



KATHOLIEKE UNIVERSITEIT
LEUVEN



 UNIVERSITY OF
CAMBRIDGE

A computationally efficient model to simulate vibrations in buildings generated by underground railways

Jonas Coene

Thesis voorgedragen tot het behalen van de graad van Master of Science in de ingenieurswetenschappen: bouwkunde, optie Civiele techniek

Promotoren:

Prof. dr. ir. Geert Degrande
Dr. ir. Hugh Hunt

Assessoren:

Dr. ir. Stijn Francois
Dr. ir. Kirsty Kuo

Academiejaar 2011 – 2012

© Copyright KU Leuven

Without written permission of the thesis supervisors and the author it is forbidden to reproduce or adapt in any form or by any means any part of this publication. Requests for obtaining the right to reproduce or utilize parts of this publication should be addressed to Faculteit Ingenieurswetenschappen, Kasteelpark Arenberg 1 bus 2200, B-3001 Heverlee, +32-16-321350.

A written permission of the thesis supervisors is also required to use the methods, products, schematics and programs described in this work for industrial or commercial use, and for submitting this publication in scientific contests.

Zonder voorafgaande schriftelijke toestemming van zowel de promotoren als de auteur is overnemen, kopiëren, gebruiken of realiseren van deze uitgave of gedeelten ervan verboden. Voor aanvragen tot of informatie i.v.m. het overnemen en/of gebruik en/of realisatie van gedeelten uit deze publicatie, wend u tot Faculteit Ingenieurswetenschappen, Kasteelpark Arenberg 1 bus 2200, B-3001 Heverlee, +32-16-321350.

Voorafgaande schriftelijke toestemming van de promotoren is eveneens vereist voor het aanwenden van de in deze masterproef beschreven (originele) methoden, producten, schakelingen en programma's voor industrieel of commercieel nut en voor de inzending van deze publicatie ter deelname aan wetenschappelijke prijzen of wedstrijden.

Preface

This master thesis is the final step in becoming a civil engineer. I have enjoyed studying in Leuven, and had the privilege to spend half a year at the University of Cambridge on a Erasmus exchange. It was an experience I will never forget.

The work presented in this master thesis was performed between September 2011 and August 2012 at the University of Cambridge and KU Leuven. An ongoing collaboration between the Dynamics and Vibration division at the University of Cambridge and the Structural Mechanics division at KU Leuven has led to an Erasmus exchange between the two universities. I am very grateful to Professor Geert Degrande and Dr Hugh Hunt for giving me this opportunity and supporting me throughout the year.

I would also like to thank Dr Kirsty Kuo. She was always available when I had a problem and was interested in all aspects of my work. I am also grateful to Dr Mohammed Hussein of the University of Nottingham. He welcomed me in Nottingham and taught me the details of the PiP model, a model that I would use throughout the year.

Finally, I would like to thank my parents and sisters. They have supported me throughout these years.

Jonas Coene

Abstract

Ground-borne vibrations are a growing concern in urban areas. These vibrations create noise and discomfort in buildings. In this dissertation a model is presented to calculate vibration levels in buildings due to an underground railway. The model is computationally efficient and makes it possible to assess design options for both underground railways and buildings.

The Pipe in Pipe (PiP) model is used as a model for the underground railway. The soil is modelled as a full space with a cylindrical cavity using the elastic continuum equations and the tunnel wall is modelled as a thin cylindrical shell. The track is modelled as a floating slab track. Despite the simplifying assumptions, the PiP model is representative for an underground railway and computationally efficient.

The building is represented as a two-dimensional portal frame. The dynamic stiffness matrix method is used in combination with periodic structure theory to model an infinite building. Novak's model is used to model the pile foundation of the building. The behaviour of the infinite model agrees with that of the finite model due to the radiation damping of the pile foundation. An infinite model is a good representation of a multistory building and needs less computing power than finite models.

The vibrations generated by the PiP model are used as an input for the building model. An uncoupled source-receiver method is used to join both models. This means that the presence of the building is assumed to have no influence on the vibrations generated by the underground railway. The building model is then integrated in the graphical user interface of the PiP model creating an efficient computer program to evaluate different design options for underground railways or buildings.

In general, a reduction of the vibration level at the location of the building can be observed. This is the result of the extra mass and damping of the building. The vibrations only propagate through the building at particular frequencies and these frequencies coincide with certain eigenmodes of the building.

In addition, the PiP model is used to analyse the influence of a composite tunnel and of a curvature in the tunnel. In both cases, the influence was limited.

Samenvatting

Trillingen die zich voortplanten door de ondergrond vormen een groeiend probleem in stedelijke gebieden. Deze trillingen zorgen voor geluidsoverlast en ongemak in gebouwen. In deze thesis wordt een model voorgesteld om het trillingsniveau te berekenen in gebouwen veroorzaakt door ondergronds treinverkeer. Het model is rekentechnisch efficiënt en maakt het mogelijk om verschillende ontwerp mogelijkheden voor metro's en gebouwen te beoordelen.

Het *PiPe in Pipe* (PiP) model wordt gebruikt om de metrotunnel te modelleren. De grond wordt gemodelleerd als een continuüm met een cilindrische holte en de tunnel zelf wordt gemodelleerd als een dunne cilindrische schaal. De spoorbaan wordt gemodelleerd als een *floating slab track* (FST). Ondanks de vereenvoudigingen geeft het PiP model een representatief beeld van trillingen veroorzaakt door metro's en is het tegelijk efficiënt.

Het gebouw wordt voorgesteld als een tweedimensionaal portiek. De dynamische stijfheid methode wordt gebruikt in combinatie met de theorie voor periodieke structuren om een oneindig gebouw te modelleren. Het Novak model wordt toegepast voor de paalfundering. Het gedrag van het oneindige model komt goed overeen met dat van het eindige model door de demping veroorzaakt door de paalfundering. Een oneindig model is een goede weergave van een gebouw met meerdere verdiepingen en vergt tegelijk minder computer kracht.

De trillingen gegenereerd door het PiP model worden gebruikt als input voor het gebouw model. Hiervoor is gebruik gemaakt van een ontkoppelde bron-ontvanger methode. Er wordt dus verondersteld dat de aanwezigheid van het gebouw geen invloed heeft op de trillingen geproduceerd door de metro. Het gebouw model is vervolgens geïntegreerd in de grafische gebruikersinterface van het PiP model. Zodoende wordt een efficiënt computerprogramma verkregen om verschillende ontwerpopties voor een metrotunnel of een gebouw te beoordelen.

Over het algemeen wordt een reductie van het trillingsniveau waargenomen op de plaats waar het gebouw zich bevindt. Dit is het gevolg van de extra massa en demping die het gebouw veroorzaakt. De trillingen planten zich enkel bij bepaalde frequenties voort doorheen het gebouw. Deze komen overeen met bepaalde eigenmodes van het gebouw.

Daarnaast werd het PiP model gebruikt om de invloed van een composiet tunnel en een kromme tunnel te analyseren. In beide gevallen was de invloed beperkt.

Contents

Preface	i
Abstract	ii
Samenvatting	iii
1 Introduction	1
1.1 Ground-borne vibration	1
1.2 Pipe in Pipe model	1
1.3 Building model	3
1.4 Outline of the dissertation	3
2 Pipe in Pipe model	5
2.1 Modelling the tunnel	5
2.2 Modelling the track	16
2.3 Conclusion	25
3 Modelling of a multistorey building	27
3.1 Dynamic stiffness method	27
3.2 Finite building model	34
3.3 Infinite building model	36
3.4 Comparison of finite and infinite building models	40
3.5 Conclusion	47
4 Coupling the PiP model to the building model	48
4.1 Method of joining subsystems	48
4.2 Joining the PiP model and the building model	50
4.3 Response of the entire building	53
4.4 Graphical user interface	53
4.5 Case study	56
4.6 Conclusion	59
5 Composite tunnel	61
5.1 Continuum equations for the composite tunnel and surrounding soil	62
5.2 Coupling the tunnel and the soil	63
5.3 Parametric study	64
5.4 Conclusion	67
6 Curved tunnel	70
6.1 Curvature in the horizontal plane	70

6.2	Curvature in the vertical plane	72
6.3	Conclusion	75
7	Conclusion	76
7.1	Conclusion	76
7.2	Recommendations for future work	77
A	Overview of the PiP model	78
B	Coefficient matrices for cylindrical shell and elastic continuum	80
B.1	Coefficients for the cylindrical shell	80
B.2	Coefficients for the elastic continuum	81
C	Displacements of the floating slab track due to unit load on the track	83
	Bibliography	85

Chapter 1

Introduction

1.1 Ground-borne vibration

Ground-borne vibrations are becoming a growing concern, especially in urban areas. As cities become more densely populated, sites with high vibration levels will now be used as building grounds and people will be living and working more closely to sources of vibration.

Ground-borne vibration can be induced by busy roadways or railways. Except for old masonry structures they don't form a danger for the structural integrity. However they cause discomfort in buildings and can damage sensitive equipment. People experience vibration transmitted into buildings as vibratory motion and re-radiated noise caused by vibrating surfaces. People are perceptible for vibrations in a frequency range of 1 Hz to 80 Hz, while the problem of re-radiated noise goes up to 250 Hz [6].

In this dissertation the vibrations in multistory buildings due to underground railways will be investigated. A model is developed to simulate the underground railway and the multistory building.

1.2 Pipe in Pipe model

Nowadays, finite element methods and boundary element methods are the most frequently used to model underground railways and buildings. These models, however, are computationally demanding. At the University of Cambridge a model is developed to simulate vibrations due to underground railways that is both accurate and computationally efficient. It is called the Pipe in Pipe (PiP) model and it provides an efficient tool to assess different options in the early design stages of an underground railway [6, 11].

The PiP model is developed by Forrest [6]. It is based on a model used to investigate the dynamic behaviour of underground pipelines. The tunnel is modelled as an infinitely long cylindrical tube surrounded by soil of infinite radial extent. The cylindrical shell theory is used to model the tunnel wall and the wave equations for

an elastic continuum are used to model the surrounding soil. Due to the cylindrical symmetry, a cylindrical coordinate system is used.

At the invert of the tunnel a track is added. To reduce vibration levels, a floating slab track (FST) can be applied in underground railways. This configuration is used in the PiP model.

The PiP model has been further extended and used in many other research studies. A brief overview is given below.

1.2.1 Evolution of PiP

The basic formulation of the model is presented by Forrest [6]. He derived the expressions for the tunnel wall and the soil and added a track at the invert of the tunnel. He also further extended the model of the FST to incorporate bending and torsion.

Talbot [21] modelled a piled foundation using Euler-Bernoulli beam theory for the pile and the boundary element method for the soil. He coupled the foundation to a multistory building via resilient bearings to investigate the vibration transmission into buildings. With this model he could also investigate the pile-soil-pile interaction. The PiP model provided a vibration source for the building model.

In his PhD thesis, Hussein [11] investigated the effect of using discontinuous slabs instead of one continuous slab and the effect of a slab with two or three lines of support or uniform support instead of one single line of support. He also incorporated asymmetric loads on the tunnel invert and investigated the influence of out of phase roughness of the two rails. A graphical user interface of the PiP model is programmed by Hussein using Matlab.

In the PiP model developed by Forrest, the soil extended infinitely in the radial direction. Rikse [19] adapted the PiP model to include bedrock, a free surface and horizontal soil layers. The bedrock was included by using the mirror image method. In collaboration with Hussein, he used the fictitious force method in combination with the ElastoDynamic Toolbox (EDT) to model the free surface and the horizontal soil layers. The EDT is developed at the Structural Mechanics division of KU Leuven [20].

Coulier [3] extended the pile model developed by Talbot. He modelled the pile using the Timoshenko beam theory instead of the Euler-Bernoulli theory. The model was used to investigate the shadow effect between multiple piles.

Beckers [1] investigated whether the simplifications made to model the track and the tunnel in the PiP model can be justified. He adapted the track model to correctly model unevenness correlations between the two rails. In the original model, the rails are modelled as one single beam and thus the unevenness on both rails is fully positively correlated. He also added a concrete layer directly fixed on the tunnel invert, modelled a double track railway tunnel and investigated the influence of a curvature on vibration levels in the soil.

Jones [12] investigated the influence of the simplifying assumptions made in the PiP model. He investigated the influence of voids at the tunnel-soil interface and the influence of assuming the soil as a homogeneous continuum. He investigated the

effect of inclined soil layers, the effect of a subsiding soil layer and the effect of soil inhomogeneity.

The most recent work is that of Kuo [13]. With the techniques used in the PiP model she made a twin tunnel model. The underground networks in cities mostly consist of two tunnels next to each other. She also modelled a piled foundation. A pile is modelled as a cylinder in an elastic continuum much like the tunnel is modelled in the PiP model. The original PiP model served as a vibration input for this model.

In Appendix A a table is given containing the different features added to the PiP over the years in chronological order.

1.3 Building model

Finite element methods are the most widely used to model buildings. Despite their accuracy, they often require very high computation times. In many multistory buildings a regular pattern of floors and columns can be recognised. Therefore a multistory building can be modelled as a portal frame. Cryer [4] modelled a multistory building with a piled foundation as a two-dimensional portal frame using the dynamic stiffness method (DSM). The building is divided in substructures, such as the columns, floors or piles, for which an analytical solution is known. These solutions are then combined to obtain the response of the entire building.

Cryer also compared the difference between finite and infinite building models. The infinite buildings are modelled using periodic structure theory. For finite building models without a piled foundation he observed standing waves in the building due to the reflection at the ends of the building. These standing waves aren't present in real buildings nor in the infinite building model. When a piled foundation is connected to the building, these standing waves are reduced because part of the vibration is radiated back into the soil. This is observed both in the finite and infinite models. Comparing the results of the models with site measurements, Cryer concludes that an infinite model is a good representation of a multistory building.

1.4 Outline of the dissertation

The purpose of this dissertation is to develop a model that simulates vibrations in buildings due to underground railways. The model has to be both accurate and computationally efficient. It should be a tool to assess different options in the early design stages of buildings and railway tunnels. Therefore the PiP model developed by Forrest is connected to a building model similar to that of Cryer. Finally the graphical user interface of the PiP model is updated to include a building.

Chapter 2 explains the basic formulation of the PiP model. First the model for the tunnel is presented. The tunnel wall is modelled with the cylindrical shell equations and the soil with the elastic continuum equations. Then the model for a FST is presented.

The building model is presented in Chapter 3. First the DSM is explained and the analytical solutions for the different substructures are given. The floors and

columns are modelled as beams using the Euler-Bernoulli beam theory. The piles are modelled using Novak's model. Next the stiffness matrices for a finite and an infinite building are calculated. For the infinite building, periodic structure theory is used. In section 3.4 the models are validated and the difference between finite and infinite models is investigated.

In Chapter 4 the PiP model and the infinite building model are connected. An uncoupled source-receiver model is used. This means that the presence of the building has no influence on vibrations generated by the underground railway. Afterwards, the building model is integrated in the GUI of the PiP model and a case study is presented.

In Chapter 5 a composite tunnel is modelled. This is done by adding an extra pipe to the PiP model. Instead of using the cylindrical shell equations for the tunnel wall, the elastic continuum equations are used to model the two parts of the composite tunnel wall and the soil.

In Chapter 6 the influence of a curvature of the tunnel on the vibration level in the soil is investigated. A purely geometrical approach is used.

Overall conclusions and recommendations for future work are presented in Chapter 7.

Chapter 2

Pipe in Pipe model

The Pipe in Pipe model (PiP model) is developed by Forrest [6] to model ground vibration from underground railways. Hussein [11] further extended this model and made a graphical user interface (GUI) using Matlab. The PiP model is both accurate and computationally efficient and therefore it is a useful tool to assess design options for underground railways. This chapter gives an extensive overview of the PiP model.

Different sections in this chapter are taken from Chapters 3 to 5 of the PhD thesis of Forrest [6]. The PiP model is not the new element in this dissertation, but a basic understanding of this model is necessary before one can continue to add different features to it. For a full description of the PiP model, the reader is referred to the PhD thesis of Forrest.

In section 2.1 a method is presented to model the tunnel wall and the surrounding soil. The tunnel is modelled as a cylindrical shell and the soil is modelled as a full space with a cylindrical cavity. This can be seen as a pipe running through another pipe. In later versions of the PiP model a free surface and other features are added.

In section 2.2 the track in the tunnel will be modelled. The configuration that is used here is a floating slab track (FST). The typical arrangement of a floating slab track is shown in Figure 2.1. Two rails are mounted via rail pads and rail fasteners onto a massive concrete slab, which in turn rests on slab bearings supported by the tunnel invert. The purpose of the rail pads, track slab and the slab bearings is to provide vibration isolation to the tunnel invert from the track.

2.1 Modelling the tunnel

In the PiP model presented by Forrest, the thin shell theory is used to model the tunnel and the elastic continuum equations are used to model the surrounding soil. Alternatively, both the tunnel and the soil can be modelled with the elastic continuum equations. This approach will be used to model a composite tunnel in Chapter 5. However, in Chapter 4 the PiP model developed by Forrest will be used to simulate vibrations from underground railways at the foundation of a building. Therefore, both methods will be presented in this chapter.

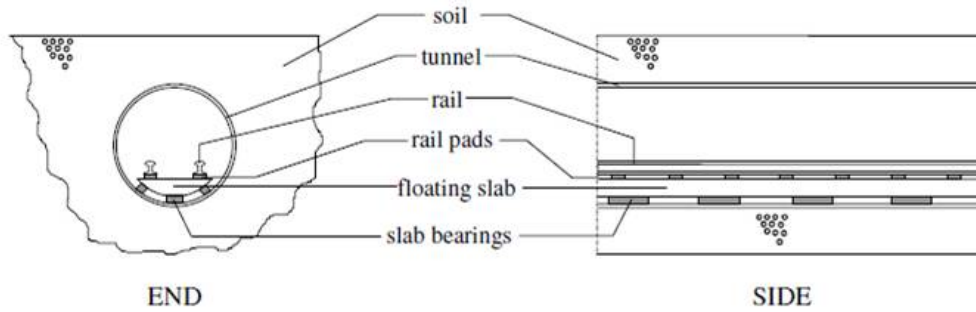


FIGURE 2.1: Underground railway layout showing the components of floating slab track [6].

2.1.1 Cylindrical Shell Equations

The main assumption of thin shell theory is that displacement and stress do not vary through the thickness of the shell. Forrest used a simplified version of the linear equations of motion for a general thin shell made of linear elastic, homogeneous, isotropic material [6]. For the three principal directions, as shown in Figure 2.2, a dynamic equilibrium equation is formulated.

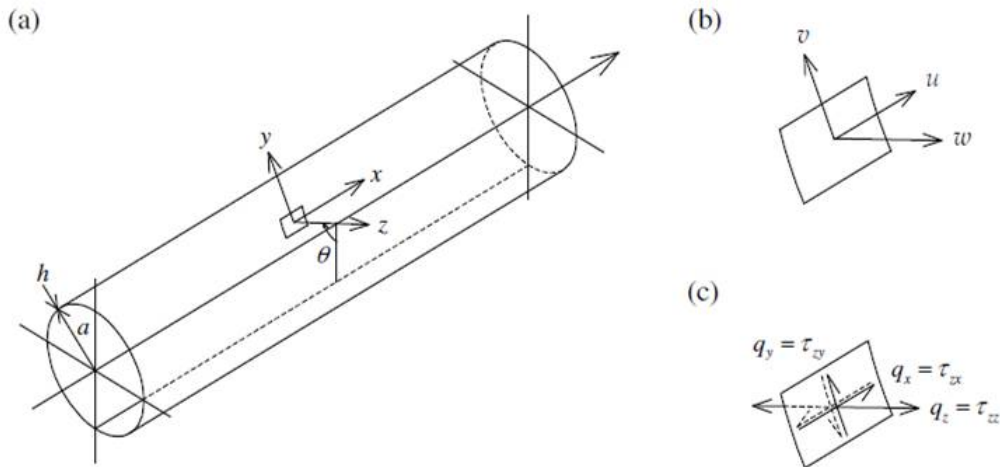


FIGURE 2.2: Coordinate system used for the thin-walled cylindrical-shell theory, showing (a) the principle directions for a typical element in the shell, (b) the corresponding displacement components and (c) the corresponding surface stress components [6].

Equilibrium in the longitudinal direction x gives [6]

$$\begin{aligned} a \frac{\partial^2 u}{\partial x^2} + \frac{(1-\nu)}{2a} \frac{\partial^2 u}{\partial \theta^2} + \frac{(1+\nu)}{2} \frac{\partial^2 v}{\partial x \partial \theta} - \nu \frac{\partial w}{\partial x} \\ + \frac{h^2}{12} \left[\frac{(1-\nu)}{2a^3} \frac{\partial^2 u}{\partial \theta^2} + \frac{\partial^3 w}{\partial x^3} - \frac{(1-\nu)}{2a^2} \frac{\partial^3 w}{\partial x \partial \theta^2} \right] \\ + a \frac{(1-\nu^2)}{Eh} q_x - \rho a \frac{(1-\nu^2)}{E} \frac{\partial^2 u}{\partial t^2} = 0 \end{aligned} \quad (2.1)$$

equilibrium in the tangential direction y gives [6]

$$\begin{aligned} \frac{(1-\nu)}{2} \frac{\partial^2 u}{\partial x \partial \theta} + a \frac{(1-\nu)}{2} \frac{\partial^2 v}{\partial x^2} + \frac{1}{a} \frac{\partial^2 v}{\partial \theta^2} - \frac{1}{a} \frac{\partial w}{\partial \theta} \\ + \frac{h^2}{12} \left[\frac{3(1-\nu)}{2a} \frac{\partial^2 v}{\partial x^2} + \frac{(3-\nu)}{2a} \frac{\partial^3 w}{\partial x^2 \partial \theta} \right] \\ + a \frac{(1-\nu^2)}{Eh} q_y - \rho a \frac{(1-\nu^2)}{E} \frac{\partial^2 v}{\partial t^2} = 0 \end{aligned} \quad (2.2)$$

and equilibrium in the radial direction z gives [6]

$$\begin{aligned} \nu \frac{\partial u}{\partial x} + \frac{1}{a} \frac{\partial v}{\partial \theta} - \frac{1}{a} w - \frac{h^2}{12} \left[a \frac{\partial^4 w}{\partial x^4} + \frac{2}{a} \frac{\partial^4 w}{\partial x^2 \partial \theta^2} + \frac{1}{a^3} \frac{\partial^4 w}{\partial \theta^4} \right] \\ - \frac{h^2}{12} \left[\frac{\partial^3 u}{\partial x^3} - \frac{(1-\nu)}{2a^2} \frac{\partial^3 u}{\partial x \partial \theta^2} + \frac{(3-\nu)}{2a} \frac{\partial^3 v}{\partial x^2 \partial \theta} + \frac{1}{a^3} w + \frac{2}{a^3} \frac{\partial^2 w}{\partial \theta^2} \right] \\ + a \frac{(1-\nu^2)}{Eh} q_z - \rho a \frac{(1-\nu^2)}{E} \frac{\partial^2 w}{\partial t^2} = 0 \end{aligned} \quad (2.3)$$

where u , v and w are the time dependent displacement components in directions x , y and z , respectively, a is the mean radius of the shell and h is its thickness. The shell material has Young's modulus E , Poisson's ratio ν and density ρ . The effects of material damping are accounted for by using complex material parameters in the frequency domain. The following stress components on the inside surface of the shell represent the applied loading: two shear tractions q_x and q_y , and one normal stress q_z . These are actually the net stresses: they are the differences between the inside and outside values of the surface stresses τ_{zx} , τ_{zy} and τ_{zz} respectively. The displacement and stress components are also shown in Figure 2.2.

It is assumed that the applied loading is harmonic in both space and time. The stress components have the form

$$\begin{aligned} q_x(x, t) &= \tilde{Q}_{xn} \cos(n\theta) e^{i(\omega t + \xi x)} \\ q_y(x, t) &= \tilde{Q}_{yn} \sin(n\theta) e^{i(\omega t + \xi x)} \\ q_z(x, t) &= \tilde{Q}_{zn} \cos(n\theta) e^{i(\omega t + \xi x)} \end{aligned} \quad (2.4)$$

and are separable in time t , space x and angular position θ . ω is the angular frequency, ξ is the angular wavenumber and n is a positive integer. The displacement

components resulting from these stress components and satisfying the equilibrium equations (2.1) to (2.3) have the form

$$\begin{aligned} u(x,t) &= \tilde{U}_n \cos(n\theta) e^{i(\omega t + \xi x)} \\ v(x,t) &= \tilde{V}_n \sin(n\theta) e^{i(\omega t + \xi x)} \\ w(x,t) &= \tilde{W}_n \cos(n\theta) e^{i(\omega t + \xi x)} \end{aligned} \quad (2.5)$$

The tilde on the coefficients \tilde{Q}_{xn} , \tilde{Q}_{yn} , \tilde{Q}_{zn} , \tilde{U}_n , \tilde{V}_n and \tilde{W}_n indicates that they are formulated in the wavenumber-frequency domain. The exponential term $e^{i\xi x}$ accounts for the infinite longitudinal extent of the cylindrical shell. The trigonometric terms represent ring modes of the cylindrical cross section and are chosen so that the displacements are symmetric about $\theta = 0$, the downward vertical. Figure 2.3 shows these ring modes and their relation to the three displacement components u , v and w .

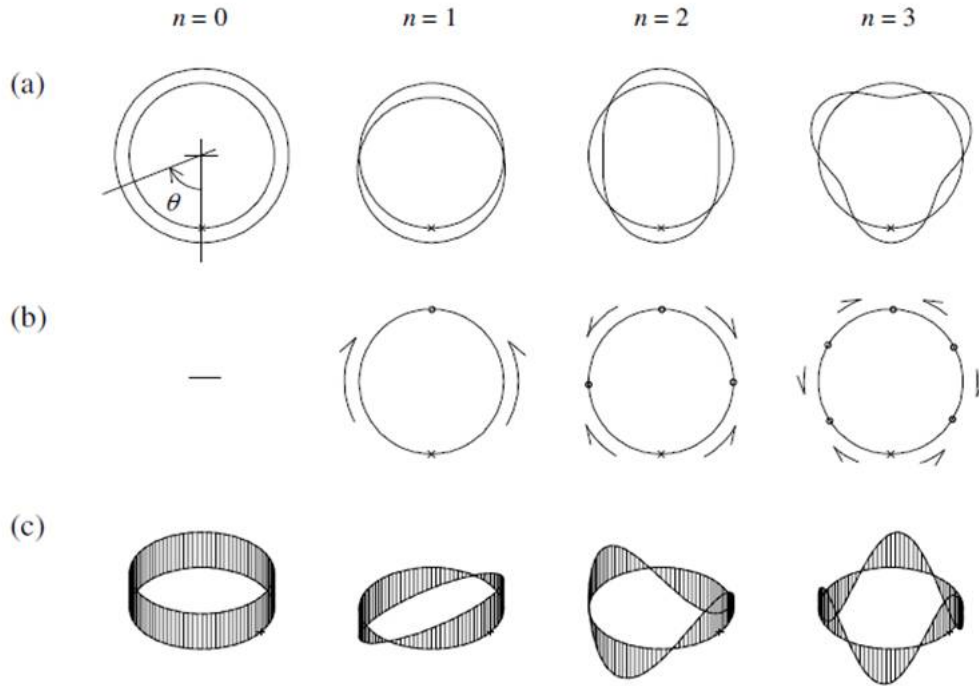


FIGURE 2.3: (a) In-plane flexural ring modes, varying as $\cos n\theta$ and corresponding to the radial displacement w ; (b) in-plane extensional ring modes, varying as $\sin n\theta$ and corresponding to the tangential displacement v ; and (c) out-of-plane flexural ring modes, varying as $\cos n\theta$ and corresponding to the displacement u , for different values of the circumferential mode number n . The $\theta = 0$ points are marked with small crosses on the undeformed ring shapes, while the small circles in (b) mark the additional nodal points on the ring's circumference [6].

A relationship between the coefficients \tilde{Q}_{xn} , \tilde{Q}_{yn} , \tilde{Q}_{zn} and \tilde{U}_n , \tilde{V}_n , \tilde{W}_n can be found by substituting the stresses (2.4) and displacements (2.5) into equations (2.1)

to (2.3). The trigonometric and exponential terms are cancelled out and this can be written in matrix form as

$$\mathbf{A} \begin{Bmatrix} \tilde{U}_n \\ \tilde{V}_n \\ \tilde{W}_n \end{Bmatrix} = \frac{-a(1-\nu^2)}{Eh} \begin{Bmatrix} \tilde{Q}_{xn} \\ \tilde{Q}_{yn} \\ \tilde{Q}_{zn} \end{Bmatrix} \quad (2.6)$$

The coefficients of the matrix \mathbf{A} are given in Appendix B. If the stress components (2.4) are known, the displacements can be found from the stresses in the wavenumber frequency domain, by substituting $\tilde{\mathbf{Q}} = \{\tilde{Q}_{xn} \quad \tilde{Q}_{yn} \quad \tilde{Q}_{zn}\}^T$ into equation (2.6) and solving for $\tilde{\mathbf{U}} = \{\tilde{U}_n \quad \tilde{V}_n \quad \tilde{W}_n\}^T$. These can then be transformed into the space time domain using equation (2.5). If the stresses $\tilde{\mathbf{Q}}$ represent a unit loading, then the displacements $\tilde{\mathbf{U}}$ represent the displacement frequency response functions (FRFs) in the wavenumber domain for a particular circumferential mode n . The actual stresses and displacements will in general be linear combinations of the modal quantities [6].

2.1.2 Elastic continuum equations

The elastic continuum equations can be used to model both the tunnel wall and the soil surrounding the tunnel. They are modelled as a three-dimensional, homogeneous, isotropic elastic solid in the form of a thick walled cylinder. For the soil, the inner diameter of the cylinder is equal to the outer diameter of the tunnel and the outer diameter is of infinite extent.

The wave equation describing motion within a three-dimensional, homogeneous, isotropic, elastic, solid medium is derived by Graff [7] and is

$$(\lambda + \mu)\nabla\nabla \cdot \mathbf{u} + \mu\nabla^2\mathbf{u} + \rho\mathbf{f} = \rho\frac{\partial^2\mathbf{u}}{\partial t^2} \quad (2.7)$$

where \mathbf{u} is the displacement vector, \mathbf{f} the vector of body forces, $\lambda = \frac{2\nu G}{(1-2\nu)}$ and $\mu = G = \frac{E}{2(1+\nu)}$ are Lamé's elastic constants for the medium where G is the shear modulus, E is Young's modulus and ν is Poisson's ratio, and ρ is the medium's density. \mathbf{f} is set to zero because the desired solution is for vibration about an equilibrium position [6]. The problem has cylindrical geometry, so the cylindrical coordinate system will be used. Figure 2.4 gives the coordinate, displacement and stress directions.

The wave equation (2.7) can be solved using the scalar and vector potentials, or Lamé's potentials, which describe the field transformation [6]

$$\mathbf{u} = \nabla\phi + \nabla \times \mathbf{H} \quad \text{with} \quad \nabla \cdot \mathbf{H} = F(\mathbf{r}, t) \quad (2.8)$$

where \mathbf{r} is the position vector $\{r \quad \theta \quad z\}^T$. The displacement equations (2.7) are satisfied if the potentials satisfy [6]

$$\begin{aligned} \nabla^2\phi &= \frac{1}{c_1^2} \frac{\partial^2\phi}{\partial t^2} \\ \nabla^2\mathbf{H} &= \frac{1}{c_2^2} \frac{\partial^2\mathbf{H}}{\partial t^2} \end{aligned} \quad (2.9)$$

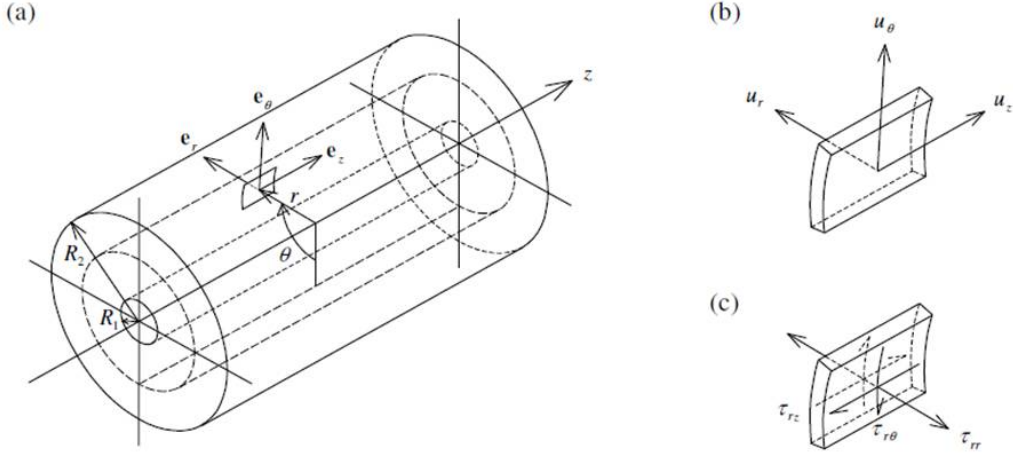


FIGURE 2.4: Coordinate system used for the theory of an elastic continuum with cylindrical geometry, showing (a) the principle directions with their unit vectors for a typical element on a cylindrical surface of radius r within the bulk medium, (b) the corresponding displacement components and (c) the corresponding cylindrical-surface stress components (stresses acting on the edges of the element are not shown) [6].

where $c_1 = \sqrt{(\lambda + 2\mu)/\rho}$ is the speed of pressure waves in the medium and $c_2 = \sqrt{\mu/\rho}$ the speed of shear waves. Since there are no surfaces or interfaces in the medium, only these two types of waves exist. The Laplacians in (2.9) for cylindrical coordinates are given by [6]

$$\begin{aligned}\nabla^2\phi &= \frac{1}{r}\frac{\partial\phi}{\partial r} + \frac{\partial^2\phi}{\partial r^2} + \frac{1}{r^2}\frac{\partial^2\phi}{\partial\theta^2} + \frac{\partial^2\phi}{\partial z^2} \\ \nabla^2\mathbf{H} &= \left(\nabla^2 H_r - \frac{H_r}{r^2} - \frac{2}{r^2}\frac{\partial H_\theta}{\partial\theta}\right)\mathbf{e}_r + \left(\nabla^2 H_\theta - \frac{H_\theta}{r^2} + \frac{2}{r^2}\frac{\partial H_r}{\partial\theta}\right)\mathbf{e}_\theta + \nabla^2 H_z\mathbf{e}_z\end{aligned}\quad (2.10)$$

where \mathbf{e}_r , \mathbf{e}_θ and \mathbf{e}_z are unit vectors in the principal directions of the cylindrical coordinate system and H_r , H_θ and H_z are the components of \mathbf{H} .

The displacement components in equation (2.8) can be written as [6]

$$\begin{aligned}u_r &= \frac{\partial\phi}{\partial r} + \frac{1}{r}\frac{\partial H_z}{\partial\theta} - \frac{\partial H_\theta}{\partial z} \\ u_\theta &= \frac{1}{r}\frac{\partial\phi}{\partial\theta} + \frac{\partial H_r}{\partial z} - \frac{\partial H_z}{\partial r} \\ u_z &= \frac{\partial\phi}{\partial z} + \frac{1}{r}\frac{\partial(rH_\theta)}{\partial r} - \frac{1}{r}\frac{\partial H_r}{\partial\theta}\end{aligned}\quad (2.11)$$

The stress components are given by the general stress-strain relation of Hooke's law:

$$\begin{aligned}\tau_{rr} &= (\lambda + 2\mu)\epsilon_{rr} + \lambda\epsilon_{\theta\theta} + \lambda\epsilon_{zz} \\ \tau_{\theta\theta} &= \lambda\epsilon_{rr} + (\lambda + 2\mu)\epsilon_{\theta\theta} + \lambda\epsilon_{zz} \\ \tau_{zz} &= \lambda\epsilon_{rr} + \lambda\epsilon_{\theta\theta} + (\lambda + 2\mu)\epsilon_{zz} \\ \tau_{r\theta} &= 2\mu\epsilon_{r\theta} = \tau_{\theta r} \\ \tau_{rz} &= 2\mu\epsilon_{rz} = \tau_{zr} \\ \tau_{\theta z} &= 2\mu\epsilon_{\theta z} = \tau_{z\theta}\end{aligned}\quad (2.12)$$

where the standard convention for designating stress direction is used. Hooke's law is valid for linear elastic materials. When damping is accounted for, the material becomes viscoelastic. However for low damping and the small magnitudes of vibration considered here, the stress-strain relations (2.12) are still valid [6]. The effects of material damping can be included by using complex material parameters in the frequency domain.

The strain components are defined in cylindrical coordinates by [7]

$$\begin{aligned}
 \epsilon_{rr} &= \frac{\partial u_r}{\partial r} \\
 \epsilon_{\theta\theta} &= \frac{1}{r} \frac{\partial u_\theta}{\partial \theta} + \frac{u_r}{r} \\
 \epsilon_{zz} &= \frac{\partial u_z}{\partial z} \\
 \epsilon_{r\theta} &= \frac{1}{2} \left(\frac{1}{r} \frac{\partial u_r}{\partial \theta} + \frac{\partial u_\theta}{\partial r} - \frac{u_\theta}{r} \right) \\
 \epsilon_{rz} &= \frac{1}{2} \left(\frac{\partial u_r}{\partial z} + \frac{\partial u_z}{\partial r} \right) \\
 \epsilon_{\theta z} &= \frac{1}{2} \left(\frac{\partial u_\theta}{\partial z} + \frac{1}{r} \frac{\partial u_z}{\partial \theta} \right)
 \end{aligned} \tag{2.13}$$

With the information from equations (2.7) to (2.13) the displacement and stress components can be calculated. If the loading applied to an infinitely long tunnel comprises stress components which are harmonic in both space and time, the following solutions for the potentials in the wave equations (2.9) can be assumed to solve the problem [6]:

$$\begin{aligned}
 \phi &= f(r) \cos(n\theta) e^{i(\omega t + \xi z)} \\
 H_r &= g_r(r) \sin(n\theta) e^{i(\omega t + \xi z)} \\
 H_\theta &= g_\theta(r) \cos(n\theta) e^{i(\omega t + \xi z)} \\
 H_z &= g_z(r) \sin(n\theta) e^{i(\omega t + \xi z)}
 \end{aligned} \tag{2.14}$$

The trigonometric terms represent ring modes of the cylindrical cross section as discussed in section 2.1.1.

Substituting of solutions (2.14) into equations (2.9), making use of the definitions (2.10) for the Laplacians and considering each component of the equation in \mathbf{H} in turn, results in four differential equations [6]:

$$\begin{aligned}
 r^2 f'' + r f' - \left[\left(\xi^2 - \frac{\omega^2}{c_1^2} \right) r^2 + n^2 \right] f &= 0 \\
 r^2 g_r'' + r g_r' - \left[\left(\xi^2 - \frac{\omega^2}{c_2^2} \right) r^2 + n^2 + 1 \right] g_r + 2n g_\theta &= 0 \\
 r^2 g_\theta'' + r g_\theta' - \left[\left(\xi^2 - \frac{\omega^2}{c_2^2} \right) r^2 + n^2 + 1 \right] g_\theta + 2n g_r &= 0 \\
 r^2 g_z'' + r g_z' - \left[\left(\xi^2 - \frac{\omega^2}{c_2^2} \right) r^2 + n^2 \right] g_z &= 0
 \end{aligned} \tag{2.15}$$

where a prime denotes differentiation with respect to r . The solutions of the differential equations in (2.15) for the functions f , g_r , g_θ and g_z are linear combinations of modified Bessel functions [6]:

$$\begin{aligned}
 f &= A I_n(\alpha r) + B K_n(\alpha r) \\
 g_r &= -g_\theta = A_r I_{n+1}(\beta r) + B_r K_{n+1}(\beta r) \\
 g_z &= A_z I_n(\beta r) + B_z K_n(\beta r)
 \end{aligned} \tag{2.16}$$

where $\alpha^2 = \xi^2 - \omega^2/c_1^2$ and $\beta^2 = \xi^2 - \omega^2/c_2^2$, $I_n(\alpha r)$, $I_n(\beta r)$, $K_n(\alpha r)$ and $K_n(\beta r)$ are modified Bessel functions of respectively the first and second kind of order n . The

coefficients A, B, A_r, B_r, A_z and B_z are to be determined from boundary conditions. These differ for the tunnel and the soil.

The displacements and stresses can be written in terms of the functions given by (2.16). This is done by substituting the expressions for the potentials (2.14) into equations (2.11) for the displacement components:

$$\begin{aligned} u_r &= \left[f' + \frac{n}{r} g_z + i\xi g_r \right] \cos(n\theta) e^{i(\omega t + \xi z)} \\ u_\theta &= \left[-\frac{n}{r} f + i\xi g_r - g_z' \right] \sin(n\theta) e^{i(\omega t + \xi z)} \\ u_z &= \left[i\xi f - \frac{(n+1)}{r} g_r + g_r' \right] \cos(n\theta) e^{i(\omega t + \xi z)} \end{aligned} \quad (2.17)$$

Using the above results for the displacements and the strain definitions (2.13), the stresses can be determined from (2.12). The surface stresses are given by

$$\begin{aligned} \tau_{rr} &= \left[(\lambda + 2\mu) f'' + \frac{\lambda}{r} f' - \lambda \left(\frac{n^2}{r^2} + \xi^2 \right) f + 2\mu i \xi g_r' + 2\mu \frac{n}{r} g_z' - 2\mu \frac{n}{r^2} g_z \right] \\ &\quad \cos(n\theta) e^{i(\omega t + \xi z)} \\ \tau_{r\theta} &= \left[-2\mu \frac{n}{r} f' + 2\mu \frac{n}{r^2} f + \mu i \xi g_r' - \mu i \xi \frac{(n+1)}{r} g_r - \mu g_z'' + \frac{\mu}{r} g_z' - \mu \frac{n^2}{r^2} g_z \right] \\ &\quad \sin(n\theta) e^{i(\omega t + \xi z)} \\ \tau_{rz} &= \left[2\mu i \xi f' - \mu g_r'' - \mu \frac{(n+1)}{r} g_r' - \mu \left(\frac{n+1}{r^2} - \xi^2 \right) g_r + \mu i \xi \frac{n}{r} g_z \right] \\ &\quad \cos(n\theta) e^{i(\omega t + \xi z)} \end{aligned} \quad (2.18)$$

These stresses are involved with the boundary conditions. Similar expressions can be found for the internal stresses $\tau_{\theta\theta}$, $\tau_{\theta z}$ and τ_{zz} .

By substituting the expressions (2.16) in equations (2.17) and (2.18), the displacements and stresses can be written in terms of modified Bessel functions of order n and $(n+1)$. The harmonic solutions can then be written in matrix form as [6]

$$\begin{aligned} \mathbf{u} &= \begin{Bmatrix} u_r \\ u_\theta \\ u_z \end{Bmatrix} = \mathbf{SUC} e^{i(\omega t + \xi z)} \\ \boldsymbol{\tau} &= \begin{Bmatrix} \tau_{rr} \\ \tau_{r\theta} \\ \tau_{rz} \\ \tau_{\theta\theta} \\ \tau_{\theta z} \\ \tau_{zz} \end{Bmatrix} = \begin{bmatrix} \mathbf{S} & \mathbf{0} \\ \mathbf{0} & \mathbf{S} \end{bmatrix} \mathbf{TC} e^{i(\omega t + \xi z)} \\ \text{with } \mathbf{S} &= \begin{bmatrix} \cos n\theta & 0 & 0 \\ 0 & \sin n\theta & 0 \\ 0 & 0 & \cos n\theta \end{bmatrix} \end{aligned} \quad (2.19)$$

$\mathbf{C} = \{A \ B \ A_r \ B_r \ A_z \ B_z\}^T$ is a vector of coefficients. These coefficients are determined from the boundary conditions. In Appendix B the 3×6 matrix \mathbf{U} defining displacements and the 6×6 matrix \mathbf{T} defining stresses are given in full. The elements of both matrices are in terms of modified Bessel functions with arguments αr and βr , and thus are functions of wavenumber ξ , frequency ω and circumferential mode number n as well as radius r and the material properties.

As for the solution of the cylindrical shell, the elastic continuum's displacements and stresses can be written in the wavenumber-frequency domain. The displacement and surface stress components are [6]

$$\begin{Bmatrix} \tilde{U}_{rn} \\ \tilde{U}_{\theta n} \\ \tilde{U}_{zn} \end{Bmatrix} = \mathbf{UC} \quad \text{and} \quad \begin{Bmatrix} \tilde{T}_{rrn} \\ \tilde{T}_{r\theta n} \\ \tilde{T}_{rzn} \end{Bmatrix} = \mathbf{T}_r \mathbf{C} \quad (2.20)$$

where the 3×6 matrix \mathbf{T}_r is the top half of the 6×6 matrix \mathbf{T} in (2.19).

2.1.3 Coupling the tunnel and soil

Before the vibrations in the tunnel or the soil can be calculated, the boundary conditions must be specified. The boundary conditions include applied loads, compatibility of displacements and equilibrium of forces at the tunnel-soil interface and a radiation condition for the infinite soil. In general the external loading applied to the tunnel will not be harmonic in space, but a linear combination of the spatially harmonic components given in (2.4) for the shell or in (2.19) for the continuum. The total displacement response can be obtained by adding the individual harmonic displacement components which result from each of the harmonic load terms which make up the total load.

Case 1: tunnel wall modelled as a thin shell

Force equilibrium for the shell when a load is applied at the invert of the shell results in:

$$A_E \tilde{\mathbf{U}}_n = \frac{-Eh}{a(1-\nu^2)} \mathbf{A} \begin{Bmatrix} \tilde{U}_n \\ \tilde{V}_n \\ \tilde{W}_n \end{Bmatrix} = \begin{Bmatrix} \tilde{Q}_{xn} \\ \tilde{Q}_{yn} \\ \tilde{Q}_{zn} \end{Bmatrix} = \begin{Bmatrix} \tilde{P}_{xn} \\ \tilde{P}_{yn} \\ \tilde{P}_{zn} \end{Bmatrix} - \begin{Bmatrix} \tilde{T}_{zxn} \\ \tilde{T}_{zy n} \\ \tilde{T}_{zzn} \end{Bmatrix}_{\text{outside}} \quad (2.21)$$

where $\tilde{\mathbf{P}}_n = \{\tilde{P}_{xn} \ \tilde{P}_{yn} \ \tilde{P}_{zn}\}^T$ are the stress components at the inside of the shell induced by the applied load and $\tilde{\mathbf{T}}_n = \{\tilde{T}_{zxn} \ \tilde{T}_{zy n} \ \tilde{T}_{zzn}\}^T$ are the stresses at the tunnel soil interface.

Due to the infinite extent of the soil, the equations (2.20) describing the continuum can be reduced. The displacements \mathbf{u} and stresses $\boldsymbol{\tau}$ for the continuum are expressed as linear combinations of modified Bessel functions. Only the Bessel functions of the second kind $K_n(\alpha r)$ and $K_n(\beta r)$ decay for all arguments as r increases. Thus the

coefficients of the modified Bessel function of the first kind $I_n(\alpha r)$ and $I_n(\beta r)$ must be set to zero for the radiation condition to be satisfied [6]. This means that

$$\begin{aligned} A = A_r = A_z &= 0 \\ \Rightarrow \mathbf{C}_{\text{red}} &= \left\{ 0 \ B \ 0 \ B_r \ 0 \ B_z \right\}^T \end{aligned} \quad (2.22)$$

In turn, the first, third and fifth elements of each row in the matrices \mathbf{U} and \mathbf{T} drop out of the equation. These are the terms containing Bessel functions $I_n(\alpha r)$ and $I_n(\beta r)$.

The coordinate system for the shell differs from that for the continuum. The relationships between the displacements and stresses in the two different coordinate systems can be found by comparing Figure 2.2 and Figure 2.4. They are

$$\begin{aligned} u &\equiv u_z & \tau_{zx} &\equiv -\tau_{rz} \\ v &\equiv u_\theta & \tau_{zy} &\equiv -\tau_{r\theta} \\ w &\equiv -u_r & \tau_{zz} &\equiv \tau_{rr} \end{aligned} \quad (2.23)$$

The coordinate system of the shell will be used here. The displacements at the tunnel-soil interface can be written as

$$\begin{Bmatrix} \tilde{U}_n \\ \tilde{V}_n \\ \tilde{W}_n \end{Bmatrix} = \begin{Bmatrix} \tilde{U}_{zn} \\ \tilde{U}_{\theta n} \\ -\tilde{U}_{rn} \end{Bmatrix}_{r=a} = \begin{bmatrix} u_{32} & u_{34} & u_{36} \\ u_{22} & u_{24} & u_{26} \\ -u_{12} & -u_{14} & -u_{16} \end{bmatrix}_{r=a} \begin{Bmatrix} B \\ B_r \\ B_z \end{Bmatrix} = [\mathbf{U}_\infty]_{r=a} \mathbf{B} \quad (2.24)$$

Equilibrium of forces at the interface results in

$$\begin{Bmatrix} \tilde{T}_{zxn} \\ \tilde{T}_{zyn} \\ \tilde{T}_{zzn} \end{Bmatrix}_{\text{outside}} = \begin{Bmatrix} -\tilde{T}_{rzn} \\ -\tilde{T}_{r\theta n} \\ \tilde{T}_{rrn} \end{Bmatrix}_{r=a} = \begin{bmatrix} -t_{32} & -t_{34} & -t_{36} \\ -t_{22} & -t_{24} & -t_{26} \\ t_{12} & t_{14} & t_{16} \end{bmatrix}_{r=a} \begin{Bmatrix} B \\ B_r \\ B_z \end{Bmatrix} = [\mathbf{T}_\infty]_{r=a} \mathbf{B} \quad (2.25)$$

where the u_{jk} and t_{jk} are the remaining elements of \mathbf{U} and \mathbf{T}_r

Substituting the displacements (2.24) and stresses (2.25) into equation (2.21) results in

$$\mathbf{A}_E [\mathbf{U}_\infty]_{r=a} \mathbf{B} = \tilde{\mathbf{P}} - [\mathbf{T}_\infty]_{r=a} \mathbf{B} \quad (2.26)$$

Solving for \mathbf{B} gives

$$\mathbf{B} = [[\mathbf{T}_\infty]_{r=a} + \mathbf{A}_E [\mathbf{U}_\infty]_{r=a}]^{-1} \tilde{\mathbf{P}} \quad (2.27)$$

Once the coefficients \mathbf{B} are known, the displacements and stresses in the tunnel wall ($r = a$) or at some radius R elsewhere in the soil can be calculated with

$$\tilde{\mathbf{U}}_n = [\mathbf{U}_\infty]_{r=R} \mathbf{B} \quad \text{and} \quad \tilde{\mathbf{T}}_n = [\mathbf{T}_\infty]_{r=R} \mathbf{B} \quad (2.28)$$

Case 2: tunnel wall modelled as a thick shell

The continuum equations are used to model both the tunnel wall and the soil. The tunnel has an inner radius r_i and outer radius r_o . The displacement and stress components in (2.20) for the tunnel wall can be written as

$$\tilde{\mathbf{U}}_t = \mathbf{U}_t \mathbf{C} \quad \text{and} \quad \tilde{\mathbf{T}}_t = \mathbf{T}_{rt} \mathbf{C} \quad (2.29)$$

As in the previous section, the continuum equations for the soil can be simplified due to the infinite extent of the soil. This results in the following displacement components

$$\tilde{\mathbf{U}}_s = \begin{bmatrix} u_{12} & u_{14} & u_{16} \\ u_{22} & u_{24} & u_{26} \\ u_{32} & u_{34} & u_{36} \end{bmatrix} \begin{Bmatrix} B \\ B_r \\ B_z \end{Bmatrix} = \mathbf{U}_s \mathbf{B} \quad (2.30)$$

and stress components

$$\tilde{\mathbf{T}}_s = \begin{bmatrix} t_{12} & t_{14} & t_{16} \\ t_{22} & t_{24} & t_{26} \\ t_{32} & t_{34} & t_{36} \end{bmatrix} \begin{Bmatrix} B \\ B_r \\ B_z \end{Bmatrix} = \mathbf{T}_{rs} \mathbf{B} \quad (2.31)$$

Now the boundary conditions can be included. Force equilibrium at the invert of the tunnel results in:

$$\tilde{\mathbf{T}}_{ti} = [\mathbf{T}_{rt}]_{r=r_i} \mathbf{C} = \tilde{\mathbf{P}} \quad (2.32)$$

Compatibility at the tunnel-soil interface results in

$$\tilde{\mathbf{U}}_{to} = [\mathbf{U}_t]_{r=r_o} \mathbf{C} = [\mathbf{U}_s]_{r=r_o} \mathbf{B} = \tilde{\mathbf{U}}_{so} \quad (2.33)$$

and

$$\tilde{\mathbf{T}}_{to} = [\mathbf{T}_{rt}]_{r=r_o} \mathbf{C} = [\mathbf{T}_{rs}]_{r=r_o} \mathbf{B} = \tilde{\mathbf{T}}_{so} \quad (2.34)$$

The coefficients \mathbf{B} can be written in function of the coefficients \mathbf{C}

$$\mathbf{B} = [\mathbf{U}_s]_{r=r_o}^{-1} [\mathbf{U}_t]_{r=r_o} \mathbf{C} \quad (2.35)$$

Substituting into equation (2.34) gives

$$\left([\mathbf{T}_{rt}]_{r=r_o} - [\mathbf{T}_{rs}]_{r=r_o} [\mathbf{U}_s]_{r=r_o}^{-1} [\mathbf{U}_t]_{r=r_o} \right) \mathbf{C} = \mathbf{O} \quad (2.36)$$

where \mathbf{O} is a 3×1 zero matrix. Combining expressions (2.32) and (2.36), gives a solution for \mathbf{C}

$$\mathbf{C} = \left[\begin{array}{c} [\mathbf{T}_{rt}]_{r=r_i} \\ [\mathbf{T}_{rt}]_{r=r_o} - [\mathbf{T}_{rs}]_{r=r_o} [\mathbf{U}_s]_{r=r_o}^{-1} [\mathbf{U}_t]_{r=r_o} \end{array} \right]^{-1} \begin{Bmatrix} \tilde{\mathbf{P}} \\ \mathbf{O} \end{Bmatrix} \quad (2.37)$$

Once the coefficients \mathbf{C} are determined, the coefficients \mathbf{B} can be calculated with (2.35). The displacements and stresses at some radius R in the tunnel or soil can be calculated with

$$\tilde{\mathbf{U}}_n = [\mathbf{U}_t]_{r=R} \mathbf{C} \quad \text{and} \quad \tilde{\mathbf{T}}_n = [\mathbf{T}_{rt}]_{r=R} \mathbf{C} \quad (2.38)$$

if $r_i \leq R < r_o$ or with

$$\tilde{\mathbf{U}}_n = [\mathbf{U}_s]_{r=R} \mathbf{B} \quad \text{and} \quad \tilde{\mathbf{T}}_n = [\mathbf{T}_{rs}]_{r=R} \mathbf{B} \quad (2.39)$$

if $R > r_o$.

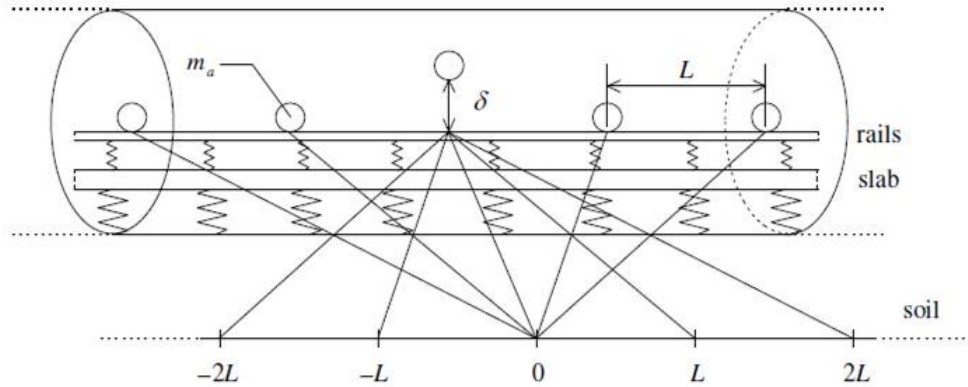


FIGURE 2.5: Full track model supported on the tunnel invert, with masses added to represent axles of a train. The centre mass is excited by a roughness displacement input δ . The tunnel's infinite length means the responses at one point in the soil to each axle input (paths with dashed lines) are equivalent to the line of separate responses to the single input shown (paths with solid lines) for an infinite number of masses at regular spacing [6].

2.2 Modelling the track

The track model used in the PiP model is shown in Figure 2.5. It consists of a simple slab beam supporting a rail beam that represents the two rails together. The axle-wheel assemblies of the train are included by adding masses placed at regular intervals. The slab and rail beams are infinitely long. The output of the PiP model is the displacement response at a certain point in the soil when there are a series of input loads along the rails due to a train running on the track. For just one input load, the load and the observation point can be shifted longitudinally while maintaining their separation with no difference in response due to the infinite length of the tunnel. In other words, the response in the soil at $x = 0$ to a load on the rail at $x = L$ is identical to the response at $x = -L$ to the same load at $x = 0$. For tangential and radial soil response components, which are even functions of x , it is also identical to the response at $x = L$ to the load at $x = 0$. In this case, only the magnitude of the separation matters. Instead of finding the set of FRFs for the soil response at $x = 0$ to a set of loads at various positions on the rail, the problem can be solved by finding the FRFs for the soil at those various longitudinal positions to a single load at $x = 0$. The shifting principle for a tunnel and track model with axle masses is shown in Figure 2.5. It has to be noted that this is only true for an infinite number of axle masses at regular spacing. The overall model remains infinite and the longitudinal symmetry is maintained with any amount of shifting. Nevertheless, a finite number of axles is sufficient if only an input at the middle axle ($x = 0$) is used and the responses of the model do not change with more axles added at the ends [6].

The total soil response due to all the axle loads acting simultaneously can be

calculated by adding up all the FRFs for an input at $x = 0$, after scaling and phasing each one appropriately. If the train is infinitely long and the inputs random, the sum represents the response anywhere along the soil line and thus condenses the three-dimensional problem represented by the individual FRFs to a two-dimensional problem of the vibration level at a particular point in the cross section of the tunnel and soil [6].

2.2.1 Coupling the floating slab track and tunnel

The connection between the floating slab track and the tunnel invert will be done in the frequency-wavenumber domain. First consider a general continuous distribution of a time harmonic force per unit length $Q(x)$ acting along a line such as the joining line on the tunnel invert as shown in Figure 2.6. The distributed force can be seen as a series of point loads represented by pulses of infinitesimal width $d\chi$ and magnitude $Q(\chi)$. The increment of the time-harmonic displacement response $Y(x)$ to one of these point loads is $dY(x) = H(x - \chi)Q(\chi)d\chi$, where $H(x)$ is the frequency response function for $Y(x)$ to a point load acting at $x = 0$. The total displacement response is the sum of these increments over the whole length of the infinite joining line, giving the integral

$$Y(x) = \int_{-\infty}^{\infty} H(x - \chi)Q(\chi)d\chi \quad (2.40)$$

which is a convolution integral in space [6]. If the Fourier transform of both sides of this equation is taken using the first integral of the transform pair

$$\begin{aligned} \tilde{Y}(\xi) &= \int_{-\infty}^{\infty} Y(x)e^{-i\xi x} dx \\ Y(x) &= \frac{1}{2\pi} \int_{-\infty}^{\infty} \tilde{Y}(\xi)e^{i\xi x} d\xi \end{aligned} \quad (2.41)$$

then (2.40) becomes

$$\tilde{Y}(\xi) = \tilde{H}(\xi)\tilde{Q}(\xi) \quad (2.42)$$

The convolution in space has been reduced to a simple multiplication in the wavenumber domain.

In Figure 2.7 a schematic overview is given of the floating slab track in the tunnel. Expression (2.42) can be applied to this problem. When a unit point load acts on the slab at $x = 0$ this yields

$$\begin{aligned} \tilde{Y}_1 &= \tilde{H}_{11}(-\tilde{G}_a + 1) \\ \tilde{Y}_2 &= \tilde{H}_{22}(\tilde{G}_a - \tilde{G}_b) \\ \tilde{Y}_3 &= \tilde{H}_{33}\tilde{G}_b \end{aligned} \quad (2.43)$$

for the displacements \tilde{Y}_1 along the rails, \tilde{Y}_2 along the slab and \tilde{Y}_3 along the tunnel invert. The applied point load is equivalent to a force per unit length of $F = \delta(x)$, which gives $\tilde{F} = 1$ when transformed [6]. The functions \tilde{H}_{11} and \tilde{H}_{22} are the FRFs in the wavenumber domain for the response of a free beam to a point load at $x = 0$ for the two rails and the slab respectively. The function \tilde{H}_{33} is the FRF for the response of the uncoupled tunnel invert to a point load at $x = 0$ in the wavenumber domain. These FRFs will be derived in section 2.2.2.

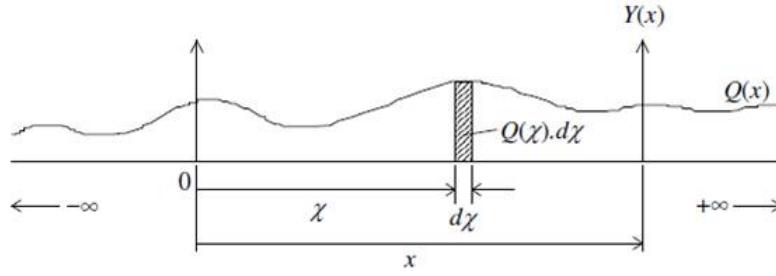


FIGURE 2.6: General force distribution per unit length $Q(x)$ acting along a single line of joining. The displacement response $Y(x)$ is obtained by the convolution in space of the force increments $Q(\chi)d\chi$ with the frequency response function to a point load [6].

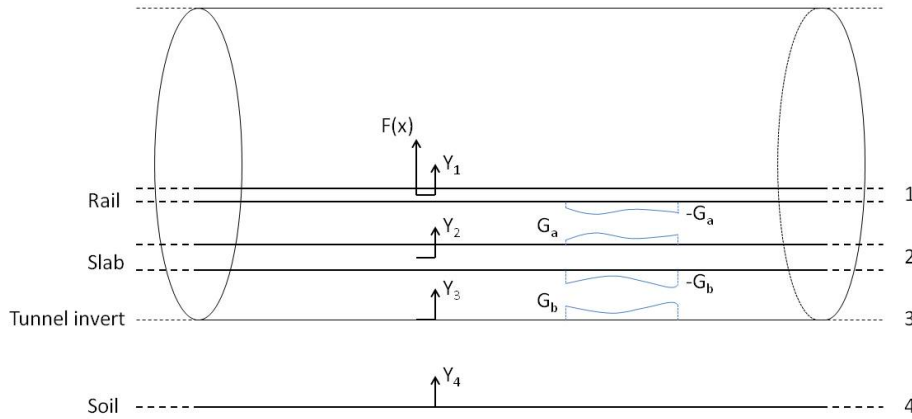


FIGURE 2.7: Schematic overview of floating slab track. The displacements and interaction forces acting on the rails, slab and tunnel are indicated.

The rails are connected to the slab via rail pads and the slab is connected to the tunnel invert via resilient slab bearings. The interaction force is determined by the extension of the bearings and the rail pads and their stiffness. The rail pads and bearings are modelled as continuous resilient layers of stiffness k_a and k_b respectively per unit length [6]. Damping can be included by using a complex stiffness. The joining condition between the rails and the slab results in

$$\tilde{G}_a = k_a(\tilde{Y}_1 - \tilde{Y}_2) \quad (2.44)$$

The joining condition between the slab and tunnel invert results in

$$\tilde{G}_b = k_b(\tilde{Y}_2 - \tilde{Y}_3) \quad (2.45)$$

Combining equations (2.43), (2.44) and (2.45) results in a system with five equations and five unknowns, namely \tilde{Y}_1 , \tilde{Y}_2 , \tilde{Y}_3 , \tilde{G}_a and \tilde{G}_b . By substituting equations (2.44) and (2.45) into equations (2.43) the displacements can be found. The solutions for \tilde{Y}_1 , \tilde{Y}_2 and \tilde{Y}_3 are given in Appendix C. The forces can then be easily derived from (2.44) and (2.45). Especially the force acting on the tunnel invert will be of interest and is given by

$$\tilde{G}_b = \frac{\tilde{Y}_3}{\tilde{H}_{33}} \quad (2.46)$$

The response along a line in the soil parallel to the joining line can be determined once this interaction force is known. The soil displacement is given by

$$\tilde{Y}_4 = \tilde{H}_{43}\tilde{G}_b \quad (2.47)$$

where \tilde{H}_{43} is the FRF of a particular soil displacement component \tilde{Y}_4 to a unit load acting on the uncoupled tunnel invert at $x = 0$ as described in section 2.1. The displacement in the space domain can be found by using the second expression of the transform pair (2.41). For the unit point load assumed here, the physical displacement in the space domain represents the FRF of the combined system for a point load acting at $x = 0$ on the rail [6]:

$$\tilde{H}_{41} = \tilde{Y}_4(\tilde{F} = 1) \quad (2.48)$$

2.2.2 Frequency response functions

The frequency response functions used in previous section still have to be determined. First the FRFs for the rails and the slab will be determined followed by the FRFs for the tunnel invert and the soil.

Both the slab and the rails are modelled as free beams of infinite length. In the calculations the two rails will be modelled as one beam. The equation of motion of a free beam in bending is given by [17]

$$m \frac{\partial^2 y}{\partial t^2} + EI \frac{\partial^4 y}{\partial x^4} = f(x, t) \quad (2.49)$$

where m is the mass per unit length, EI is the bending stiffness (E is Young's modulus and I is the second moment of area) and $f(x, t)$ is the applied force per unit length. The FRF can be determined by substituting a harmonic solution $y = \tilde{Y} e^{i(\omega t + \xi x)}$ with a force $f = \tilde{F} e^{i(\omega t + \xi x)}$ into the equation of motion (2.49). This yields

$$-m\omega^2 \tilde{Y} e^{i(\omega t + \xi x)} + EI \xi^4 \tilde{Y} e^{i(\omega t + \xi x)} = \tilde{F} e^{i(\omega t + \xi x)} \quad (2.50)$$

Rearranging and eliminating the terms $e^{i(\omega t + \xi x)}$ gives the FRF in the wavenumber domain:

$$\tilde{H}_{\text{free beam}} = \frac{\tilde{Y}}{\tilde{F}} = \frac{1}{EI \xi^4 - m\omega^2} \quad (2.51)$$

Using harmonic solutions in this way is equivalent to taking the Fourier transform of (2.49) twice, once for time to frequency domain and once for space to wavenumber domain. The FRF $\tilde{H}_{\text{free beam}}$ is equal to the displacement \tilde{Y} if the applied force is a unit spatial point load acting at $x = 0$, thus $\tilde{F} = 1$ [6].

The FRF \tilde{H}_{11} for the rails is found by using the mass per unit length m_1 and the bending stiffness EI_1 for the two rails together:

$$\tilde{H}_{11} = \tilde{H}_{\text{free beam}}(m_1, EI_1) \quad (2.52)$$

Using the mass per unit length m_2 and the bending stiffness EI_2 results in the FRF for the slab:

$$\tilde{H}_{22} = \tilde{H}_{\text{free beam}}(m_2, EI_2) \quad (2.53)$$

The FRFs for the tunnel invert and the soil are determined by applying a spatial unit point load on the invert and calculating the displacements in the tunnel or at a particular point in the soil. It is assumed that forces normal to the tunnel invert will have the most important effect on the dynamic behaviour of the tunnel and the soil [6]. Therefore, the longitudinal and tangential applied forces are set to zero. The spatial variation of such a point load is shown in Figure 2.8.

The solutions for the cylindrical shell equation (2.6) and the elastic continuum equation (2.20) are expressed in the wavenumber-frequency domain for a particular circumferential mode number n . Thus an expression for the unit point load has to be determined in the wavenumber-frequency domain.

As in the PIP model, the coordinate system for the cylindrical shell will be used. The vector $\tilde{\mathbf{P}}_n$ in equation (2.21) contains stresses, while the normal point load here is a force. To ensure that the stresses correspond with a unit load, the load is visualised as a three-dimensional rectangular pulse centered on the position $x = 0$ and $\theta = 0$ of small base side-lengths Δx and $a\Delta\theta$, and height $1/a\Delta\theta\Delta x$ [6]. This pulse can be considered as the product of two separate rectangular pulses in x and θ , as depicted in Figure 2.8. The point load is achieved in the limit as Δx and $\Delta\theta$ tend to zero. Written out, the applied stress for a unit point load in the space-time domain is

$$\begin{aligned} p_x &= p_y = 0 \\ p_z &= \begin{cases} \frac{1}{a\Delta\theta\Delta x} e^{i\omega t} & \text{for } -\frac{\Delta x}{2} \leq x \leq \frac{\Delta x}{2} \text{ and } -\frac{\Delta\theta}{2} \leq \theta \leq \frac{\Delta\theta}{2} \\ 0 & \text{otherwise} \end{cases} \\ &\rightarrow \frac{\delta(x)\delta(\theta)}{a} e^{i\omega t} \quad \text{as } \Delta x, \Delta\theta \rightarrow 0 \end{aligned} \quad (2.54)$$

where $\delta(x)$ and $\delta(\theta)$ are Dirac delta functions [6]. Forrest transformed this into the wavenumber-frequency domain. For a particular circumferential mode number n and for all ξ , the stresses are given by [6]

$$\begin{aligned} \tilde{P}_{xn} &= 0 \\ \tilde{P}_{yn} &= 0 \\ \tilde{P}_{zn} &= \begin{cases} 1/2\pi a, & n = 0 \\ 1/2\pi a, & n \geq 1 \end{cases} \end{aligned} \quad (2.55)$$

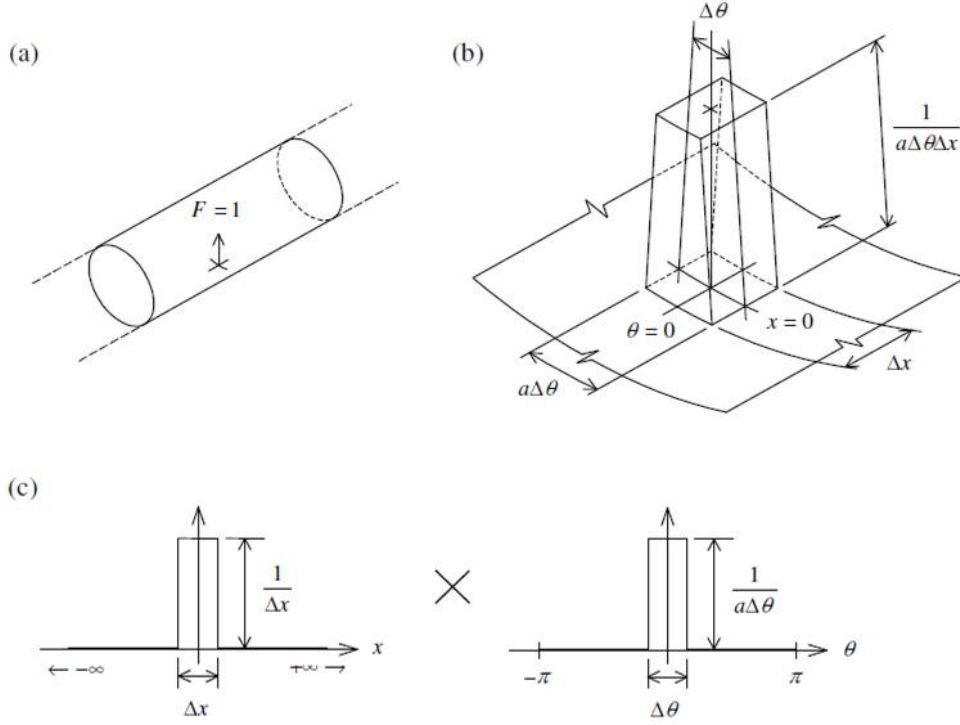


FIGURE 2.8: (a) A unit normal point force acting on the invert of an infinitely long tunnel can be construed as (b) an appropriately scaled uniform normal stress acting over a small rectangular area centered on $x = 0$ and $\theta = 0$. This normal stress distribution can be decomposed into (c) the product of two rectangular pulse functions, one in x and one in θ [6].

The harmonic displacements $\{\tilde{U}_n \ \tilde{V}_n \ \tilde{W}_n\}^T$ are calculated for each value of n from equation (2.28) by applying the stresses (2.55). The total displacements $\tilde{U} = \{\tilde{U} \ \tilde{V} \ \tilde{W}\}^T$ at a particular radius r and angular position θ resulting from a time harmonic unit point load acting on the invert are given by a linear combination of these spatially harmonic components:

$$\begin{Bmatrix} \tilde{U} \\ \tilde{V} \\ \tilde{W} \end{Bmatrix}_r = \begin{Bmatrix} \tilde{U}_0 \\ 0 \\ \tilde{W}_0 \end{Bmatrix}_r + \sum_{n=1}^{\infty} \begin{Bmatrix} \tilde{U}_n \cos n\theta \\ \tilde{V}_n \sin n\theta \\ \tilde{W}_n \cos n\theta \end{Bmatrix}_r \quad (2.56)$$

The tunnel invert FRF \tilde{H}_{33} can now be determined from the displacement \tilde{W} for $r = a$ and $\theta = 0$. The soil FRF \tilde{H}_{43} can be one of the three displacement components, whichever is of interest, for any line in the soil defined by constant $r = R$ and $\theta = \beta$. These can be expressed as

$$\begin{aligned} \tilde{H}_{33} &= \tilde{W}(r = a, \theta = 0) \\ \tilde{H}_{43} &= \tilde{U}, \tilde{V} \text{ or } \tilde{W}(r = R, \theta = \beta) \end{aligned} \quad (2.57)$$

2.2.3 Adding axles masses

To simulate a train running over the track, masses are added at regular intervals along the track as depicted in Figure 2.5. These masses represent the axles of a train. Adding the masses to the model constructed so far is done in the space domain. Since the axles interact with the rail, the FRF $H_{11}(x)$ is required in the x -domain. This can be obtained by the inverse Fourier transform of the FRF in the ξ -domain given in (2.52)

$$H_{11}(x) = \frac{1}{2\pi} \int_{-\infty}^{\infty} \tilde{H}_{11}(\xi) e^{i\xi x} d\xi \quad (2.58)$$

The FRF $H_{41}(x)$ of the soil in the x -domain is required to find the final response in the soil. This can be obtained by the inverse Fourier transform of the FRF in the ξ -domain given in equation (2.48)

$$H_{41}(x) = \frac{1}{2\pi} \int_{-\infty}^{\infty} \tilde{H}_{41}(\xi) e^{i\xi x} d\xi \quad (2.59)$$

As the first step in the addition of axle masses, the rail responses at the positions where the masses are to be added must be formed into an FRF matrix \mathbf{H}_1 which satisfies

$$\mathbf{Y}_1 = \mathbf{H}_1 \mathbf{F}_1 \quad (2.60)$$

where \mathbf{Y}_1 is the vector of rail displacements at the locations where masses will be added and \mathbf{F}_1 is the vector of forces acting at those positions on the rail [6]. The elements of the matrix \mathbf{H}_1 are determined by the rail displacement FRF $H_{11}(x)$.

The case of adding only five masses will be considered here as an example of the general approach. It can easily be extended to more added masses to give the convergence necessary to model an infinitely long train. Due to the infinite length and the symmetry of the track and tunnel, the rail FRF is only dependent on the magnitude of the separation between the position where the displacement is wanted and the position of the load as described in the introduction of this section. For a regular spacing L of the positions where the masses will be added, the rail FRF matrix is

$$\mathbf{H}_1 = \begin{bmatrix} H_{11}(0) & H_{11}(L) & H_{11}(2L) & H_{11}(3L) & H_{11}(4L) \\ H_{11}(L) & H_{11}(0) & H_{11}(L) & H_{11}(2L) & H_{11}(3L) \\ H_{11}(2L) & H_{11}(L) & H_{11}(0) & H_{11}(L) & H_{11}(2L) \\ H_{11}(3L) & H_{11}(2L) & H_{11}(L) & H_{11}(0) & H_{11}(L) \\ H_{11}(4L) & H_{11}(3L) & H_{11}(2L) & H_{11}(L) & H_{11}(0) \end{bmatrix} \quad (2.61)$$

To add the axle masses, the FRF matrix \mathbf{H}_1 is inverted, what results in the dynamic stiffness matrix (DSM) expression

$$\mathbf{F}_1 = [\mathbf{H}_1]^{-1} \mathbf{Y}_1 = \mathbf{K}_1 \mathbf{Y}_1 \quad (2.62)$$

Axles are then added to the model as concentrated masses m_a by adding inertia terms of the form $-m_a \omega^2 Y$, where Y is the displacement at the axle's position, to the appropriate diagonal elements of \mathbf{K}_1 , leaving the centre station free [6]. The

axle mass at the centre station is added via a roughness displacement $\delta = \Delta e^{i\omega t}$, as shown in Figure 2.5. The overall matrix equation then becomes

$$\begin{bmatrix} k_{11} - m_a\omega^2 & k_{12} & k_{13} & k_{14} & k_{15} & 0 \\ k_{21} & k_{22} - m_a\omega^2 & k_{23} & k_{24} & k_{25} & 0 \\ k_{31} & k_{32} & k_{33} & k_{34} & k_{35} & -m_a\omega^2 \\ k_{41} & k_{42} & k_{43} & k_{44} - m_a\omega^2 & k_{45} & 0 \\ k_{51} & k_{52} & k_{53} & k_{54} & k_{55} - m_a\omega^2 & 0 \\ 0 & 0 & -1 & 0 & 0 & 1 \end{bmatrix} \begin{Bmatrix} Y_1 \\ Y_2 \\ Y_3 \\ Y_4 \\ Y_5 \\ Y_a \end{Bmatrix} = \begin{Bmatrix} 0 \\ 0 \\ 0 \\ 0 \\ 0 \\ \delta \end{Bmatrix} \quad (2.63)$$

where k_{ij} is the element on row i and column j of \mathbf{K}_1 . Equation (2.63) is of order one greater than the original DSM because of the extra displacement component Y_a introduced by the independent axle mass at the centre.

From equation (2.63) the displacements $\mathbf{Y}_1 = \{Y_1 \ Y_2 \ Y_3 \ Y_4 \ Y_5\}^T$ of the rail at the axle masses are calculated. These displacements are substituted back into (2.62) to obtain the interaction forces \mathbf{F}_1 acting on the rail at the positions of the axle masses. Once these forces are known, the soil displacements \mathbf{Y}_4 can be found from the FRF function $H_{41}(x)$. In matrix form this can be expressed as

$$\mathbf{Y}_4 = \mathbf{H}_4 \mathbf{F}_1 \quad (2.64)$$

where \mathbf{H}_4 is the FRF matrix for the soil line to input forces acting on the rail with no axle masses added. For the tangential and radial components of soil displacements, V and W , \mathbf{H}_4 has the same form as \mathbf{H}_1 given by (2.61), but with $H_{41}(x)$ instead of $H_{11}(x)$. This is because these components are even functions of x for a vertical load applied at $x = 0$. However, the longitudinal component U is an odd function of x for such a load, so that the sign of the longitudinal separation between a given load and displacement is important. The soil FRF matrix is then

$$\mathbf{H}_4 = \begin{bmatrix} H_{41}(0) & -H_{41}(L) & -H_{41}(2L) & -H_{41}(3L) & -H_{41}(4L) \\ H_{41}(L) & H_{41}(0) & -H_{41}(L) & -H_{41}(2L) & -H_{41}(3L) \\ H_{41}(2L) & H_{41}(L) & H_{41}(0) & -H_{41}(L) & -H_{41}(2L) \\ H_{41}(3L) & H_{41}(2L) & H_{41}(L) & H_{41}(0) & H_{41}(L) \\ H_{41}(4L) & H_{41}(3L) & H_{41}(2L) & H_{41}(L) & H_{41}(0) \end{bmatrix} \quad (2.65)$$

2.2.4 Power spectral density calculations

A last step in the PiP model is the calculation of the power spectral density of the soil displacements. Since the roughness and other irregularities of the real rail and wheel surface profiles will be randomly distributed, the roughness displacement inputs at the wheel of a train travelling on the track will be random processes. Therefore, the calculation of the resultant soil responses requires the use of the theory of random vibration [6].

The PiP model is considered as a system with N stationary random inputs x_j , the axle inputs, and one stationary random output y , the displacement response of a

particular point in the soil. The power spectral density (PSD) $S_y(\omega)$ of the output y is then given by

$$S_y(\omega) = \sum_{p=1}^N \sum_{q=1}^N H_p^*(\omega) H_q(\omega) S_{x_p x_q}(\omega) \quad (2.66)$$

where $H_p(\omega)$ and $H_q(\omega)$ are the FRFs of y to the inputs x_p and x_q respectively and $S_{x_p x_q}(\omega)$ is the cross spectral density between the two inputs [6]. $H_p^*(\omega)$ is the complex conjugate of $H_p(\omega)$.

The train's wheels are assumed to be perfectly smooth, so that all irregularities are contained in the rail surface, the axle inputs can be assumed to differ by a time delay only. Therefore, the statistical properties of the different inputs are the same, thus have the same spectrum $S_0(\omega)$. However for two inputs, say x_1 and x_2 , one lags the other such that $x_2(t) = x_1(t - T)$. In this case the cross spectra are given by [6]

$$\begin{aligned} S_{x_1 x_2}(\omega) &= S_0(\omega) e^{-i\omega T} \\ S_{x_2 x_1}(\omega) &= S_0(\omega) e^{i\omega T} \end{aligned} \quad (2.67)$$

The time delay between two adjacent axles is $T = L/v$, where L is the axle spacing and v is the train's speed. If the axles are not adjacent, this time delay is multiplied by the integer difference $(q - p)$. q and p are the indices of the axles concerned. The general formula (2.66) for the output spectrum can be rewritten as

$$S_y(\omega) = \sum_{p=1}^N \sum_{q=1}^N H_p^*(\omega) H_q(\omega) S_0(\omega) e^{-i\omega(q-p)L/v} \quad (2.68)$$

The FRFs $H_p(\omega)$ and $H_q(\omega)$ can be obtained from the appropriate elements of the soil response vector \mathbf{Y}_4 in (2.64). The soil response vector is calculated for an input at the centre axle mass only, thus the shifting principle has to be used. For example, consider a train with 5 axles as in section 2.2.3. The spectra of the soil displacement at $x = 0$ is wanted. The FRF $H_2(\omega)$ is equal to the displacement in the soil at $x = 0$ for an input roughness on the track at $x = -L$. Due to the shifting principle this is the same as the displacement at $x = L$ for an input on the track at $x = 0$, thus $H_2(\omega) = Y_4$. The other FRFs can be found in a similar way and used in equation (2.68) to obtain the PSD. The real model should include N axle masses instead of just five, where N is sufficiently large for convergence of the soil responses so that the shifting principle is valid.

In version 3 of the PiP model the power spectral density is calculated for uncorrelated inputs using a white input roughness spectrum of $S_0 = 1 \text{ mm}^2/\text{Hz}$. Equation (2.68) can be simplified to

$$S_y(\omega) = \sum_{p=1}^N |H_p(\omega)|^2 \quad (2.69)$$

The FRFs $H_p(\omega)$ are obtained as before.

To calculate the response of the building model described in Chapter 3 the vertical displacement component is needed as an input to the building's foundation. However, the displacements here are expressed as longitudinal, tangential and radial

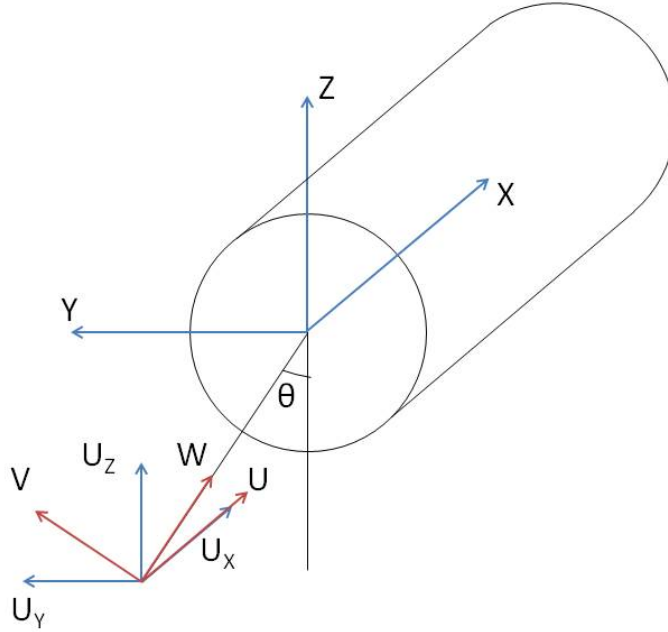


FIGURE 2.9: Relationship between the shell coordinates and the global coordinates. The displacement components U , V and W in shell coordinates and displacement components U_X , U_Y and U_Z in global coordinates are indicated.

components U , V and W due to the cylindrical geometry of the PiP model. To obtain horizontal and vertical components, an absolute coordinate system XYZ needs to be defined. The longitudinal direction X coincides with the longitudinal x -axis of the tunnel, the horizontal direction Y with the $\theta = 90^\circ$ radius, and the vertical direction Z with the $\theta = 180^\circ$ radius as shown in Figure 2.9. The relationship of the longitudinal, horizontal and vertical displacement components U_X , U_Y and U_Z to the original components U , V and W are

$$\begin{Bmatrix} U_X \\ U_Y \\ U_Z \end{Bmatrix} = \begin{bmatrix} 1 & 0 & 0 \\ 0 & \cos \theta & -\sin \theta \\ 0 & \sin \theta & \cos \theta \end{bmatrix} \begin{Bmatrix} U \\ V \\ W \end{Bmatrix} \quad (2.70)$$

The FRFs can be calculated for the U , V and W components of soil displacement and then transformed with (2.70) before being used in the PSD equation (2.68) or (2.69).

2.3 Conclusion

The Pipe in Pipe model is a computationally efficient model to simulate vibrations due to underground railways. The model can be divided into two parts: modelling

the tunnel and modelling the track. The tunnel and track are assumed to be straight and infinitely long.

The tunnel can be modelled as a thin cylindrical shell or a thick cylindrical shell. The soil is modelled as an elastic continuum with a cylindrical cavity. Due to the cylindrical geometry of the problem a cylindrical coordinate system is used.

Floating slab tracks are frequently used for underground railways. Two rails are mounted via rail pads and rail fasteners onto a massive concrete slab, which in turn rests on slab bearings supported by the tunnel invert. The purpose of the rail pads, track slab and the slab bearings is to provide vibration isolation to the tunnel invert from the track. The rails and the slab are modelled as infinite beams and coupled to the tunnel in the wavenumber-frequency domain.

A train running through the tunnel can be modelled by adding masses at regular intervals on the track. The masses represent the axle loads of the train. Because the irregularities of the rail and wheel will be randomly distributed, theory of random vibration will be used to calculate the power spectral density of the displacement response of the soil.

Chapter 3

Modelling of a multistory building

In this chapter a two-dimensional building model is presented. The building is modelled as a portal frame with a number of columns and floors. The dynamic stiffness matrix method is used to model this portal frame. The building rests on a pile foundation and the soil-structure interaction is accounted for by using Novak's model for pile foundations. In section 3.2 a finite model for a building will be presented. To further reduce the computation time, an infinite model is assembled in section 3.3. The two models are compared in section 3.4. Finally the model is validated by comparing it to a similar building model that is presented by Cryer [4].

3.1 Dynamic stiffness method

The model for the building has to be representative for the structures under investigation, but the computation time has to be limited so that it can be used in combination with the PiP model.

Building models can be formulated in either the time or frequency domain. "Models in the time domain are often used for the seismic analysis of structures where peak vibration levels due to a transient event are of interest." When dealing with ground-borne vibrations due to underground railways, however, the problem may be treated as linear because the strain amplitudes are low. For linear problems the frequency domain is the most appropriate and thus the model presented here will be formulated in the frequency domain [21].

The finite element method (FEM) is the most widely used numerical technique to model vibration of buildings. It is a powerful tool enabling the analysis of virtually any structure. However, the FEM requires considerable computing power to achieve reasonable results.[21].

Analytical models often require less computing power. A base-isolated building, for example, can be modelled as a standard single degree of freedom oscillator. This represents the isolated building as a rigid mass supported on a spring and a damping element to represent the isolation bearing. "Despite its popularity, the value of the

SDOF model is limited because it fails to describe some of the major features of a building's dynamic behaviour, in particular the flexibility and damping properties of the building and the effects of its foundation" [21].

In his PhD, Cryer [4] takes the analytical models one stage further by using the dynamic stiffness method to model a two-dimensional portal frame building resting on a three-dimensional piled foundation. The dynamic stiffness method accounts for both the longitudinal and transverse behaviour of the columns and floors of the building and the foundation model, based on a series of Novak piles, accounts for the interaction between the building and the ground. The computation time is minimized by treating the building as infinitely long and using periodic structure theory [4]. This approach will also be used in this dissertation, mainly due to its computationally efficiency.

The dynamic stiffness method involves dividing the building into a number of substructures, a wall or a floor for example. The response of each substructure is calculated using the analytical solutions of the equations of motion for that particular substructure. These responses are then assembled to evaluate the overall response of the model to a set of specified inputs.

3.1.1 Beam element

The building model presented here consists of floors and columns modelled as beams. The response of each beam is determined separately using its equations of motion and these responses are then combined to calculate the overall response of the building model. It is assumed that the beam behaves as an elastic bar in compression and an Euler beam in bending. There is no coupling between the two types of motion and consequently, the longitudinal and lateral vibration can be analysed independently [4]. Figure 3.1 and Figure 3.2 show the displacements and rotations and corresponding forces and moments of a beam. A typical element from a two dimensional portal frame is defined by its length L , cross-sectional area A , second moment of inertia I , density ρ and Young's modulus E .

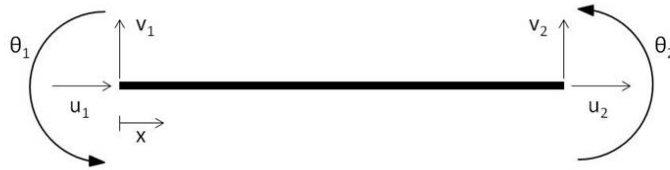


FIGURE 3.1: Displacements and Rotations.

The equation of motion governing undamped, longitudinal motion of an elastic bar is given by [17]:

$$\frac{\partial^2 u}{\partial t^2} - \frac{E}{\rho} \frac{\partial^2 u}{\partial x^2} = 0 \quad (3.1)$$



FIGURE 3.2: Forces and Moments.

A solution will be sought in the frequency domain. First equation (3.1) has to be transformed into the frequency domain. This can be done by taking the Fourier transform. A harmonic solution of the form $u(x, t) = U(x, \omega)e^{i\omega t}$ can be substituted into equation (3.1). This results in

$$-\omega^2 U e^{i\omega t} - \frac{E}{\rho} \frac{d^2 U}{dx^2} e^{i\omega t} = 0 \quad (3.2)$$

This can be rewritten as

$$\frac{\partial^2 U}{\partial x^2} + \alpha^2 U = 0 \quad \text{with} \quad \alpha^2 = \omega^2 \frac{\rho}{E} \quad (3.3)$$

This is a differential equation in the frequency domain for which the solution is known:

$$U(x, \omega) = c_1 e^{i\alpha x} + c_2 e^{-i\alpha x} \quad (3.4)$$

where $i^2 = -1$ and the constants c_1 and c_2 have to be determined from the boundary conditions. The normal force acting on the cross section at x is obtained by differentiating equation (3.4):

$$F = AE \frac{\partial U}{\partial x} = AE \left(i\alpha c_1 e^{i\alpha x} - i\alpha c_2 e^{-i\alpha x} \right) \quad (3.5)$$

For an Euler beam, the undamped equation of motion is [17]:

$$\frac{\partial^2 v}{\partial t^2} + \frac{EI}{\rho A} \frac{\partial^4 v}{\partial x^4} = 0 \quad (3.6)$$

Substituting a harmonic solution $v(x, t) = V(x, \omega)e^{i\omega t}$ results in a differential equation in the frequency domain:

$$\frac{d^4 V}{dx^4} - \beta^4 V = 0 \quad \text{with} \quad \beta^4 = \omega^2 \frac{\rho A}{EI} \quad (3.7)$$

The general solution of this differential equation is

$$V(x, \omega) = c_3 e^{\beta x} + c_4 e^{i\beta x} + c_5 e^{-\beta x} + c_6 e^{-i\beta x} \quad (3.8)$$

where the constants c_3 to c_6 have to be determined. Successive differentiation of equation (3.8) gives the rotation Θ , the bending moment Q and the shear force S at point x :

$$\begin{aligned}\Theta &= \frac{\partial V}{\partial x} = \beta c_3 e^{\beta x} + i\beta c_4 e^{i\beta x} - \beta c_5 e^{-\beta x} - i\beta c_6 e^{-i\beta x} \\ Q &= EI \frac{\partial^2 V}{\partial x^2} = EI \left(\beta^2 c_3 e^{\beta x} - \beta^2 c_4 e^{i\beta x} + \beta^2 c_5 e^{-\beta x} - \beta^2 c_6 e^{-i\beta x} \right) \\ S &= EI \frac{\partial^3 V}{\partial x^3} = EI \left(\beta^3 c_3 e^{\beta x} - i\beta^3 c_4 e^{i\beta x} - \beta^3 c_5 e^{-\beta x} + i\beta^3 c_6 e^{-i\beta x} \right)\end{aligned}\quad (3.9)$$

The generalised forces and displacements are related through the following boundary conditions at the ends of the element:

$$U = U_1, \quad V = V_1, \quad \Theta = \Theta_1, \quad F = -F_1, \quad S = S_1, \quad Q = -Q_1 \quad \text{at } x = 0 \quad (3.10a)$$

$$U = U_2, \quad V = V_2, \quad \Theta = \Theta_2, \quad F = F_2, \quad S = -S_2, \quad Q = Q_2 \quad \text{at } x = L \quad (3.10b)$$

By combining the above equations, the following matrix equations can be assembled:

$$\begin{pmatrix} U_1 \\ V_1 \\ \Theta_1 \\ U_2 \\ V_2 \\ \Theta_2 \end{pmatrix} = \begin{bmatrix} 1 & 1 & 0 & 0 & 0 & 0 \\ 0 & 0 & 1 & 1 & 1 & 1 \\ 0 & 0 & \beta & i\beta & -\beta & -i\beta \\ e^{i\alpha L} & e^{-i\alpha L} & 0 & 0 & 0 & 0 \\ 0 & 0 & e^{\beta L} & e^{i\beta L} & e^{-\beta L} & e^{-i\beta L} \\ 0 & 0 & \beta e^{\beta L} & i\beta e^{i\beta L} & -\beta e^{-\beta L} & -i\beta e^{-i\beta L} \end{bmatrix} \begin{pmatrix} c_1 \\ c_2 \\ c_3 \\ c_4 \\ c_5 \\ c_6 \end{pmatrix}$$

or

$$\mathbf{U}_l = \mathbf{M}\mathbf{c} \quad (3.11)$$

and

$$\begin{pmatrix} F_1 \\ S_1 \\ Q_1 \\ F_2 \\ S_2 \\ Q_2 \end{pmatrix} = \begin{bmatrix} -iAE\alpha & iAE\alpha & 0 & 0 & 0 & 0 \\ 0 & 0 & EI\beta^3 & -iEI\beta^3 & -EI\beta^3 & iEI\beta^3 \\ 0 & 0 & -EI\beta^2 & EI\beta^2 & -EI\beta^2 & EI\beta^2 \\ iAE\alpha e^{i\alpha L} & -iAE\alpha e^{-i\alpha L} & 0 & 0 & 0 & 0 \\ 0 & 0 & -EI\beta^3 e^{\beta L} & iEI\beta^3 e^{i\beta L} & EI\beta^3 e^{-\beta L} & -iEI\beta^3 e^{-i\beta L} \\ 0 & 0 & EI\beta^2 e^{\beta L} & -EI\beta^2 e^{i\beta L} & EI\beta^2 e^{-\beta L} & -EI\beta^2 e^{-i\beta L} \end{bmatrix} \begin{pmatrix} c_1 \\ c_2 \\ c_3 \\ c_4 \\ c_5 \\ c_6 \end{pmatrix}$$

or

$$\mathbf{F}_l = \mathbf{N}\mathbf{c} \quad (3.12)$$

The components of the generalised force vector \mathbf{F}_l and displacement vector \mathbf{U}_l are defined in the local coordinate system of the element. Their values are the complex amplitudes at the ends of the element.

Finally, eliminating \mathbf{c} from Equations (3.11) and (3.12) gives the local dynamic stiffness matrix \mathbf{K}_l of the element:

$$\mathbf{F}_l = \mathbf{K}_l \mathbf{U}_l, \quad \mathbf{K}_l = \mathbf{N}[\mathbf{M}]^{-1} \quad (3.13)$$

3.1.2 Novak's Model

The foundation assumed for the multistory building is a pile foundation. “Numerical solutions of dynamic pile foundation models, such as those based on the boundary element method or the finite element method, generally offer robustness” [13]. However, these methods often have excessive computation times, making them unsuitable for this application.

As mentioned before, the wavefield produced by an underground railway consists of low strain levels, for which it has been shown that the assumption of linear soil behaviour is justified. Hence the foundation model presented here is based upon the treatment of the soil as a linear, elastic continuum. Novak formulated an approximate solution for a single pile embedded in an elastic halfspace [18]. Novak's model assumes that the soil is made up of an infinite number of infinitesimally thin, independent, horizontal, elastic layers that extend to infinity. Compatibility between adjacent layers is only satisfied very far from the pile, and at the pile, where a perfect bond exists between the pile and the soil. This corresponds to the plane strain case. The motion of the pile and the soil is limited to either the vertical or the horizontal plane, depending on the direction of excitation. This approach results in a closed-form solution for the dynamic soil reaction per unit length of the pile [13].

Kuo [13] concluded that the Novak model is a computationally efficient model, but the plane strain assumption makes the Novak model ineffective in certain situations. The most notable of these are the lateral response of a pile to an incident wavefield. However, the short running time and the good representation of the axial pile response makes it suitable for this application.

As for the beam in section 3.1.1, the pile is modelled as a bar in axial vibration or an Euler beam in lateral vibration. The pile is embedded in the soil that is represented by infinitesimal horizontal soil layers as shown in Figure 3.3. The axial and lateral directions of motion are decoupled and the problem will be solved in the frequency domain.

For axial motion, the pile behaviour is governed by the equation [13]:

$$\frac{\partial^2 u}{\partial t^2} - \frac{E}{\rho} \frac{\partial^2 u}{\partial x^2} + \frac{N_x}{\rho A} = 0 \quad (3.14)$$

where ρ is the density of the pile, A the cross-sectional area, E Young's modulus. N_x is the vertical soil reaction force and is given by

$$N_x = GS_x u(x) \quad (3.15)$$

where G is the soil shear modulus, $u(x)$ is the axial displacement of the pile at position x .

As before, equation (3.14) is transformed into the frequency domain by substituting the harmonic solution $u(x, t) = U(x, \omega)e^{i\omega t}$. This results in a differential equation in the frequency domain for which the solution is known:

$$\frac{d^2 U}{dx^2} + \alpha_p^2 U = 0 \quad \text{with} \quad \alpha_p^2 = \omega^2 \frac{\rho}{E} - \frac{GS_x}{EA} \quad (3.16)$$

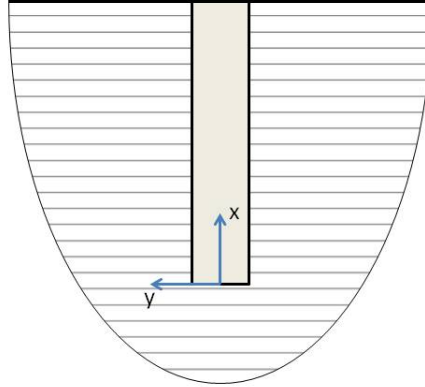


FIGURE 3.3: Novak's plane strain representation of a pile [13].

This is the same differential equation as for the beam in section 3.1 except for the term α_p which now include the soil reaction. S_x is given by [13]

$$S_x = 2\pi a_0 \frac{J_1(a_0)J_0(a_0) + Y_1(a_0)Y_0(a_0)}{J_0^2(a_0) + Y_0^2(a_0)} + \frac{4i}{J_0^2(a_0) + Y_0^2(a_0)} \quad (3.17)$$

where a_0 is the dimensionless frequency parameter, given by

$$a_0 = a\omega \sqrt{\frac{\rho_s}{G}} \quad (3.18)$$

$J_0(a_0)$ and $J_1(a_0)$ are Bessel functions of the first kind of order zero and one respectively, $Y_0(a_0)$ and $Y_1(a_0)$ are Bessel functions of the second kind of order zero and one respectively, ρ_s is the soil density, a is the pile radius and ω is the angular frequency of interest.

The general solution for the displacements in the x -direction in the frequency domain is:

$$U(x, \omega) = d_1 e^{i\alpha_p x} + d_2 e^{-i\alpha_p x} \quad (3.19)$$

where the coefficients d_1 and d_2 are determined using the boundary conditions at the ends of the pile.

For lateral motion, the pile behaviour is governed by the equation [13]:

$$\frac{\partial^2 v}{\partial t^2} + \frac{EI}{\rho A} \frac{\partial^4 v}{\partial x^4} + \frac{N_y}{\rho A} = 0 \quad (3.20)$$

N_y is the horizontal soil reaction and is given by

$$N_y = GS_y v(x) \quad (3.21)$$

where $v(x)$ is the lateral displacement of the pile at position x .

Substituting the harmonic solution $v(x, t) = V(x, \omega)e^{i\omega t}$ results in a differential equation in the frequency domain:

$$\frac{d^4 V}{dx^4} - \beta_p^4 V = 0 \quad \text{with} \quad \beta_p^4 = \frac{\rho A \omega^2 - G S_y}{EI} \quad (3.22)$$

This the same differential equation as for the lateral motion of the beam in section 3.1 except for the term β_p which now includes the soil reaction. S_y is given by [13]

$$S_y = 2\pi a_0 \frac{\frac{1}{\sqrt{q}} H_2^{(2)}(a_0) H_1^{(2)}(x_0) + H_1^{(2)}(x_0) H_1^{(2)}(a_0)}{H_0^{(2)}(a_0) H_2^{(2)}(x_0) + H_0^{(2)}(x_0) H_2^{(2)}(a_0)} \quad (3.23)$$

where $H_0^{(2)}(a_0)$ and $H_1^{(2)}(a_0)$ are Hankel functions of the second kind,

$$q = \frac{1 - 2\nu_s}{2(1 - \nu_s)}, \quad (3.24)$$

ν_s is the Poisson ratio of the soil and

$$x_0 = \sqrt{q} a_0 \quad (3.25)$$

The general solution for the displacements in the x -direction in the frequency domain is:

$$V(x, \omega) = d_3 e^{\beta_p x} + d_4 e^{i\beta_p x} + d_5 e^{-\beta_p x} + d_6 e^{-i\beta_p x} \quad (3.26)$$

where the coefficients d_3 to d_6 are determined using the boundary conditions at the ends of the pile.

Using the boundary conditions given in (3.10) and the general solutions for the displacements (3.19) and (3.26), following matrix equations can be assembled:

$$\mathbf{U}_p = \mathbf{M}_p \mathbf{d} \quad (3.27)$$

and

$$\mathbf{F}_p = \mathbf{N}_p \mathbf{d} \quad (3.28)$$

where the vectors \mathbf{U}_p and \mathbf{F}_p and the matrices \mathbf{M}_p and \mathbf{N}_p have the same form as in equations (3.11) and (3.12). The components of the generalised force and displacement vectors are defined in the local coordinates of the element. Their values are the complex amplitudes at the ends of the pile.

Finally, eliminating \mathbf{d} from equations (3.27) and (3.28) gives the local dynamic stiffness matrix \mathbf{K}_p of the pile:

$$\mathbf{F}_p = \mathbf{K}_p \mathbf{U}_p, \quad \mathbf{K}_p = \mathbf{N}_p [\mathbf{M}_p]^{-1} \quad (3.29)$$

3.1.3 Damping

Material damping is included in the building and the piles, and the soil model includes both radiation and material damping. In both cases the material damping is included using a frequency independent, hysteretic damping ratio. This differs for the building model used by Cryer [4] who used Rayleigh damping which is frequency dependent. The radiation damping is accounted for by the use of Bessel and Hankel functions in equations (3.17) and (3.23)

“Material damping is modelled in the frequency domain by representing the material as a viscoelastic continuum and accounting for damping by replacing the standard elastic constants with suitable complex values” [2]. For example, Young’s modulus E becomes $E(1 + i\eta_E)$, where η_E is the damping loss factor. In general, the damping loss factor is a function of frequency, but is often found to be approximately constant in practice [21].

“Laboratory experiments on various concrete columns described by Newland and Hunt [10] indicate that the variation in damping between columns with differing reinforcing configurations is small and that the loss factors are not strongly dependent on frequency, being of the order of 0.01. This supports the use of hysteretic damping to describe a single reinforced concrete column. However, it is unlikely that these results are appropriate for an entire building where damping may be an order of magnitude greater than the material damping. The extra damping is believed to be due to boundary damping arising at structural joints and radiation into foundations. Such damping is less easy to model than material damping. In practice, the model adopted for material damping is usually assumed to extend to boundary damping if the damping is small” [21].

3.2 Finite building model

Once the dynamic stiffness matrices of all elements of the building have been calculated, they must be assembled together to reflect the physical connections between the elements. In Figure 3.4 a building is shown with 9 columns and 5 floors.

Elements in the model are joined at points called nodes each of which has three degrees of freedom: horizontal displacement, vertical displacement and rotation. External forces and moments may only be applied at nodes and must be in equilibrium with the stresses at that node. The resulting set of equilibrium equations may be written in matrix form as follows. The set of external forces F_r^x and F_r^y , and moments M_r applied at the nodes are used to form a single vector \mathbf{F}_G where $\mathbf{F}_G = \{F_1^x \ F_1^y \ M_1 \ F_2^x \ F_2^y \ M_2 \ \dots \ F_n^x \ F_n^y \ M_n\}^T$ for example. Similarly, the corresponding displacements U_r and V_r , and rotations Θ_r are used to form a vector \mathbf{U}_G where $\mathbf{U}_G = \{U_1 \ V_1 \ \Theta_1 \ \dots \ U_n \ V_n \ \Theta_n\}^T$. These two vectors are related by the dynamic stiffness matrix of the entire model, \mathbf{K}_G , as

$$\mathbf{F}_G = \mathbf{K}_G \mathbf{U}_G \quad (3.30)$$

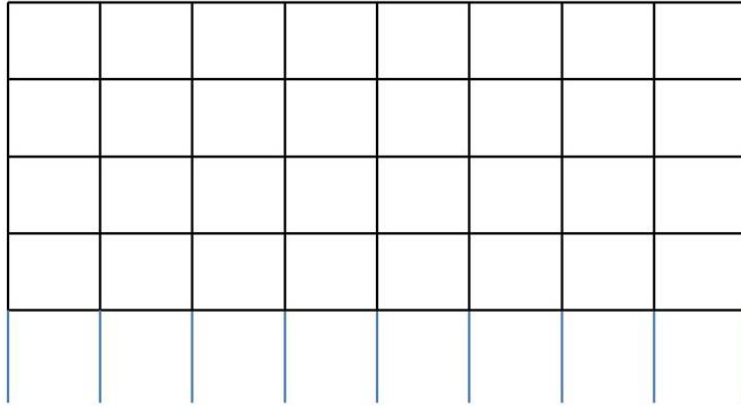


FIGURE 3.4: Finite building model with 9 columns and 5 horizontal floors.

Once K_G is known the response of the model to any set of input forces can be calculated by matrix inversion.

The global stiffness matrix K_G is assembled from the stiffness matrices of each of the elements that make up the model. Each entry in K_G is the sum of the stiffnesses of the elements connected to that node. This process is directly equivalent to the assembly of static stiffness matrices in finite element analysis. Each element's stiffness matrix must be transformed into a coordinate system common to the entire model before it is added to K_G . In two dimensions this transformation is simply a rotation from the local axes of the element to the global axes.

Consider an element inclined at some angle ϕ to the global horizontal, that is the x' -axis as shown in Figure 3.5. The generalised displacements can be transformed to

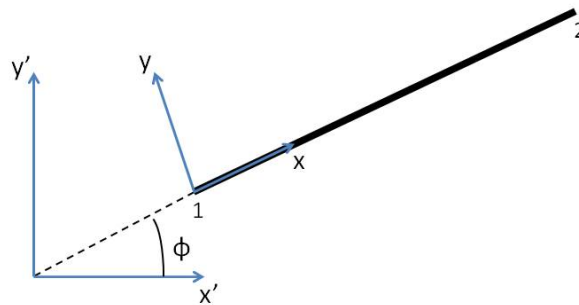


FIGURE 3.5: Transformation of the coordinate system

the global coordinate system [21]:

$$\begin{Bmatrix} U'_1 \\ V'_1 \\ \Theta'_1 \\ U'_2 \\ V'_2 \\ \Theta'_2 \end{Bmatrix} = \begin{bmatrix} \cos \phi & -\sin \phi & 0 & 0 & 0 & 0 \\ \sin \phi & \cos \phi & 0 & 0 & 0 & 0 \\ 0 & 0 & 1 & 0 & 0 & 0 \\ 0 & 0 & 0 & \cos \phi & -\sin \phi & 0 \\ 0 & 0 & 0 & \sin \phi & \cos \phi & 0 \\ 0 & 0 & 0 & 0 & 0 & 1 \end{bmatrix} \begin{Bmatrix} U_1 \\ V_1 \\ \Theta_1 \\ U_2 \\ V_2 \\ \Theta_2 \end{Bmatrix}$$

or

$$\mathbf{U}_g = \mathbf{R}\mathbf{U}_l \quad (3.31)$$

Similarly the generalized forces can be written in global coordinates:

$$\mathbf{F}_g = \mathbf{R}\mathbf{F}_l \quad (3.32)$$

Using this relationships, the global dynamic stiffness matrix \mathbf{K}_g of an element can be deduced:

$$\mathbf{F}_g = \mathbf{K}_g\mathbf{U}_g, \quad \mathbf{K}_g = \mathbf{R}\mathbf{K}_l[\mathbf{R}]^{-1} = \mathbf{R}\mathbf{K}_l[\mathbf{R}]^T \quad (3.33)$$

Once transformed, each element's stiffness matrix is added to the entries in \mathbf{K}_G that correspond to the degrees of freedom of the nodes which the element connects [4].

3.3 Infinite building model

To analyse a large building using the method described above requires a substantial amount of time. For the incorporation of a building into the PiP software, a more computationally efficient model is required.

A cross section through many buildings reveals a regular pattern of columns, walls and floors. Often a particular substructure is repeated a number of times throughout the building. Therefore, it is reasonable to investigate the response of such a substructure to obtain an estimate of the response of the entire building. Cryer [4] showed that when such a substructure is repeated infinitely in a horizontal direction, the total response agrees well with that of a real building. Using the periodic structure theory, a substructure that is repeated infinitely can be modelled. This analysis considers an infinite model as divided into three parts: two semi-infinite structures extending to the left and right respectively and a central structure to which these are connected (Figure 3.6) [4].

3.3.1 Analysis of a semi-infinite structure

Figure 3.7 shows a semi-infinite structure extending to the right. It is build up out of a unit comprising one column and five floors attached to it. Cryer [4] derived the stiffness matrix for this semi-infinite structure following the transfer matrix approach used by Mead [15] and Livesley [14] and this will be discussed in the following paragraphs.

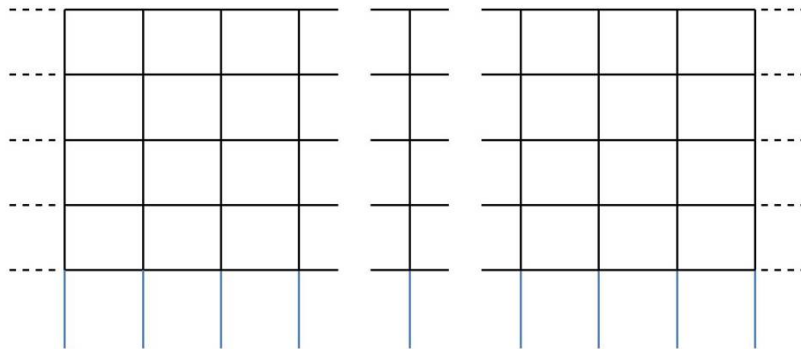


FIGURE 3.6: Infinite building model with 5 horizontal floors. The infinite model consists a semi-infinite structure extending to the left and a semi-infinite structure extending to the right connected to a central structure.

The repeated unit's stiffness matrix is assembled from the matrices of its constituent elements as described in section (3.2). Four different types of degree of freedom can be recognised in a unit: constrained degrees of freedom, degrees of freedom of nodes that are internal to the unit and degrees of freedom of nodes on the left and right hand sides of the unit which form the connections to adjacent units.

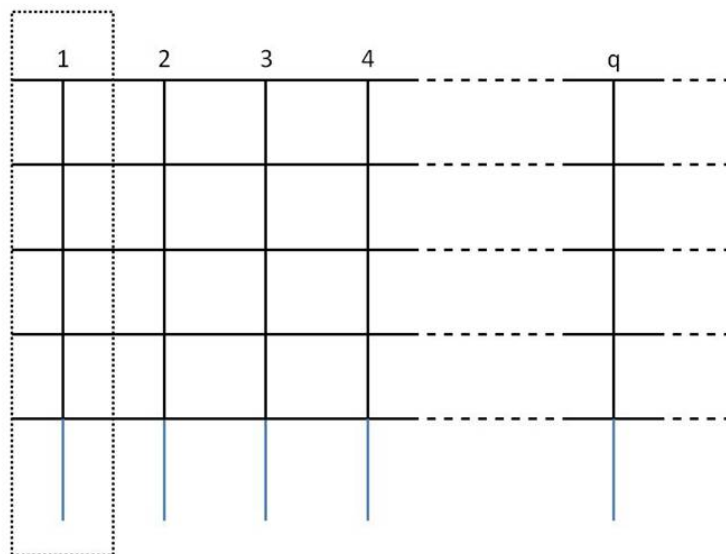


FIGURE 3.7: Diagram of a semi-infinite structure constructed from a repeated unit.

Therefore, the repeated unit's stiffness matrix can be partitioned as follows:

$$\begin{Bmatrix} \mathbf{F}_i \\ \mathbf{F}_l \\ \mathbf{F}_r \\ \mathbf{F}_c \end{Bmatrix} = \begin{bmatrix} \mathbf{K}_{ii} & \mathbf{K}_{il} & \mathbf{K}_{ir} & \mathbf{K}_{ic} \\ \mathbf{K}_{li} & \mathbf{K}_{ll} & \mathbf{K}_{lr} & \mathbf{K}_{lc} \\ \mathbf{K}_{ri} & \mathbf{K}_{rl} & \mathbf{K}_{rr} & \mathbf{K}_{rc} \\ \mathbf{K}_{ci} & \mathbf{K}_{cl} & \mathbf{K}_{cr} & \mathbf{K}_{cc} \end{bmatrix} \begin{Bmatrix} \mathbf{U}_i \\ \mathbf{U}_l \\ \mathbf{U}_r \\ \mathbf{U}_c \end{Bmatrix} \quad (3.34)$$

Subscript i indicates internal degrees of freedom, c constrained degrees of freedom, l and r degrees of freedom on the left and right hand sides of the unit.

The constrained degrees of freedom are not allowed to move, so $\mathbf{U}_c = 0$. The reactions at these points are not required in the analysis, so the stiffness matrix may be reduced in size and equation (3.34) rewritten as

$$\begin{Bmatrix} \mathbf{F}_i \\ \mathbf{F}_l \\ \mathbf{F}_r \end{Bmatrix} = \begin{bmatrix} \mathbf{K}_{ii} & \mathbf{K}_{il} & \mathbf{K}_{ir} \\ \mathbf{K}_{li} & \mathbf{K}_{ll} & \mathbf{K}_{lr} \\ \mathbf{K}_{ri} & \mathbf{K}_{rl} & \mathbf{K}_{rr} \end{bmatrix} \begin{Bmatrix} \mathbf{U}_i \\ \mathbf{U}_l \\ \mathbf{U}_r \end{Bmatrix} \quad (3.35)$$

If there are no external forces applied to any of the unit's internal degrees of freedom then $\mathbf{F}_i = 0$ and the first row of this product can be rewritten as

$$\mathbf{U}_i = -[\mathbf{K}_{ii}]^{-1} \mathbf{K}_{il} \mathbf{U}_l - [\mathbf{K}_{ii}]^{-1} \mathbf{K}_{ir} \mathbf{U}_r \quad (3.36)$$

The forces and moments and the displacements and rotations of the sides of the unit can now be directly related by

$$\begin{Bmatrix} \mathbf{F}_l \\ \mathbf{F}_r \end{Bmatrix} = \begin{bmatrix} \mathbf{K}_{ll} - \mathbf{K}_{li} [\mathbf{K}_{ii}]^{-1} \mathbf{K}_{il} & \mathbf{K}_{lr} - \mathbf{K}_{li} [\mathbf{K}_{ii}]^{-1} \mathbf{K}_{ir} \\ \mathbf{K}_{rl} - \mathbf{K}_{ri} [\mathbf{K}_{ii}]^{-1} \mathbf{K}_{il} & \mathbf{K}_{rr} - \mathbf{K}_{ri} [\mathbf{K}_{ii}]^{-1} \mathbf{K}_{ir} \end{bmatrix} \begin{Bmatrix} \mathbf{U}_l \\ \mathbf{U}_r \end{Bmatrix} \quad (3.37)$$

Forces, moments, displacements and rotations of the q^{th} copy of the repeated unit are denoted by a superscript q , thus for the q^{th} unit we may rewrite equation (3.37) as

$$\begin{Bmatrix} \mathbf{F}_l^q \\ \mathbf{F}_r^q \end{Bmatrix} = \begin{bmatrix} \mathcal{K}_{ll} & \mathcal{K}_{lr} \\ \mathcal{K}_{rl} & \mathcal{K}_{rr} \end{bmatrix} \begin{Bmatrix} \mathbf{U}_l^q \\ \mathbf{U}_r^q \end{Bmatrix} \quad (3.38)$$

where $\mathcal{K}_{ll} = \mathbf{K}_{ll} - \mathbf{K}_{li} [\mathbf{K}_{ii}]^{-1} \mathbf{K}_{il}$ etc.

The displacements and forces at the edges of adjacent units must satisfy compatibility and equilibrium conditions. Thus, if no external forces are applied to the joined degrees of freedom, then

$$\mathbf{U}_r^q = \mathbf{U}_l^{q+1}, \quad \mathbf{F}_r^q + \mathbf{F}_l^{q+1} = \mathbf{0} \quad (3.39)$$

Hence equation (3.38) becomes

$$\begin{Bmatrix} \mathbf{F}_l^q \\ -\mathbf{F}_l^{q+1} \end{Bmatrix} = \begin{bmatrix} \mathcal{K}_{ll} & \mathcal{K}_{lr} \\ \mathcal{K}_{rl} & \mathcal{K}_{rr} \end{bmatrix} \begin{Bmatrix} \mathbf{U}_l^q \\ \mathbf{U}_l^{q+1} \end{Bmatrix} \quad (3.40)$$

These equations can be rearranged as follows

$$\begin{Bmatrix} \mathbf{F}_l^{q+1} \\ \mathbf{U}_l^{q+1} \end{Bmatrix} = \begin{bmatrix} -\mathcal{K}_{rr} [\mathcal{K}_{lr}]^{-1} & \mathcal{K}_{rr} [\mathcal{K}_{lr}]^{-1} \mathcal{K}_{ll} - \mathcal{K}_{rl} \\ [\mathcal{K}_{lr}]^{-1} & -[\mathcal{K}_{lr}]^{-1} \mathcal{K}_{ll} \end{bmatrix} \begin{Bmatrix} \mathbf{F}_l^q \\ \mathbf{U}_l^q \end{Bmatrix} \quad (3.41)$$

Now the displacements and forces at the left side of unit q are related to the displacements and forces at the left side of unit $q + 1$.

By consideration of waves propagating through the assembled structure, it is assumed that the displacements on the left side of the repeating unit are similar to those on the right with only a uniform change in amplitude and phase [9]. The same assumption is made for the forces on both sides of the unit. For a certain wave mode, this can be written out as

$$\begin{Bmatrix} \mathbf{F}_l^{q+1} \\ \mathbf{U}_l^{q+1} \end{Bmatrix} = \lambda \begin{Bmatrix} \mathbf{F}_l^q \\ \mathbf{U}_l^q \end{Bmatrix} \quad (3.42)$$

Consideration of equations (3.41) and (3.42) shows that the propagation of vibration through the structure can be found by solving a standard eigenvalue problem [4]:

$$\begin{bmatrix} -\mathcal{K}_{rr} [\mathcal{K}_{lr}]^{-1} & \mathcal{K}_{rr} [\mathcal{K}_{lr}]^{-1} \mathcal{K}_{ll} - \mathcal{K}_{rl} \\ [\mathcal{K}_{lr}]^{-1} & -[\mathcal{K}_{lr}]^{-1} \mathcal{K}_{ll} \end{bmatrix} \begin{Bmatrix} \mathbf{F}_i \\ \mathbf{U}_i \end{Bmatrix} = \lambda_i \begin{Bmatrix} \mathbf{F}_i \\ \mathbf{U}_i \end{Bmatrix} \quad (3.43)$$

A vector of displacements \mathbf{U}_i at the left hand side of one unit will generate a vector of displacements $\lambda_i \mathbf{U}_i$ at the left hand side of the next unit. Therefore each element of the vector \mathbf{U}_i has undergone the same scaling of amplitude and change of phase.

The matrix in equation (3.41) is of order $2p \times 2p$, where p is the number of degrees of freedom connected between adjacent units. Thus this matrix has $2p$ eigenvectors and eigenvalues. Half of these eigenvectors correspond to wave patterns propagating to the left and the other half to wave patterns propagating to the right. Those eigenvectors whose eigenvalues have magnitudes less than 1 correspond to wave patterns propagating to the right, as the vibration amplitude must be bounded at infinity. Similarly, eigenvalues with magnitudes greater than one correspond to wave patterns travelling to the left.

For the semi-infinite structure in Figure 3.7 the wave patterns that are excited must decay as they propagate to the right as the response tends to zero at infinity. Thus the vector of the p displacements at the left-hand end of this structure, \mathbf{U}_l^1 , must be a linear combination of the p eigenvectors which correspond to wave patterns propagating to the right, and so may be written as

$$\mathbf{U}_l^1 = \begin{bmatrix} \mathbf{U}_1 & \mathbf{U}_2 & \dots & \mathbf{U}_{p-1} & \mathbf{U}_p \end{bmatrix} \mathbf{C} = \underline{\mathbf{U}} \mathbf{C} \quad (3.44)$$

where \mathbf{C} is a vector whose i^{th} element determines the amplitude and phase of the i^{th} eigenvector in the motion. Similarly, the forces \mathbf{F}_l^1 acting on this end of the structure are given by

$$\mathbf{F}_l^1 = \begin{bmatrix} \mathbf{F}_1 & \mathbf{F}_2 & \dots & \mathbf{F}_{p-1} & \mathbf{F}_p \end{bmatrix} \mathbf{C} = \underline{\mathbf{F}} \mathbf{C} \quad (3.45)$$

By eliminating \mathbf{C} from these two equations, the stiffness matrix of the end of the semi-infinite structure extending to the right is obtained:

$$\mathbf{F}_l^1 = \underline{\mathbf{F}} [\underline{\mathbf{U}}]^{-1} \mathbf{U}_l^1 = \mathbf{K}_\infty^r \mathbf{U}_l^1 \quad (3.46)$$

3.3.2 Construction of an infinite model

To construct an infinite building model, the semi-infinite structure considered in the previous section has to be joined with a central unit and a semi-infinite structure extending to the left as shown in Figure 3.6. The central unit is the same as the repeated unit used in previous section. To find the stiffness matrix of the semi-infinite structure extending to the left, a similar construction technique to that described above may be used. However, it can also be constructed by using the wave patterns travelling to the left which have already been found during the analysis. Combining the p eigenvectors which correspond to wave patterns propagating to the left in a matrix \underline{U} as in equation (3.44) and the corresponding forces in a matrix \underline{F} as in equation (3.45), the stiffness matrix of the semi-infinite structure extending to the left is found as in equation (3.46):

$$\mathbf{K}_{\infty}^l = \underline{F}[\underline{U}]^{-1} \quad (3.47)$$

Connecting these repeated structures to a central structure involves including their stiffness matrices in the assembly of the central structure's stiffness matrix \mathbf{K}_G . This procedure is analogous to adding an extra beam to the structure as described in section 3.2 although in this case the size of the stiffness matrix to be included may be somewhat larger. This addition is performed for each of the entries in the central structure's stiffness matrix, and for both of the semi-infinite structures.

3.4 Comparison of finite and infinite building models

In this section the difference will be investigated between finite and infinite models. In section 3.4.2 two buildings without a pile foundation will be compared. In this case the column bases are constrained. In section 3.4.3 two buildings with a pile foundation will be compared. This allows us to investigate the difference between finite and infinite models first and next the influence of adding a pile foundation.

At the same time the model will be validated by reproducing some figures that Cryer showed in his work [4]. The finite model consist of 9 columns and 5 floors (9×5) and the infinite model consists of 5 floors. The same dimensions and material parameters are used and are given below.

In Table 3.1 the material parameters and geometry of the building are given. In Table 3.2 the properties for the pile foundation and soil are given.

3.4.1 Damping

Before continuing, an important difference between the approach used here and that of Cryer has to be noted. In his derivation of the stiffness matrix of a beam, Cryer used the equation of motion of an elastic bar and an Euler beam with Rayleigh damping [4]. In this dissertation the undamped equations of motion are used. Material damping is modelled in the frequency domain by replacing the standard elastic constants with suitable complex values [2].

3.4. Comparison of finite and infinite building models

Material parameters	Value
Density	2400 kg/m ³
Young's modulus	45 × 10 ⁹ Pa
Rayleigh damping constant α	2.0 s ⁻¹
Rayleigh damping constant β	2 × 10 ⁻⁵ s
Column geometry	Value
Column spacing	4 m
Area	0.08 m ²
Second moment of inertia	2.67 × 10 ⁻⁴ m ⁴
Cross section	rectangular
Floor geometry	Value
Floor spacing	3 m
Area	0.6 m ²
Second moment of inertia	0.002 m ⁴
Cross-section	rectangular

TABLE 3.1: Building parameters

Pile properties	Value
Density	2400 kg/m ³
Young's modulus	45 × 10 ⁹ Pa
Rayleigh damping constant α	2.0 s ⁻¹
Rayleigh damping constant β	2 × 10 ⁻⁵ s
Pile geometry	Value
Pile radius	0.2 m
Pile length	20 m
Cross section	circular
Soil properties	Value
Density	2000 kg/m ³
Shear modulus	80 × 10 ⁶ Pa
Poisson's ratio	0.4

TABLE 3.2: Foundation parameters

The following relationship can be found between the constants α and β used by Cryer [4] and the damping loss factor η :

$$\eta(\omega) = \frac{\alpha}{\omega} + \beta\omega \quad (3.48)$$

In the next two sections the minimum of this function will be used:

$$\eta = 2\sqrt{\alpha\beta} = 2\sqrt{2.0 \times 2 \times 10^{-5}} = 0.013 \quad (3.49)$$

3.4.2 Comparison between finite and infinite building models without a pile foundation

The building models without a pile foundation are constructed in a similar way as the models described in section 3.2 and 3.3. Instead of connecting piles to the bases of the column, the column bases are constrained from translating or rotating except from the centre column. The excitation is a vertical unit displacement at the base of the central column.

Figure 3.8 shows the transmissibility of the vertical displacement of the node of the upper floor at the centre of the building in function of frequency. The transmissibility is the response of the position where the displacements are wanted divided by the response of the position where the load is applied. The results exhibit great similarity in certain frequency ranges, but at other frequencies the finite model displays a series of additional resonances and anti-resonances. The resonances are due to waves reflecting at the free sides of the finite model.

Some of these peaks will be further investigated by plotting the displacement of the entire building at the particular frequency of a peak. To do this the response of the elements at points other than their nodes is required. The vibration amplitudes of the nodes, and thus the ends of the elements, provide sufficient information to calculate the response at any point of each element. At a particular frequency the parameters \mathbf{c} governing the motion of an element may be derived from the displacements of its ends using equation (3.11). The response in the frequency domain at a point along the element is then readily obtained from equations (3.4) and (3.8). The response in

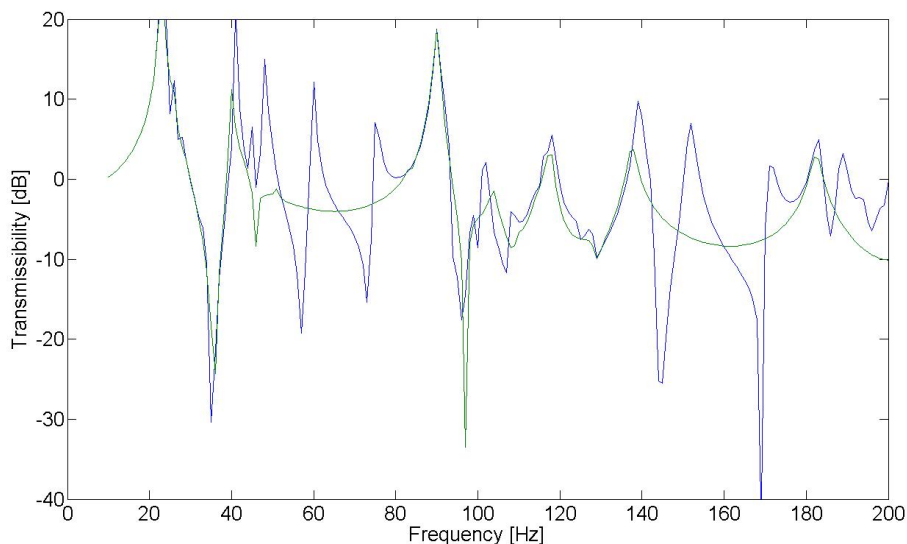


FIGURE 3.8: Vertical response of the top of the forced column of a finite (blue line) and infinite (green line) building model without a pile foundation.

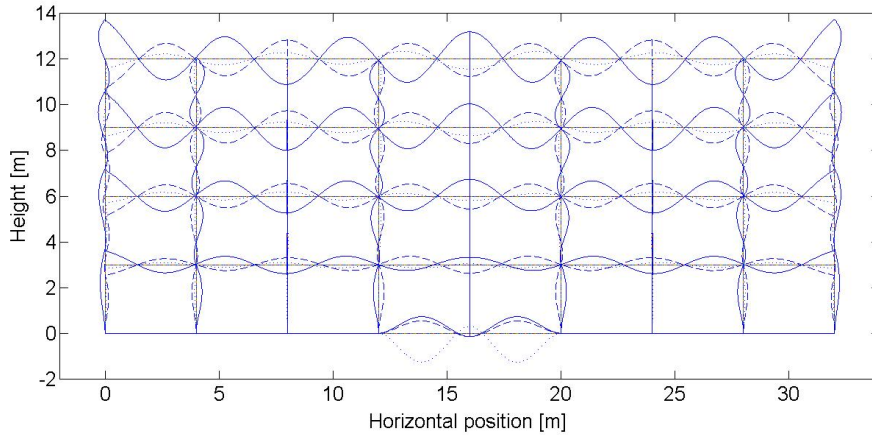


FIGURE 3.9: Real part of the displacement of the finite building without a pile foundation for $\omega = 2\pi 60$ rad/s at $t = 2\pi/(3\omega)$ (solid line), $t = \pi/(3\omega)$ (dashed line), $t = 2\pi/\omega$ (dotted line).

the time domain for a certain frequency can be calculated with

$$\begin{aligned} u(x, t) &= \Re(U(x, \omega)e^{i\omega t}) \\ v(x, t) &= \Re(V(x, \omega)e^{i\omega t}) \end{aligned} \quad (3.50)$$

This is done for every element in the structure to give the deformed shape for a particular frequency and phase of the input.

Consider the peak at 60 Hz visible in Figure 3.8 for the finite building. Figure 3.9 shows the displacement of the finite model and Figure 3.10 shows the displacement of the infinite model at 60 Hz. It is clearly visible that for the finite model the waves reflect at the free ends while for the infinite model the wave amplitude becomes small further away from the centre.

The peaks in Figure 3.8 coincide with eigenfrequencies and eigenmodes of the building. To find these eigenfrequencies and eigenmodes, a finite element model is made for the finite building using the Stabil package in Matlab. In Figure 3.11 the eigenmode at 22.38 Hz is shown. This motion is present in the finite and infinite building model. In Figure 3.12 the eigenmode at 58.65 Hz is shown. This motion is only present in the finite model and is consistent with the motion depicted in Figure 3.9. Due to the infinite extent, certain eigenmodes won't be present in the infinite model.

3.4. Comparison of finite and infinite building models

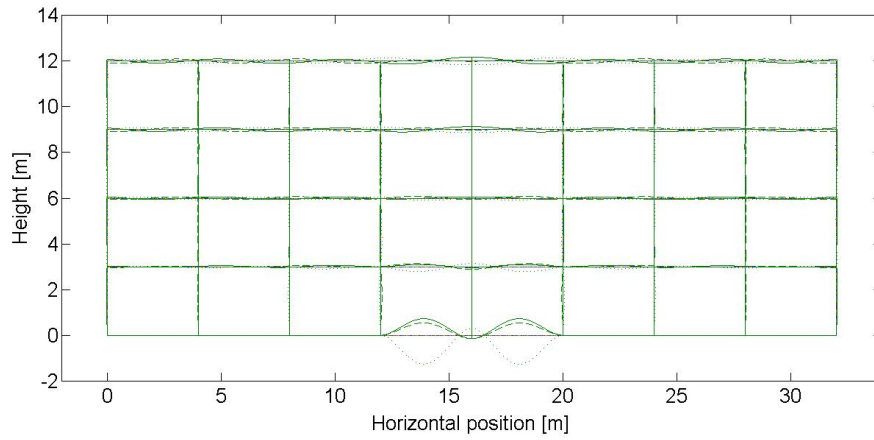
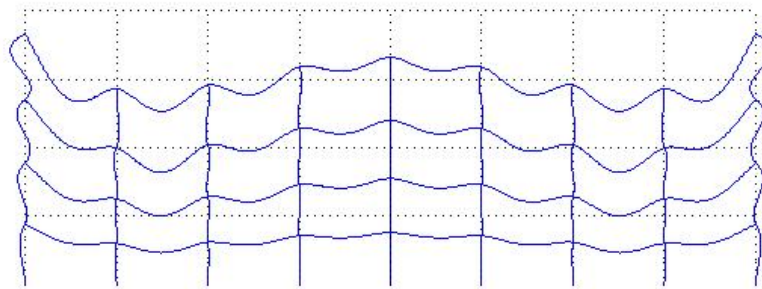
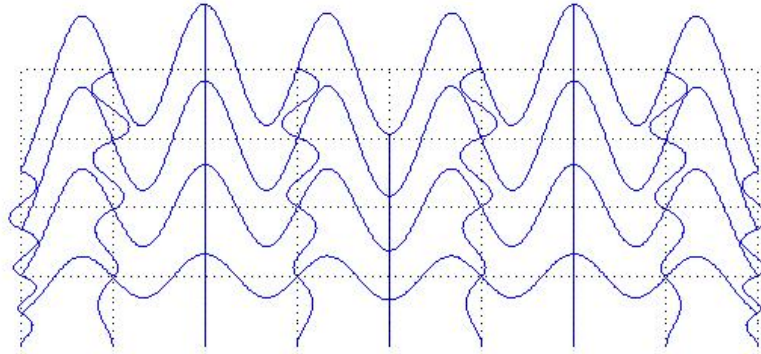


FIGURE 3.10: Real part of the displacement of the infinite building without a pile foundation for $\omega = 2\pi 60$ rad/s at $t = 2\pi/(3\omega)$ (solid line), $t = \pi/(3\omega)$ (dashed line), $t = 2\pi/\omega$ (dotted line).



Maximal displacement: 0.0039163

FIGURE 3.11: Eigenmode at 22.38 Hz found with the finite element model.



Maximal displacement: 0.00627099

FIGURE 3.12: Eigenmode at 58.65 Hz found with the finite element method.

3.4.3 Comparison between finite and infinite building models with a pile foundation

By adding a pile foundation to the building model, the apparent damping in the structure increases. This has a significant effect on the differences noted between the response of the finite and infinite building models discussed in section 3.4.2. These differences were attributed to standing waves due to reflections at the sides of the finite model. The damping provided by the piled foundations increases the attenuation of the outgoing and reflected waves as they travel through the building so now they do not interfere as effectively to produce resonances. Figure 3.13 shows the displacement response for a finite and an infinite building model with a pile foundation. Again a vertical unit displacement at the base of the central column is used as the input to both models and the vertical response at the top of that column is shown.

Figure 3.14 and Figure 3.15 show the deformed shapes of the building for an input frequency of 60 Hz for the finite model and infinite model, respectively. These plots show much greater similarity than was seen in the absence of the pile foundation. However, in the 40-70 Hz and 140-170 Hz regions there are still peaks in the response of the finite model that are not present in the infinite model as can be seen in Figure 3.13. At these frequencies, resonances are still present in the finite building model. However, the differences in the responses of the two models over the entire frequency range considered here are much reduced.

The peaks observed in Figure 3.13 still coincide with eigenmodes of the building. However, due to the addition of the piles, these peaks are lower and slightly shifted

3.4. Comparison of finite and infinite building models

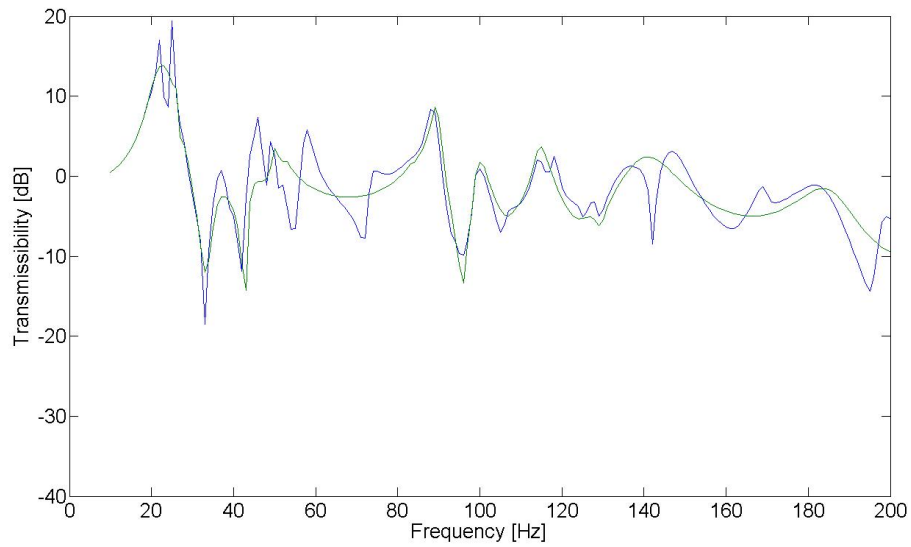


FIGURE 3.13: Vertical response of the top of the forced column of a finite (blue line) and infinite (green line) building model with a pile foundation.

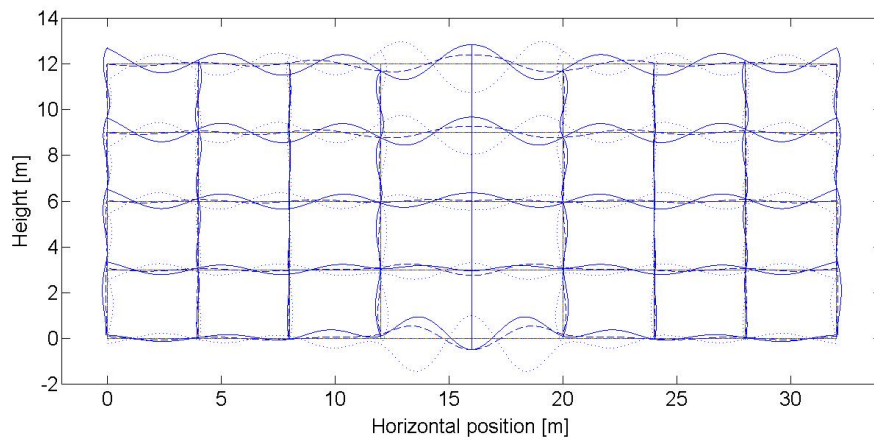


FIGURE 3.14: Real part of the displacement of the finite building with a pile foundation for $\omega = 2\pi 60$ rad/s at $t = 2\pi/(3\omega)$ (solid line), $t = \pi/(3\omega)$ (dashed line), $t = 2\pi/\omega$ (dotted line).

to the left. This is true for both the finite and infinite model.

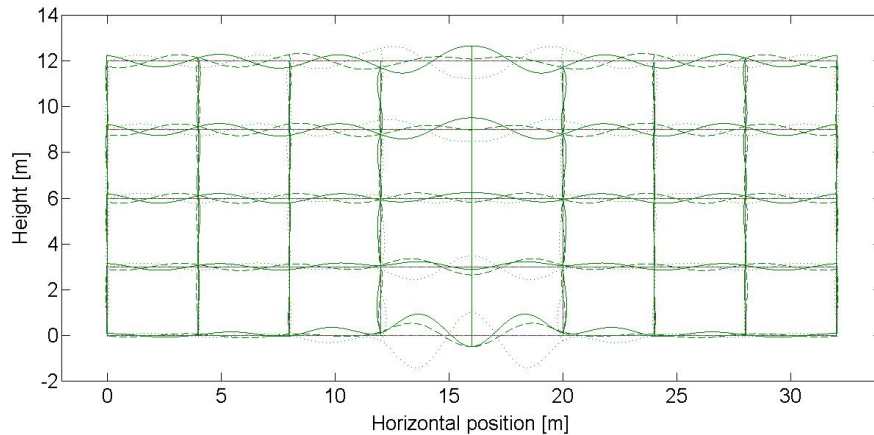


FIGURE 3.15: Real part of the displacement of the infinite building with a pile foundation for $\omega = 2\pi 60$ rad/s at $t = 2\pi/(3\omega)$ (solid line), $t = \pi/(3\omega)$ (dashed line), $t = 2\pi/\omega$ (dotted line).

3.5 Conclusion

The building modelled in this chapter is represented by a two-dimensional portal frame. This portal frame is modelled with the dynamic stiffness method. With this method the building is divided in substructures for which the analytical solution is known. The floors, columns and piles are the substructures of the building. The floors and columns are modelled as beams and Novak's model is used to model the piles. The different substructures are then joined in a similar way as the elements of a finite element model. This results in a model that requires little computation time.

To further reduce the computation time, the building is assumed to be of infinite extent. The infinite building is modelled using periodic structure theory. It consists of a central unit and a semi-infinite structure extending to the left and one extending to the right.

By comparing finite and infinite models it can be concluded that the infinite model accurately represents the dynamic behaviour of a multistory building on a piled foundation. This conclusion confirms that of Cryer [4] who both modelled an infinite building and carried out site measurements for a multistory building, before and after construction. The results showed a good agreement between the response of the infinite model and the measurements.

Chapter 4

Coupling the PiP model to the building model

In this chapter the displacement response of a building due to underground railway vibrations will be calculated. The PiP model will generate the displacements that will serve as inputs for the building model described in Chapter 3. An uncoupled approach will be used. This means that there is no interaction between the underground railway and the building and it is assumed that the presence of the building has no influence on the vibrations generated by the underground railway. A coupled model is more accurate when the distance between the tunnel and the building is limited, but these models require more computation power. Therefore an uncoupled model is used.

In section 4.1 the method of joining subsystems is explained. “The composite system produced using this method represents an uncoupled source-receiver model” [13]. This method will then be used in section 4.2 to join the PiP model and the building. The displacement response of the building is first calculated for an input at one pile. Since the vibration input of the underground railway acts on all the piles of the building, the calculations described in section 4.2 have to be repeated for all the piles. The total displacement response of the building can be found by superposition due the linear nature of the methods used and is presented in section 4.3.

The calculations are performed in the space-frequency domain. Only the vertical displacement component generated by the PiP model will be used. This is because the Novak model used to model the piles only gives a good representation of the axial behaviour, but not of the lateral behaviour due to the plane strain assumptions [13].

4.1 Method of joining subsystems

Consider two subsystems A and B , characterised by the matrix equations

$$\mathbf{F}^A = \mathbf{K}^A \mathbf{U}^A \quad \text{and} \quad \mathbf{F}^B = \mathbf{K}^B \mathbf{U}^B \quad (4.1)$$

where \mathbf{U}^A and \mathbf{U}^B are vectors with the displacements of the nodes of system A and B respectively, \mathbf{F}^A and \mathbf{F}^B are vectors with the forces acting on those nodes and

K^A and K^B are the dynamic stiffness matrices of the two systems which relate the forces to the displacements.

Each subsystem is build up out of nodes which have a certain amount of degrees of freedom (for the two dimensional building model described in Chapter 3 each node has three degrees of freedom). There are three possible types of degree of freedom: those constrained not to move, those that will be attached together when the systems are joined and those that are internal to each of the systems. The equations in (4.1) can be rewritten as

$$\begin{Bmatrix} \mathbf{F}_i^A \\ \mathbf{F}_j^A \\ \mathbf{F}_c^A \end{Bmatrix} = \begin{bmatrix} K_{ii}^A & K_{ij}^A & K_{ic}^A \\ K_{ji}^A & K_{jj}^A & K_{jc}^A \\ K_{ci}^A & K_{cj}^A & K_{cc}^A \end{bmatrix} \begin{Bmatrix} \mathbf{U}_i^A \\ \mathbf{U}_j^A \\ \mathbf{U}_c^A \end{Bmatrix} \quad \text{and} \quad \begin{Bmatrix} \mathbf{F}_i^B \\ \mathbf{F}_j^B \\ \mathbf{F}_c^B \end{Bmatrix} = \begin{bmatrix} K_{ii}^B & K_{ij}^B & K_{ic}^B \\ K_{ji}^B & K_{jj}^B & K_{jc}^B \\ K_{ci}^B & K_{cj}^B & K_{cc}^B \end{bmatrix} \begin{Bmatrix} \mathbf{U}_i^B \\ \mathbf{U}_j^B \\ \mathbf{U}_c^B \end{Bmatrix} \quad (4.2)$$

where subscript i denotes an internal degree of freedom, subscript j a joined degree of freedom and c a constrained degree of freedom. The displacements \mathbf{U}_c of the constrained degrees of freedom are zero and the forces \mathbf{F}_c acting on these nodes can be calculated once \mathbf{U}_i and \mathbf{U}_j are known. Equations (4.2) simplify to

$$\begin{Bmatrix} \mathbf{F}_i^A \\ \mathbf{F}_j^A \end{Bmatrix} = \begin{bmatrix} K_{ii}^A & K_{ij}^A \\ K_{ji}^A & K_{jj}^A \end{bmatrix} \begin{Bmatrix} \mathbf{U}_i^A \\ \mathbf{U}_j^A \end{Bmatrix} \quad \text{and} \quad \begin{Bmatrix} \mathbf{F}_i^B \\ \mathbf{F}_j^B \end{Bmatrix} = \begin{bmatrix} K_{ii}^B & K_{ij}^B \\ K_{ji}^B & K_{jj}^B \end{bmatrix} \begin{Bmatrix} \mathbf{U}_i^B \\ \mathbf{U}_j^B \end{Bmatrix} \quad (4.3)$$

In the derivations that follow, the inverse of the dynamic stiffness matrices will be used. These are called compliance matrices [4]. Equation (4.3) can be rewritten as

$$\begin{Bmatrix} \mathbf{U}_i^A \\ \mathbf{U}_j^A \end{Bmatrix} = \begin{bmatrix} K_{ii}^A & K_{ij}^A \\ K_{ji}^A & K_{jj}^A \end{bmatrix}^{-1} \begin{Bmatrix} \mathbf{F}_i^A \\ \mathbf{F}_j^A \end{Bmatrix} = \begin{bmatrix} H_{ii}^A & H_{ij}^A \\ H_{ji}^A & H_{jj}^A \end{bmatrix} \begin{Bmatrix} \mathbf{F}_i^A \\ \mathbf{F}_j^A \end{Bmatrix} \quad (4.4)$$

$$\begin{Bmatrix} \mathbf{U}_i^B \\ \mathbf{U}_j^B \end{Bmatrix} = \begin{bmatrix} K_{ii}^B & K_{ij}^B \\ K_{ji}^B & K_{jj}^B \end{bmatrix}^{-1} \begin{Bmatrix} \mathbf{F}_i^B \\ \mathbf{F}_j^B \end{Bmatrix} = \begin{bmatrix} H_{ii}^B & H_{ij}^B \\ H_{ji}^B & H_{jj}^B \end{bmatrix} \begin{Bmatrix} \mathbf{F}_i^B \\ \mathbf{F}_j^B \end{Bmatrix}$$

When the systems are joined the displacements of connected degrees of freedom must be the same in each system and the sum of the forces acting on these degrees of freedom must equal any externally applied force, thus

$$\begin{aligned} \mathbf{U}_j &= \mathbf{U}_j^A = \mathbf{U}_j^B \\ \mathbf{F}_j &= \mathbf{F}_j^A + \mathbf{F}_j^B \end{aligned} \quad (4.5)$$

Substituting these conditions in equation (4.4) gives the following set of equations

$$\begin{cases} \mathbf{U}_i^A = & H_{ii}^A \mathbf{F}_i^A + H_{ij}^A \mathbf{F}_j^A \\ \mathbf{U}_j^A = \mathbf{U}_j = & H_{ji}^A \mathbf{F}_i^A + H_{jj}^A \mathbf{F}_j^A \\ \mathbf{U}_i^B = & H_{ii}^B \mathbf{F}_i^B + H_{ij}^B (\mathbf{F}_j - \mathbf{F}_j^A) \\ \mathbf{U}_j^B = \mathbf{U}_j = & H_{ji}^B \mathbf{F}_i^B + H_{jj}^B (\mathbf{F}_j - \mathbf{F}_j^A) \end{cases} \quad (4.6)$$

An expression for \mathbf{F}_j^A can be derived from the second and fourth expression in (4.6):

$$\mathbf{F}_j^A = \left[H_{jj}^A + H_{jj}^B \right]^{-1} \left[H_{ji}^B \mathbf{F}_i^B + H_{jj}^B \mathbf{F}_j - H_{ji}^A \mathbf{F}_i^A \right] \quad (4.7)$$

The displacement in the two systems can be found by substituting this result back into the set of equations (4.6). Particularly the displacements in system B will be of interest in the next section.

4.2 Joining the PiP model and the building model

In this case system A is the tunnel with the surrounding soil and system B is the infinite building with a pile foundation as shown in Figure 4.1. The calculations will be done for an input at the centre pile of the building.

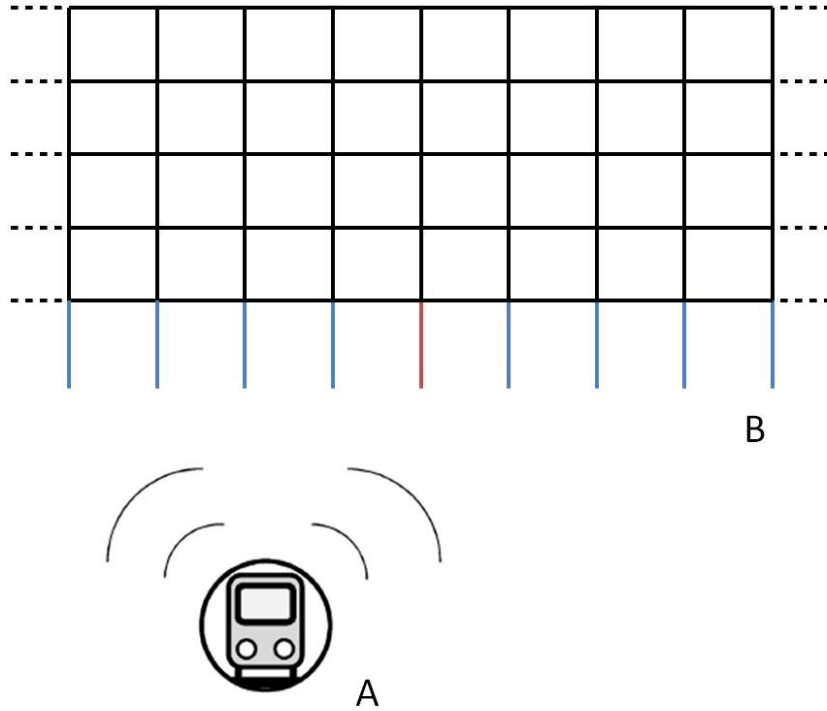


FIGURE 4.1: The two separate subsystems that are joined together to obtain a building-railway model.

The centre pile is discretised into N equally spaced segments along the pile length, as shown in Figure 4.2. At the top and bottom faces of each segment is a node where forces are applied to the pile and the displacements are calculated. This means that there are $N + 1$ nodes. The incident wavefield is calculated at the position of these nodes. The spacing between the nodes has to be small enough to capture the wave behaviour of the incident wavefield [13].

The $N + 1$ nodes of the pile are joined to the PiP model, these are the joined degrees of freedom. Assume that there are no external forces acting on the joined

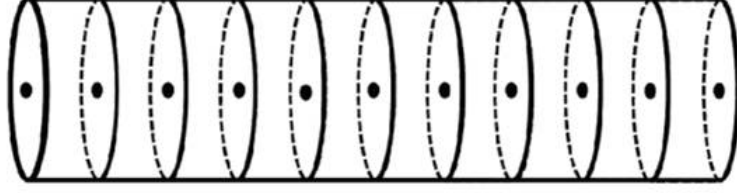


FIGURE 4.2: Discretisation of the pile into N equally spaced segments ($N = 10$ in this case), with $N + 1$ nodes for application of forces and displacements [13]

nodes or the internal nodes of the building. Equation (4.7) can be simplified:

$$\mathbf{F}_j^A = - \left[\mathbf{H}_{jj}^A + \mathbf{H}_{jj}^B \right]^{-1} \left[\mathbf{H}_{ji}^A \mathbf{F}_i^A \right] \quad (4.8)$$

Substituting this result into the set of equations (4.6) yields an expression for the displacements of the centre pile nodes and the building:

$$\begin{aligned} \mathbf{U}_j^B &= \mathbf{H}_{jj}^B \left[\mathbf{H}_{jj}^A + \mathbf{H}_{jj}^B \right]^{-1} \left[\mathbf{H}_{ji}^A \mathbf{F}_i^A \right] \\ \mathbf{U}_i^B &= \mathbf{H}_{ij}^B \left[\mathbf{H}_{jj}^A + \mathbf{H}_{jj}^B \right]^{-1} \left[\mathbf{H}_{ji}^A \mathbf{F}_i^A \right] \end{aligned} \quad (4.9)$$

The vector \mathbf{F}_i^A are the forces acting on the track. The elements of the matrix \mathbf{H}_{ji}^A are the FRFs of the PiP model which give the displacements in the soil at the position of the joined nodes to an unit input load on the track. Thus the product $\mathbf{H}_{ji}^A \mathbf{F}_i^A$ is simply the incident wavefield at positions of the joined nodes calculated with the PiP model. Equation (4.9) can be rewritten as

$$\begin{aligned} \mathbf{U}_j^B &= \mathbf{H}_{jj}^B \left[\mathbf{H}_{jj}^A + \mathbf{H}_{jj}^B \right]^{-1} \mathbf{U}^{\text{incident}} \\ \mathbf{U}_i^B &= \mathbf{H}_{ij}^B \left[\mathbf{H}_{jj}^A + \mathbf{H}_{jj}^B \right]^{-1} \mathbf{U}^{\text{incident}} \end{aligned} \quad (4.10)$$

where $\mathbf{U}^{\text{incident}}$ is the incident wavefield.

The FRF matrix \mathbf{H}_{jj}^A relates the displacement of the soil to the forces acting on the soil. In the Novak model used here, there is no interaction between the soil layers. Therefore, there are no cross-coupling terms and \mathbf{H}_{jj}^A is a diagonal matrix. For axial vibration the diagonal terms are $\frac{1}{GS_x L/N}$ and for lateral vibration the diagonal terms are $\frac{1}{GS_y L/N}$ where L is the pile length and G the shear modulus of the soil and S_x and S_y are given by equation (3.17) and (3.23) [13].

The matrices \mathbf{H}_{jj}^B and \mathbf{H}_{ij}^B can be derived from the inverse of the global dynamic stiffness matrix of the building. Note that the centre pile is divided into N segments. The stiffness matrix for one segment is obtained by assuming that segment as a pile of length L/N .

The vectors \mathbf{U}_j and \mathbf{U}_i contain the displacements of the central unit of the infinite building. Also the displacement response elsewhere in the building is wanted.

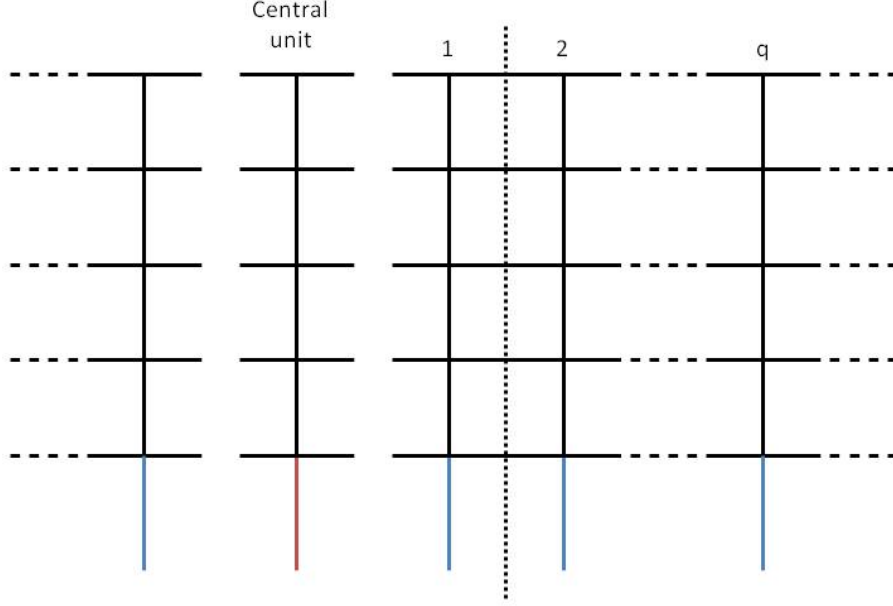


FIGURE 4.3: Central unit and repeating units for an infinite building with 5 floors.

The displacement at the right hand side of the central unit $\mathbf{V}_r^{\text{central unit}}$ is equal to the displacement on the left hand side of the first repeating unit \mathbf{U}_l^1 . As an example, the central unit and the repeating units of an infinite building with five floors are shown in Figure 4.3.

In section 3.3.1 the displacements on the left hand side of the first unit are written as a linear combination of the eigenvectors of the repeating unit (equation (3.44)):

$$\mathbf{U}_l^1 = \begin{bmatrix} \underline{\mathbf{U}}_1 & \underline{\mathbf{U}}_2 & \dots & \underline{\mathbf{U}}_{p-1} & \underline{\mathbf{U}}_p \end{bmatrix} \mathbf{C} = \underline{\mathbf{U}} \mathbf{C} \quad (4.11)$$

With the displacements and eigenvectors known, the coefficients \mathbf{C} can be determined from

$$\mathbf{C} = [\underline{\mathbf{U}}]^{-1} \mathbf{U}_l^1 \quad (4.12)$$

Remembering that a vector of displacements $\underline{\mathbf{U}}_i$ at the left hand side of one unit will generate a vector of displacements $\lambda_i \underline{\mathbf{U}}_i$ at the left hand side of the next unit, the displacements of unit q can be determined from

$$\mathbf{U}_l^q = \begin{bmatrix} \lambda_1^{q-1} \underline{\mathbf{U}}_1 & \lambda_2^{q-1} \underline{\mathbf{U}}_2 & \dots & \lambda_{p-1}^{q-1} \underline{\mathbf{U}}_{p-1} & \lambda_p^{q-1} \underline{\mathbf{U}}_p \end{bmatrix} \mathbf{C} \quad (4.13)$$

The displacements of the internal nodes of the repeating unit follow from equation (3.36):

$$\mathbf{U}_i^q = -[\mathbf{K}_{ii}]^{-1} \mathbf{K}_{il} \mathbf{U}_l^q - [\mathbf{K}_{ii}]^{-1} \mathbf{K}_{ir} \mathbf{U}_r^q \quad (4.14)$$

where the displacements \mathbf{U}_r^q at the right hand side of unit q are equal to the displacements \mathbf{U}_l^{q+1} at the left hand side of the next unit.

In a similar way the displacements of the semi-infinite structure extending to the left can be found by using the p eigenvectors and eigenvalues of waves propagating to the left or by using the symmetry of the problem.

4.3 Response of the entire building

In section 4.1 the displacement of the building for an input at one pile was calculated. The building, however, has a larger number of piles, so multiple inputs have to be used. Due to the linear nature of the methods superposition can be used. The displacement response of the building is calculated for each input separately and then added to the total response after it is shifted over the correct distance.

Real buildings are of finite extent and the vibration input only acts on the piles of this finite building. The building, however, is modelled as an infinite building, but with inputs only acting on the piles of the real building. For example, consider a real building with 5 floors and 7 columns as depicted in Figure 4.4. For an input at the first pile (pile at the left hand side) the displacement response is calculated for the central unit of the infinite model in Figure 4.3 and six repeating units to the right of that central unit. These displacements can be written in a 5×7 matrix where the rows reflect the rows of the finite building and the columns the columns of the building. Next the displacement response for an input at the second pile is calculated. Now the displacements are calculated for one repeating unit to the left of the central unit, the central unit and five repeating units to the right of the central unit and gathered in a matrix accordingly. This procedure is repeated for an input at the other pile locations. The matrices must be added to obtain the total displacement response of the building.

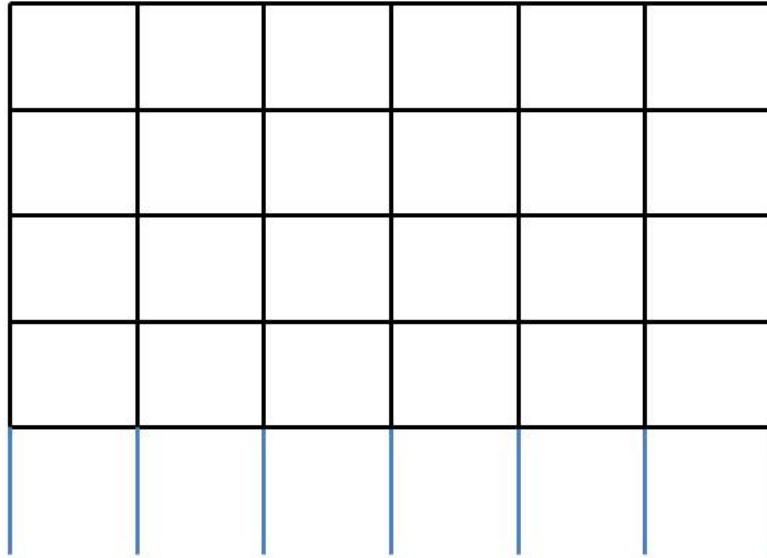
For a building parallel to the tunnel, the displacements at the pile locations are all the same due to the infinite extent of the tunnel model. This means that the building response has to be calculated only once and therefore the calculation time is limited. For a building at a different angle to the tunnel, the displacements at the different piles differ and have to be calculated separately. Therefore the computation time will be longer than for a building parallel to the tunnel.

4.4 Graphical user interface

4.4.1 PiP model

Hussein programmed the GUI of the PiP model. Version 3 will be used here to include a building. It contains the PiP model in its most simple form. It consists of a tunnel in a full space and a floating slab track. Bedrock can be accounted for by using the mirror image method. However, there is no option to include a free surface or soil layers.

The interface is shown in Figure 4.5. In the upper half the configuration of the floating slab track and the tunnel is shown. In the bottom half the results for a particular case are shown. It is possible to plot the power spectral density of the

FIGURE 4.4: 5×7 building with pile foundations

vertical displacement component or the insertion gain of the different cases. In between different runs, the parameters of the different elements of the model can be adapted. Also the position where the PSD is calculated can be changed. The default parameters of the PiP model are given in Table 4.1.

In version 4 a free surface was added to the interface. Hussein and Rikse used the fictitious force method and the ElastoDynamic Toolbox to do this [19]. However, this version takes longer to run and therefore version 3 will be used to keep the computation time limited.

4.4.2 PiP model and building model

The methods described in this chapter will be integrated in the GUI of the PiP model. To keep the computation time low, only a building parallel to the tunnel will be included and the infinite building model will be used.

The updated interface is shown in Figure 4.6. The only differences that can be noted with Figure 4.5 are the tick box *Add building* on the right hand side of the interface and the menu option *Building* in the menu bar. A building is located by defining the position of the base of the centre column. The response of this point will be shown in the results section. This enables the user to compare the vibration level before and after a building is added. The default parameters of the building are given in Table 4.2.

Soil parameters	Value
Density	2000 kg/m ³
Young's modulus	0.55×10^9 N/m ²
Poisson's ratio	0.44
Shear loss factor	0.06
Dilatational loss factor	0
Tunnel parameters	Value
Density	2500 kg/m ³
Young's modulus	50×10^9 N/m ²
Poisson's ratio	0.3
Shear loss factor	0
Dilatational loss factor	0
Tunnel radius	3 m
Tunnel thickness	0.25 m
Train parameters	Value
Unsprung axle mass	500 kg
Spacing between axles	20 m
Rail and railpad parameters	Value
Railpad stiffness per rail	0.20×10^9 N/m/m
Railpad loss factor	0.3
Bending stiffness of one rail	0.005×10^9 N.m ²
Bending stiffness loss factor	0.02
Mass of one rail	50 kg/m
Slab and slab bearing parameters	Value
Bending stiffness of slab	1.43×10^9 N.m ²
Bending stiffness loss factor	0.05
Slab mass	3500 kg/m
Natural frequency of slab	40 Hz
Bearing stiffness	0.221×10^9 N/m/m
Bearings loss factor	0.5

TABLE 4.1: Default parameters PiP model

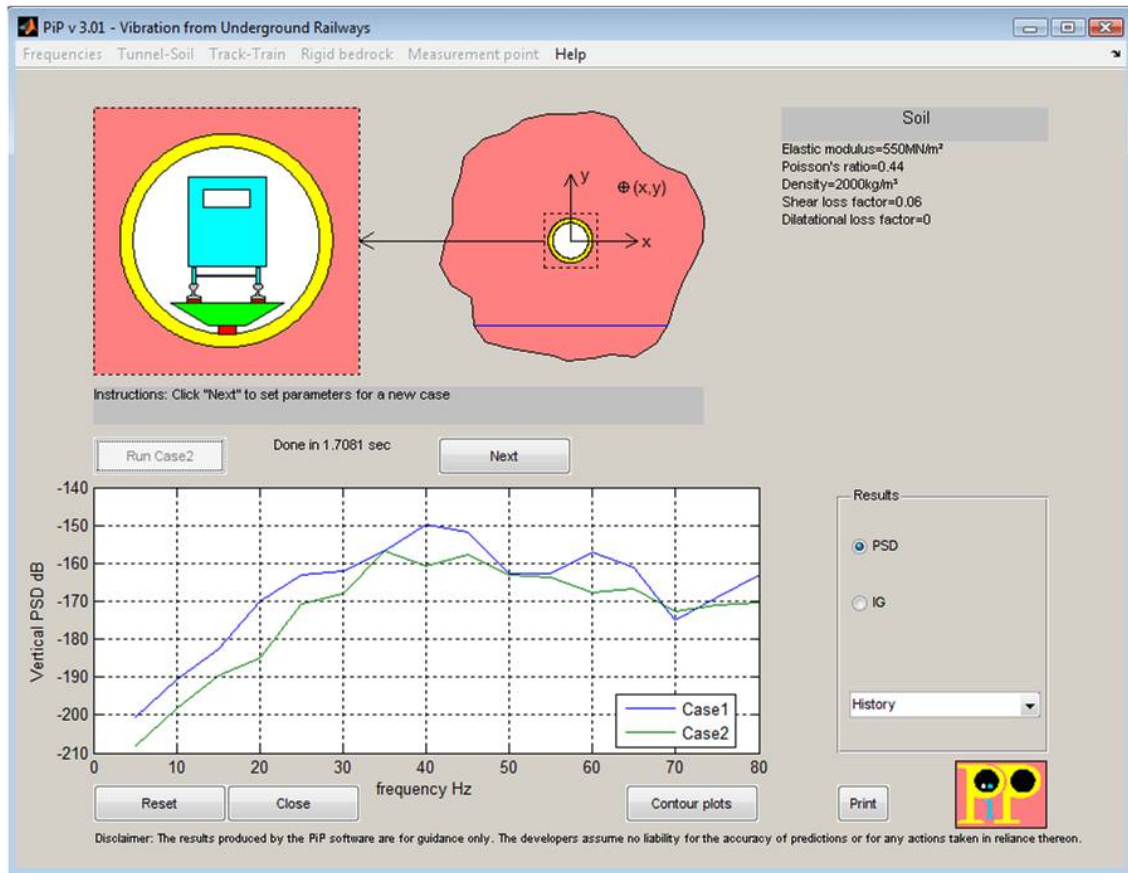


FIGURE 4.5: PiP model version 3.

To illustrate the working principle of the GUI a short case study is presented in section 4.5.

4.5 Case study

In this case study a building will be constructed in the vicinity of an underground railway. First the vibration level before the construction will be calculated. In Case 2 a building will be added and in Case 3 a number of floors will be added to the building of Case 2. In Case 4 the building of Case 2 will be relocated to a different position.

Case 1: Vibration level before construction

The base of the centre column of the building will be located at $x = 0$ m and $y = 20$ m following the convention of the GUI of the PiP model (see Figure 4.5). At this position the vibration level is calculated before a building is added. The default



FIGURE 4.6: PiP model version 3 with the option to include a building.

values for the tunnel (Table 4.2) will be used. The frequency range considered is 2 Hz till 200 Hz with intervals of 2 Hz.

The vertical PSD is shown in Figure 4.7. A peak of the vibration level is observed at 40 Hz and different peaks and troughs can be observed between 60 Hz and 160 Hz. These peaks are due to an interference of compression and shear waves that propagate away from the tunnel. The frequency step depends on the distance between the tunnel and the observation point and the soil parameters [8].

Case 2: 5×7 building at $x = 0$ m and $y = 20$ m

Now a building is added parallel to the tunnel at the location mentioned in Case 1. The default parameters of the building (Table 4.2) are used.

The PSD density is shown in Figure 4.7. A general reduction of the vibration level can be observed. The peak vibration level still occurs at 40 Hz and is about equal to that of Case 1. The peaks and troughs between 60 Hz and 160 Hz are no longer visible. The extra mass added by the building and the damping within this building reduce the vibration observed.

Column parameters	Value
Density	2400 kg/m ³
Young's Modulus	10 × 10 ⁹ N/m ²
Loss factor	0.1
Area	0.5 m ²
Second moment of inertia	0.04 m ²
Column height	3 m
Number of columns	7
Floor parameters	Value
Density	2400 kg/m ³
Young's Modulus	10 × 10 ⁹ N/m ²
Loss factor	0.1
Area	0.5 m ²
Second moment of inertia	0.04 m ²
Floor length	5 m
Number of floors	5
Pile parameters	Value
Density	2667 kg/m ³
Young's Modulus	28 × 10 ⁹ N/m ²
Damping loss factor	0
Pile radius	0.354 m
Pile length	7.5 m

TABLE 4.2: Default building parameters

In Figure 4.8 the vertical PSD at the top of the centre column is shown. Two peaks are clearly visible one at 40 Hz and one at 140 Hz. These peaks are also visible at the bottom of the column but are more clearly defined at the top. The building amplifies the vibrations at these frequencies. This peaks can also be seen when considering the building alone as in Chapter 3 and coincide with certain eigenmodes of the building.

Case 3: 10 × 7 building at $x = 0$ m and $y = 20$ m

In this case five floors are added to the building. The same building parameters as in Case 2 are used and the building is located at the same position.

The vertical PSD at the base of the centre column is shown in Figure 4.7 and the vertical PSD at the top of the centre column is shown in Figure 4.8. The difference with Case 2 at the base is limited. At lower frequencies the PSD is reduced and the peak is slightly shifted to the left due to the extra mass added to the building. At the top of the column the reduction is more clearly visible.

Case 4: 5×7 building at $x = 40$ m and $y = 20$ m

The building is relocated to $x = 40$ m and $y = 20$ m, so the building is further away from the tunnel. It is the same building as in Case 2 and the same parameters are used.

The vertical PSD at the base of the centre column is shown in Figure 4.7 and the vertical PSD at the top of the centre column is shown in Figure 4.8. At frequencies below 60 Hz the vibration level is only slightly lower than in Case 2 and Case 3 but at frequencies above 60 Hz the difference is larger. Overall the differences remain small. Since the building is the same as in Case 2, the different vibration is due to the different location of the building. Also note that as the building lies further away from the tunnel in the x -direction, the lateral vibrations will become more important. These, however, are not included in the model.

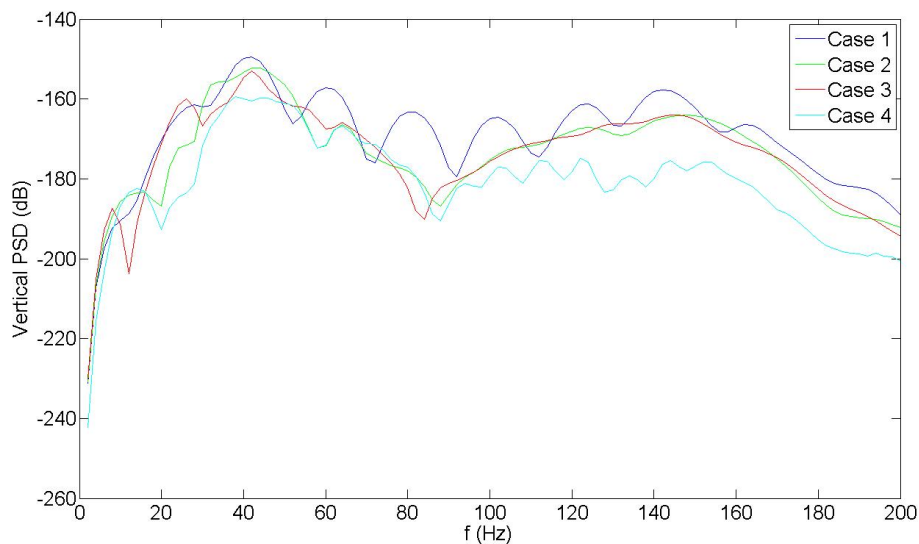


FIGURE 4.7: Vertical PSD at the base of the centre column.

4.6 Conclusion

The displacement response of the building model described in Chapter 3 due to underground railway vibrations generated by the PiP model was calculated in this chapter. This is done in two steps. First the displacements at the pile locations are determined and second, the displacement response of the building is calculated.

To join the PiP model and the building model, the method of joining subsystems is used. The composite system produced using this method represents an uncoupled source-receiver model. It is assumed that the presence of a building has no influence on the vibration level generated by the underground railway.

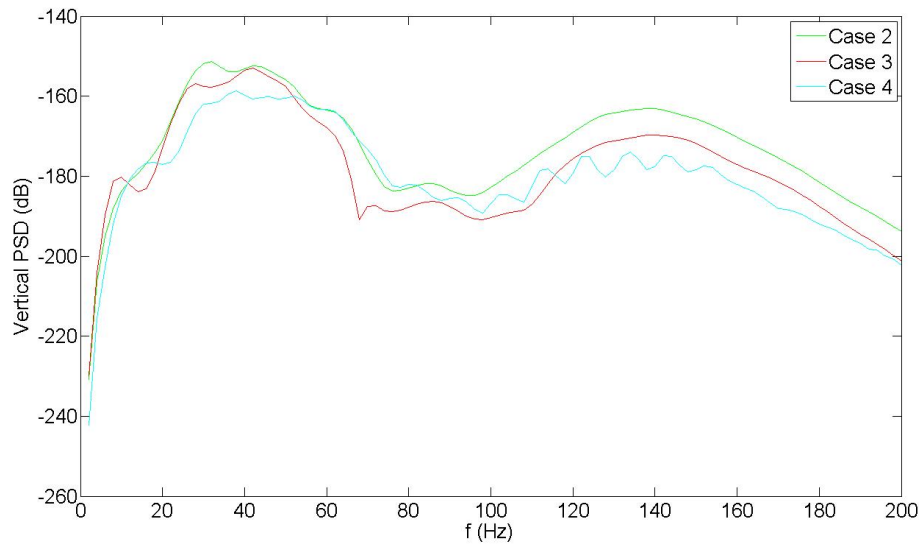


FIGURE 4.8: Vertical PSD at the top of the centre column.

The displacement response is calculated for an input at each pile separately. Superposition is used to combine the results for the different inputs. Only the vertical displacements obtained from the PiP model are used as inputs because the Novak model used to model the piles only properly represents the axial behaviour of a pile.

The GUI of the PiP model is adapted and now includes a building model. A case study performed with this GUI indicates that in general the vibration level at the base of the building will be reduced compared to the original vibration level in the soil. At a frequency of 40 Hz and 140 Hz, the vibration level in the building is at a peak level. At these frequencies the waves propagate more easily through the building.

Chapter 5

Composite tunnel

In this chapter a composite tunnel is modelled using the same techniques as described in Chapter 2. The aim is to add an extra layer of damping to the inside or outside of the tunnel to reduce the vibrations that propagate into the soil. This can be compared with the free layer damping and constrained layer damping used frequently in the aeronautic industry.

In the case of free layer damping (unconstrained damping), a single damping layer is added to a steel or aluminium plate. The damping layer only works in tension or compression, so the damping is limited. In the case of constrained layer damping, the damping layer is constrained between two layers of sheet metal. The damping layer experiences both tensional/compressive strain and shear strains. More strains means more scope to dissipate energy. The construction is more complex, but has a higher performance [16].

The positive effect of this damping method is clear in aeronautic and automotive applications, but it is not certain that it will have an effect in the case of vibrations from underground railways. The frequency range of interest for these vibrations lies below the range where the constrained layer damping technique is effective. A second reason why this method may not be applicable in practical situations is the construction method of tunnels for underground railways. The tunnels as modelled in Chapter 2 are most often excavated with a Tunnel Boring Machine (TBM). This machine both excavates the soil and delivers precast concrete wall sections to the front of the tunnel. It isn't possible with this setup to add an extra damping layer to the tunnel wall except when the precast sections already include this extra layer.

Nevertheless, it is useful to model this composite tunnel. It is an interesting exercise and gives a good insight in the way the PiP model works. Furthermore, it shows how easy it is to extend the PiP model with new features.

In section 5.1 the equations to model the composite tunnel will be derived. The different elements of the composite tunnel will be joined in section 5.2. In section 5.3 a parametric study will be executed and then a conclusion will be made.

5.1 Continuum equations for the composite tunnel and surrounding soil

In Figure 5.1 a cross section of the composite tunnel is shown. The tunnel is divided into two parts, part *A* and part *B*, each of which can have different material parameters and thickness. This means that two different materials can be used and a composite tunnel is formed. In contrast to the PiP model, both the tunnel and the soil are modelled with the elastic continuum equations. The coordinate system as depicted in Figure 2.4 is used.

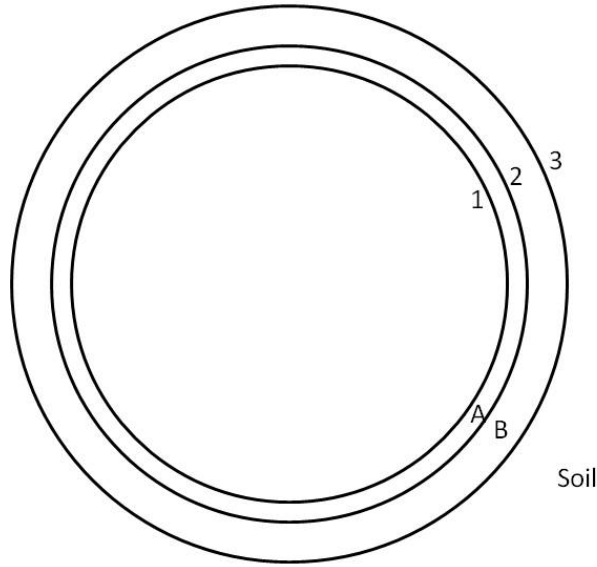


FIGURE 5.1: Cross section composite tunnel. Parts *A* and *B* of the tunnel are indicated and the interfaces between the different elements are numbered.

The elastic continuum equation's displacements and stresses are written in the wavenumber-frequency domain. From (2.20) the displacement and surface stress components for part *A* of the tunnel are

$$\tilde{\mathbf{U}}_A = \mathbf{U}_A \mathbf{C}_A \quad \text{and} \quad \tilde{\mathbf{T}}_A = \mathbf{T}_A \mathbf{C}_A \quad (5.1)$$

and for part *B*

$$\tilde{\mathbf{U}}_B = \mathbf{U}_B \mathbf{C}_B \quad \text{and} \quad \tilde{\mathbf{T}}_B = \mathbf{T}_B \mathbf{C}_B \quad (5.2)$$

For the soil the simplified continuum equations from (2.30) and (2.31) are used

$$\tilde{\mathbf{U}}_s = \mathbf{U}_s \mathbf{B} \quad \text{and} \quad \tilde{\mathbf{T}}_s = \mathbf{T}_s \mathbf{B} \quad (5.3)$$

5.2 Coupling the tunnel and the soil

In this section the boundary conditions are included and the different elements of the tunnel are connected.

The applied load generates following stresses on the tunnel invert

$$\tilde{\mathbf{P}} = \begin{Bmatrix} \tilde{P}_{rr} \\ \tilde{P}_{r\theta} \\ \tilde{P}_{rz} \end{Bmatrix} \quad (5.4)$$

Force equilibrium at the invert of the tunnel results in:

$$\tilde{\mathbf{T}}_A = [\mathbf{T}_A]_1 \mathbf{B}_A = \tilde{\mathbf{P}} \quad (5.5)$$

Compatibility at the interface between part A and B of the tunnel results in

$$\begin{aligned} \tilde{\mathbf{U}}_{A_2} &= [\mathbf{U}_A]_2 \mathbf{C}_A = [\mathbf{U}_B]_2 \mathbf{C}_B = \tilde{\mathbf{U}}_{B_2} \\ \tilde{\mathbf{T}}_{A_2} &= [\mathbf{T}_A]_2 \mathbf{C}_A = [\mathbf{T}_B]_2 \mathbf{C}_B = \tilde{\mathbf{T}}_{B_2} \end{aligned} \quad (5.6)$$

Compatibility at the interface between part B and the soil results in

$$\begin{aligned} \tilde{\mathbf{U}}_{B_3} &= [\mathbf{U}_B]_3 \mathbf{C}_B = [\mathbf{U}_s]_3 \mathbf{B} = \tilde{\mathbf{U}}_s \\ \tilde{\mathbf{T}}_{B_3} &= [\mathbf{T}_B]_3 \mathbf{C}_B = [\mathbf{T}_s]_3 \mathbf{B} = \tilde{\mathbf{T}}_s \end{aligned} \quad (5.7)$$

Subscript 1 refers to the tunnel invert, 2 to the interface between part A and B , and 3 to the tunnel-soil interface as depicted in Figure 5.1.

From expressions (5.5) to (5.7), the coefficients \mathbf{C}_A , \mathbf{C}_B and \mathbf{B} can be determined. Using equations (5.7) an expression for \mathbf{C}_B is found

$$\begin{aligned} \mathbf{B} &= [\mathbf{U}_s]_3^{-1} [\mathbf{U}_B]_3 \mathbf{C}_B \\ ([\mathbf{T}_B]_3 - [\mathbf{T}_s]_3 [\mathbf{U}_s]_3^{-1} [\mathbf{U}_B]_3) \mathbf{C}_B &= \mathbf{O} \end{aligned} \quad (5.8)$$

where \mathbf{O} is a 3×1 zero vector. The term between brackets on the left hand side of the second expression is a 3×6 matrix. By combining the two expressions in (5.6) \mathbf{C}_B can be written in function of \mathbf{C}_A as

$$\begin{aligned} \begin{bmatrix} [\mathbf{U}_A]_2 \\ [\mathbf{T}_A]_2 \end{bmatrix} \mathbf{C}_A &= \begin{bmatrix} [\mathbf{U}_B]_2 \\ [\mathbf{T}_B]_2 \end{bmatrix} \mathbf{C}_B \\ \mathbf{C}_B &= \begin{bmatrix} [\mathbf{U}_B]_2 \\ [\mathbf{T}_B]_2 \end{bmatrix}^{-1} \begin{bmatrix} [\mathbf{U}_A]_2 \\ [\mathbf{T}_A]_2 \end{bmatrix} \mathbf{C}_A \end{aligned} \quad (5.9)$$

With expressions (5.5), (5.8) and (5.9), the coefficients \mathbf{C}_A can be determined as

$$\mathbf{C}_A = \left[\begin{array}{c} [\mathbf{T}_A]_1 \\ ([\mathbf{T}_B]_3 - [\mathbf{T}_s]_3 [\mathbf{U}_s]_3^{-1} [\mathbf{U}_B]_3) \end{array} \begin{array}{c} [\mathbf{U}_B]_2 \\ [\mathbf{T}_B]_2 \end{array} \right]^{-1} \begin{array}{c} [\mathbf{U}_A]_2 \\ [\mathbf{T}_A]_2 \end{array} \begin{Bmatrix} \tilde{\mathbf{P}} \\ \mathbf{O} \end{Bmatrix} \quad (5.10)$$

The term in between square brackets on the right hand side of equation (5.10) is a 6×6 matrix. Once the coefficients \mathbf{C}_A are determined, coefficients \mathbf{C}_B and \mathbf{B} can be calculated from (5.9) and (5.8). The displacements and stresses at some radius R in the tunnel or soil can be calculated with

$$\tilde{\mathbf{U}}_n = [\mathbf{U}_A]_{r=R} \mathbf{C}_A \quad \text{and} \quad \tilde{\mathbf{T}}_n = [\mathbf{T}_A]_{r=R} \mathbf{C}_A \quad (5.11)$$

if $r_1 \leq R < r_2$ or with

$$\tilde{\mathbf{U}}_n = [\mathbf{U}_B]_{r=R} \mathbf{C}_B \quad \text{and} \quad \tilde{\mathbf{T}}_n = [\mathbf{T}_B]_{r=R} \mathbf{C}_B \quad (5.12)$$

if $r_2 \leq R < r_3$ or with

$$\tilde{\mathbf{U}}_n = [\mathbf{U}_s]_{r=R} \mathbf{B} \quad \text{and} \quad \tilde{\mathbf{T}}_n = [\mathbf{T}_s]_{r=R} \mathbf{B} \quad (5.13)$$

if $R > r_3$.

5.3 Parametric study

A parametric study is performed to investigate the effect of a composite tunnel. A single tunnel and a composite tunnel of the same thickness t are compared for different compositions of the composite tunnel. The dimensions of the single and the composite tunnel are given in Table 5.1. The single tunnel is made out of concrete. One part of the composite tunnel is made out of concrete while the other part is made out of steel or a rubber like material (damping layer). The material parameters of the different materials used here and the soil parameters are given in Table 5.2. The displacements are calculated at $R = 20$ m directly above the tunnel ($\theta = 180^\circ$) for a unit load applied on the tunnel invert at $x = 0$. The frequency range considered is 1 Hz - 200 Hz, this is the range of importance for vibrations from underground railways. Note that no track is added to the model, this reduces the computation time.

	t [m]	$r_i = r_1$ [m]	r_2 [m]	$r_0 = r_3$ [m]
Single tunnel	0.30	2.70	-	3.00
Composite tunnel	0.30	2.70	2.85	3.00

TABLE 5.1: Dimensions single and composite tunnel

	E [Pa]	ν [-]	ρ [kg/m ³]	η_G [-]	η_K [-]
Concrete	50e9	0.3	2500	-	-
Steel	200e9	0.3	7850	-	-
Rubber	0.1e9	0.4	1500	-	-
Soil	0.55e9	0.44	2000	0.06	0

TABLE 5.2: Material parameters

Case 1: Concrete-concrete

By using concrete for part A and B of the tunnel the model for the composite tunnel can be validated. In Figure 5.2 the displacements of both the single tunnel and the composite tunnel are shown. The displacements are calculated with equation (5.13) in the wavenumber-frequency domain and then transformed into the space-frequency domain by taking the inverse Fourier transform. The results are expressed in dB. Also the insertion gain is given in Figure 5.2. The insertion gain indicates the increase in vibration level when a composite tunnel is used and is given by

$$\text{Insertion Gain [dB]} = 20 \log_{10} \sqrt{\frac{U_n(\text{composite tunnel})}{U_n(\text{single tunnel})}} \quad (5.14)$$

The displacement curve coincides for both tunnels and the insertion gain is more or less zero over the frequency range. This validates the model for the composite tunnel.

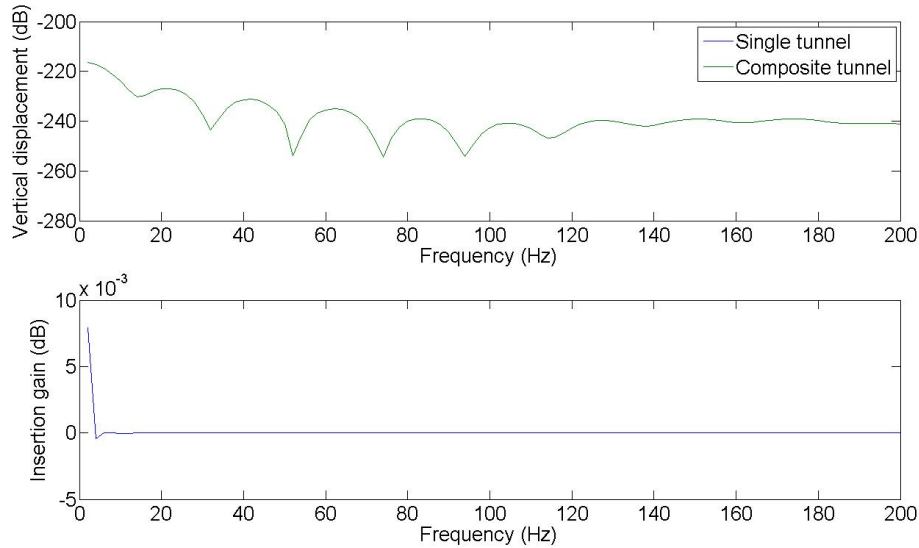


FIGURE 5.2: Displacements and insertion gain at $x = 0$, $\theta = 180^\circ$ and $R = 20$ m. The single tunnel is shown in blue and the composite in green. Part A and B of the composite tunnel are made out of concrete.

Case 2: Concrete-steel

Part A of the composite tunnel is made out of concrete and part B of steel. This means that the outer layer of the tunnel is stiffer than the inside layer. The displacements and insertion gain are shown in Figure 5.3. The difference between both tunnels is limited. The large peak at around 75 Hz in the insertion gain is due to the fact that the response is calculated at discrete frequencies. The peak at 75 Hz in the plot of

the displacements for a composite tunnel will be slightly shifted in comparison to the peak for the single tunnel due to the different stiffness. Due to the small shift of the peak, the calculated displacement response differs and this difference is seen in the plot of the insertion gain. The overall displacement response is marginally lower due to the higher stiffness of the composite tunnel.

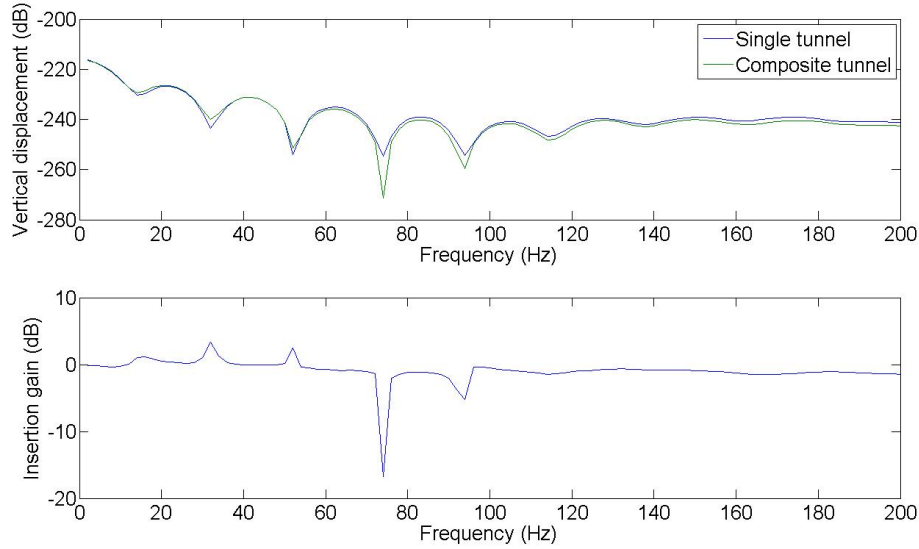


FIGURE 5.3: Displacements and insertion gain at $x = 0$, $\theta = 180^\circ$ and $R = 20$ m. The single tunnel is shown in blue and the composite in green. Part *A* of the composite tunnel is made out of concrete and part *B* is made out of steel.

Case 3: Steel-concrete

Part *A* of the composite tunnel is made out of steel and part *B* of concrete. This means that the inner layer of the tunnel is stiffer than the outer layer. The displacements and insertion gain are shown in Figure 5.4. Again the difference between both tunnels is limited. However large peaks are visible in the plot of the insertion gain. This can be explained by the shift of the peaks seen in the plot of the displacements. When dividing the response of the composite tunnel by that of the single tunnel, a shift of the peaks will result in larger values for the insertion gain. The height of the peaks in the displacement plot are of the same magnitude. The peaks are shifted to the right due to higher stiffness of the composite tunnel compared to the single tunnel. The overall displacement response is also marginally lower.

Case 4: Concrete-rubber

Part *A* of the composite tunnel is made out of concrete and part *B* of rubber. This means that the inner layer of the tunnel is stiffer than the outer layer. The

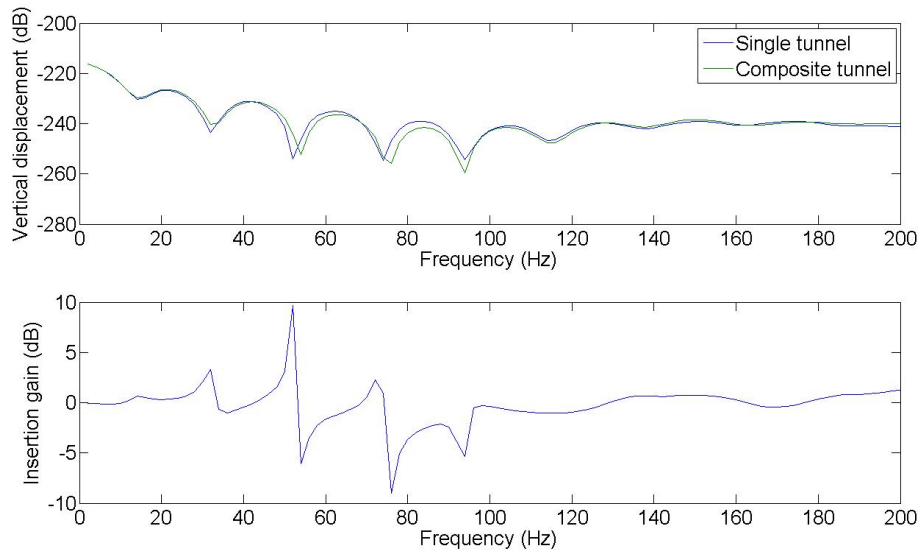


FIGURE 5.4: Displacements and insertion gain at $x = 0$, $\theta = 180^\circ$ and $R = 20$ m. The single tunnel is shown in blue and the composite in green. Part *A* of the composite tunnel is made out of steel and part *B* is made out of concrete.

displacements and insertion gain are shown in Figure 5.5. The difference between both tunnels is more clearly visible. The shift of the peaks in the displacement plot is larger due to the larger difference between the stiffness of the rubber and concrete than between the stiffness of the steel and concrete. The shift also explains the large peaks in the insertion gain. The overall displacement response is higher due to the lower stiffness of the composite tunnel and the peaks are shifted to the left.

Case 5: Rubber-concrete

Part *A* of the composite tunnel is made out of rubber and part *B* of concrete. This means that the outer layer of the tunnel is stiffer than the inside layer. The displacements and insertion gain are shown in Figure 5.6. The difference between both tunnels is more clearly visible than in Case 1 and 2. The shift of the peaks due to the difference in stiffness can be seen in the the displacements. This results in large peaks in the insertion gain. At lower frequencies it appears that the rubber layer has a negative effect. The overall stiffness is reduced and therefore the displacements are larger. At higher frequency it appears that the rubber has a positive effect. Nevertheless, the impact remains limited.

5.4 Conclusion

A composite tunnel can be modelled in a similar way as the single tunnel of the PiP model described in Chapter 2. Both the composite tunnel and the soil are modelled

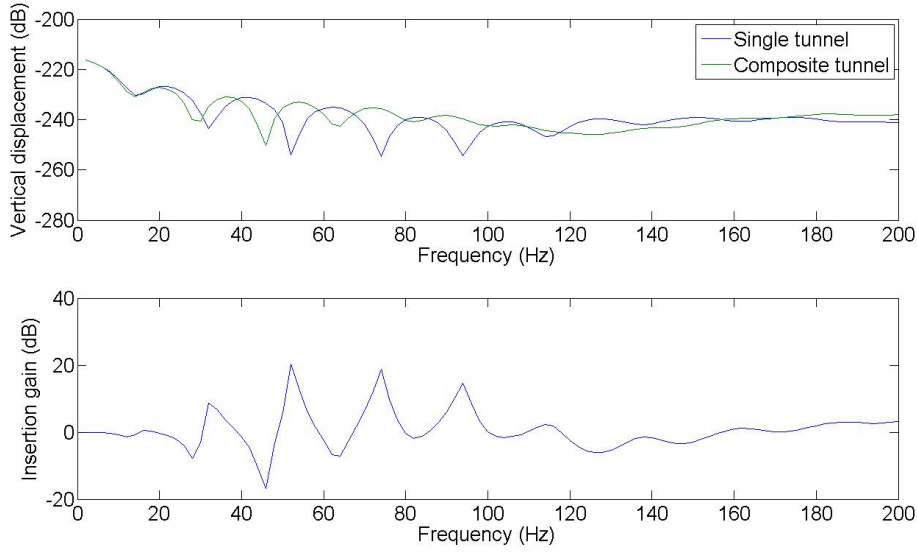


FIGURE 5.5: Displacements and insertion gain at $x = 0$, $\theta = 180^\circ$ and $R = 20$ m. The single tunnel is shown in blue and the composite in green. Part A of the composite tunnel is made out of concrete and part B is made out of rubber.

with the elastic continuum equations. Due to the more extensive matrix operations in equations (5.8) to (5.10) to obtain the coefficients \mathbf{C}_A , \mathbf{C}_B and \mathbf{B} , the computation time is higher than in the original model.

A simple parametric study showed that the effect of using a composite tunnel is limited. The differences observed are more likely due to the difference in overall stiffness of the tunnel than to an extra damping layer as is the case in constrained layer damping. This was predicted because the effective frequency range for constrained layer damping lies well above the frequency range of interest for vibrations of underground railways.

Aside the limited effect, a composite tunnel isn't applicable in real live situations. Current building methods don't allow for an extra layer to be added. Nevertheless, the study of this composite tunnel is of interest because it gives a good insight in the PiP model and it shows that the PiP model is easily expandable.

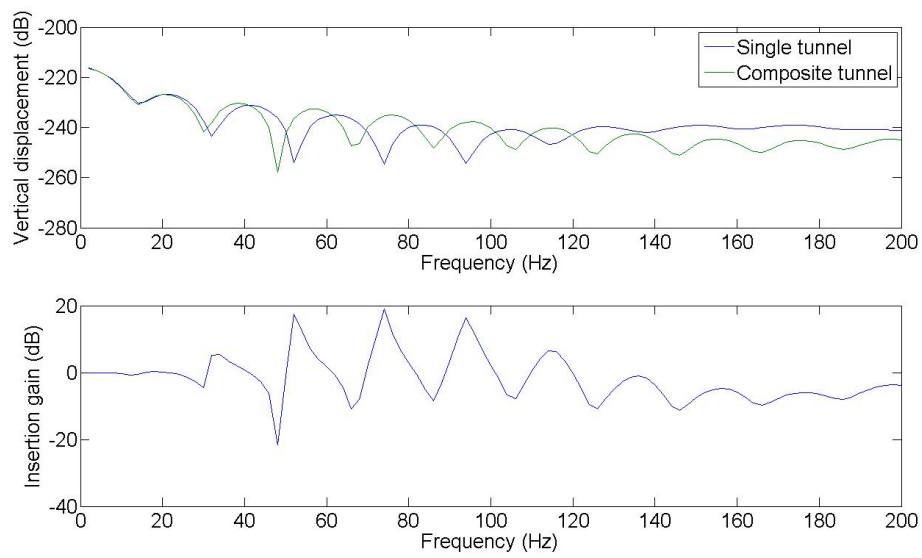


FIGURE 5.6: Displacements and insertion gain at $x = 0$, $\theta = 180^\circ$ and $R = 20$ m. The single tunnel is shown in blue and the composite in green. Part A of the composite tunnel is made out of rubber and part B is made out of concrete.

Chapter 6

Curved tunnel

Underground railway tunnels in urban areas often show some curvature. Therefore it is interesting to see what the influence is of the curvature on the vibration level in the soil. In this chapter a purely geometrical approach is used to model a curved tunnel. It is assumed that the vibration at a point in the soil only depends on the position of that point relative to the curved tunnel and not on the different dynamic behaviour of the tunnel itself. A similar approach is used by Maarten Beckers to investigate the influence of a curved tunnel on the vibration levels [1].

In section 6.1 a method will be developed to model a tunnel that is curved in the horizontal plane. This is repeated for a tunnel that is curved in the vertical plane in section 6.2. Only the vertical displacement response will be considered.

6.1 Curvature in the horizontal plane

Consider a tunnel with curvature R_{cur} as depicted in Figure 6.1. The response is wanted at position P . The tunnel and the track are modelled with the PiP model described in Chapter 2. This means that the tunnel is actually modelled as a straight tunnel of infinite extent.

The train is represented by its' axle masses. The forces acting on the track follow from equation (2.62). These are the forces acting on the rail at the positions of the axles when the mass at the centre station is added via a roughness displacement. The response in the soil can then be calculated with equation (2.64). The FRF matrix H_4 for the curved tunnel differs from that one of the straight tunnel. The elements of the FRF matrix relate the forces acting on the rail to the displacements in the soil. They can be found by applying a unit load at one of the axle stations on the track and calculating the response at position P in the soil.

For example, consider the n^{th} axle to the right of the centre station as shown in Figure 6.1. The coordinates of P relative to the centre station are x_0 , y_0 and z_0 . To calculate the response at P due to a unit load at the position of the n^{th} axle, the coordinates of P relative to this axle position have to be known. Name these coordinates x_n , y_n and z_n . The coordinates are found by assuming a straight tunnel tangent to the curved tunnel at the axle position as can be seen in Figure 6.1.

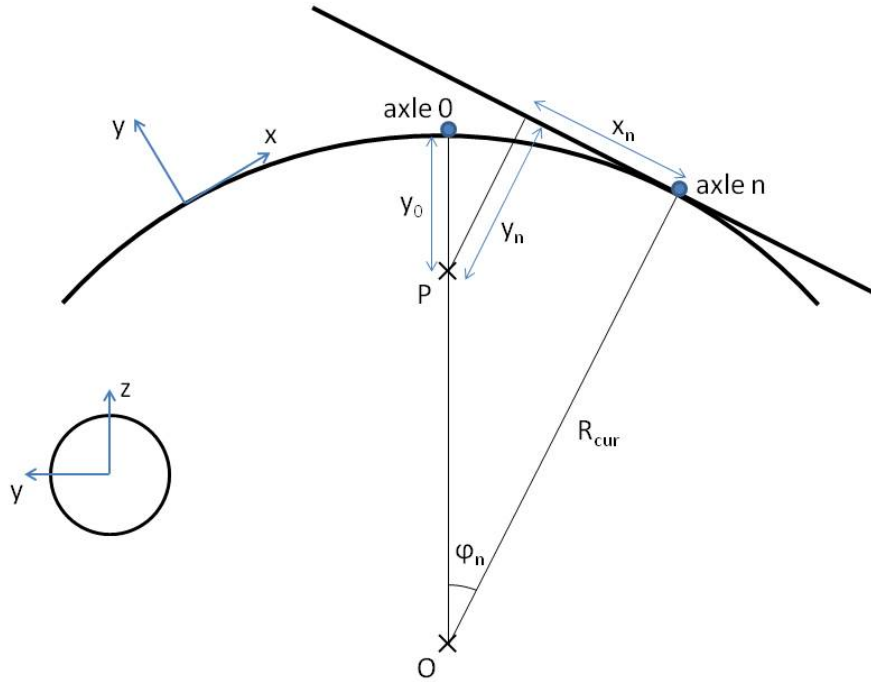


FIGURE 6.1: Schematic representation of a curved tunnel in the horizontal plane. O is the centre of curvature and P is the position where the response is wanted. Axle 0 and n and their coordinates are indicated.

The angle φ_n is defined as

$$\varphi_n = n \frac{L}{R_{\text{cur}}} \quad (6.1)$$

where n is an integer representing the axle, L is the axle spacing and R_{cur} is the curvature of the tunnel. After some basic trigonometric calculations, the coordinates of the n^{th} axle are found:

$$\begin{aligned} x_n^2 &= (R_{\text{cur}} + y_0 - R_{\text{cur}} \cos \varphi_n)^2 + R_{\text{cur}}^2 \sin^2 \varphi_n - ((R_{\text{cur}} + y_0) \cos \varphi_n - R_{\text{cur}})^2 \\ y_n &= (R_{\text{cur}} + y_0) \cos \varphi_n - R_{\text{cur}} \\ z_n &= z_0 \end{aligned} \quad (6.2)$$

These coordinates have to be transformed into the cylindrical coordinates used in the PiP model (Figure 2.2):

$$\begin{aligned} x &= x_n \\ R &= y_n^2 + z_n^2 \\ \theta &= \angle(-z_n - iy_n) \end{aligned} \quad (6.3)$$

Since only the vertical component is of interest, the sign of x doesn't matter because the vertical displacement V is an even function of x . The displacement components

U , V and W calculated for the coordinates given in (6.3) follow the convention of the cylindrical shell (Figure 2.2). The vertical component in the global coordinate system can be found from equation (2.70). This displacement is the FRF $H_{41}(n)$ relating the force acting on the track at the position of the n^{th} axle to the vertical displacement in P .

As an example, consider the case where only 5 masses are added. The FRF matrix \mathbf{H}_4 now becomes, noting that due to symmetry $H_{41}(n) = H_{41}(-n)$ for the vertical component:

$$\mathbf{H}_4 = \begin{bmatrix} H_{41}(4) & H_{41}(3) & H_{41}(2) & H_{41}(1) & H_{41}(0) \\ H_{41}(3) & H_{41}(2) & H_{41}(1) & H_{41}(0) & H_{41}(1) \\ H_{41}(2) & H_{41}(1) & H_{41}(0) & H_{41}(1) & H_{41}(2) \\ H_{41}(1) & H_{41}(0) & H_{41}(1) & H_{41}(2) & H_{41}(3) \\ H_{41}(0) & H_{41}(1) & H_{41}(2) & H_{41}(3) & H_{41}(4) \end{bmatrix} \quad (6.4)$$

The displacement response at P can now be calculated with

$$\mathbf{Y}_4 = \mathbf{H}_4 \mathbf{F}_1 \quad (6.5)$$

where the elements of the vector \mathbf{Y}_4 give the displacement at P due to a roughness-displacement input at one of the axles.

As in Chapter 2, the roughness-displacement inputs for a real track are randomly distributed. Therefore, the calculation of the resultant soil response requires the use of the theory of random vibration. The power spectral density can be obtained with equation (2.68) as explained in section 2.2.4.

As an example, a curved tunnel with $R_{\text{cur}} = 500$ m is modelled and compared to a straight tunnel. In Figure 6.2 the insertion gain is given for a number of points which lie on a horizontal line perpendicular to the tunnel. It is clearly visible that for points at the concave side of the tunnel (negative y -values) the vibration level is generally increased while for points at the convex side (positive y -values) the vibration level is reduced. For a smaller radius of curvature the increase at the concave side and the reduction at the convex side will be larger.

6.2 Curvature in the vertical plane

The approach for a curvature in the vertical plane is analogous to the approach for a curved tunnel in the horizontal plane. The tunnel is modelled with the PiP model and the train is represented by its axle masses.

The forces acting on the track have to be calculated with equation (2.62) first. Next the FRF matrix \mathbf{H}_4 has to be calculated. Consider a tunnel with curvature R_{cur} as depicted in Figure 6.3. As before, the elements of the FRF matrix are obtained by applying a unit load at the positions of the axles and calculating the response at P .

The coordinates of P relative to the n^{th} axle are given by

$$\begin{aligned} x_n^2 &= (R_{\text{cur}} + z_0 - R_{\text{cur}} \cos \varphi_n)^2 + R_{\text{cur}}^2 \sin^2 \varphi_n - ((R_{\text{cur}} + z_0) \cos \varphi_n - R_{\text{cur}})^2 \\ y_n &= y_0 \\ z_n &= (R_{\text{cur}} + z_0) \cos \varphi_n - R_{\text{cur}} \end{aligned} \quad (6.6)$$

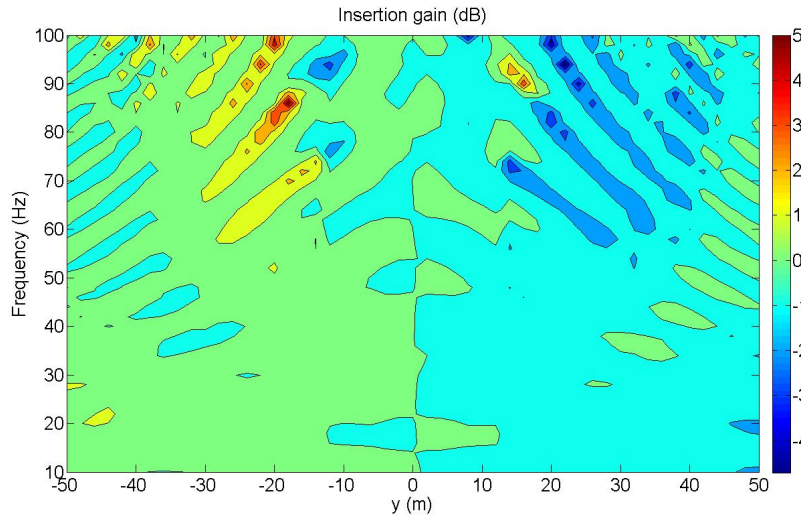


FIGURE 6.2: Insertion gain for a curvature in the horizontal plane

where φ_n is defined in (6.1).

To calculate the displacement in the soil, these coordinates are transformed into the shell coordinates with (6.3). Again only the vertical component in the global coordinate system is of interest. However, for a particular axle n the displacement components due to a force acting on that axle will be given in local coordinates of a straight tunnel tangent to the curved tunnel as shown in Figure 6.4. The displacement components in local coordinates follow from (2.70):

$$\begin{aligned} U_x &= U \\ U_z &= V \sin \theta + W \cos \theta \end{aligned} \quad (6.7)$$

where U , V and W are the displacement components in shell coordinates. The vertical displacement in the global coordinate system can be calculated with:

$$U_Z = U_z \cos \varphi_n + U_x \sin \varphi_n \quad (6.8)$$

If the force acting on the track is a unit point load, the displacement U_Z is the FRF $H_{41}(n)$. The calculations can be repeated for the other axles and the FRF can be assembled as in section 6.1. Note again that $H_{41}(n) = H_{41}(-n)$ when only the vertical component is considered.

The displacement response due to a roughness-displacement input at the different axles can be calculated with equation (6.5). The power spectral density follows from equation (2.68).

As an example, a curved tunnel with $R_{\text{cur}} = 500$ m is modelled and compared to a straight tunnel. In Figure 6.5 the insertion gain is given for a number of points which lie on a vertical line perpendicular to the tunnel. For points at the concave side of the tunnel (negative z -values) the vibration level is increased while for points at the convex side (positive z -values) the vibration level is reduced. The difference is not

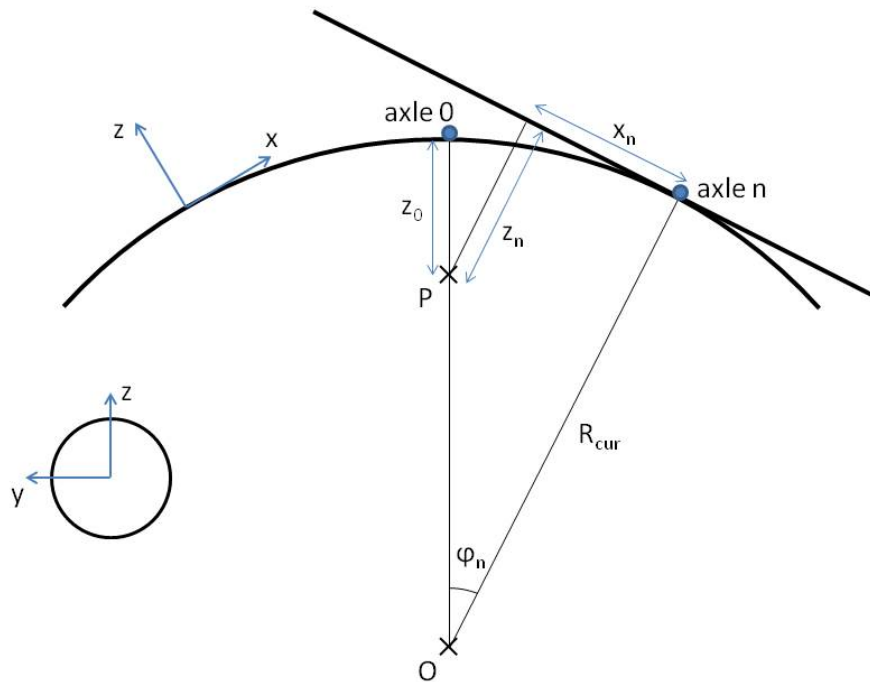


FIGURE 6.3: Schematic representation of a curved tunnel in the vertical plane. O is the centre of curvature and P is the position where the response is wanted. Axle 0 and n and their coordinates are indicated.

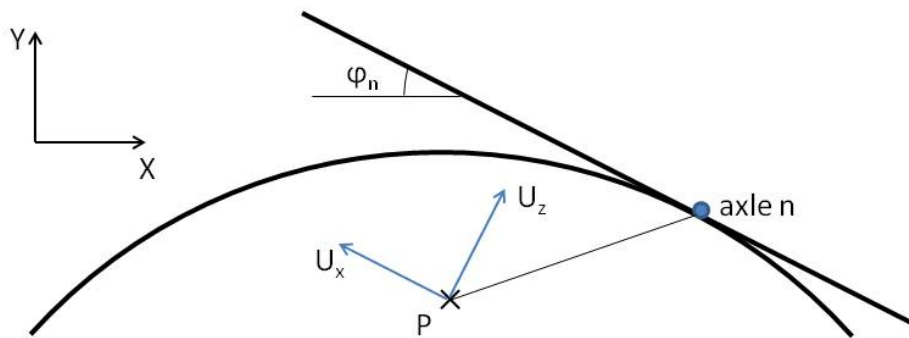


FIGURE 6.4: Global coordinate system for a curved tunnel in the vertical plane. The displacements U_x and U_z at P in local coordinates for a force acting on the track at the position of axle n are indicated.

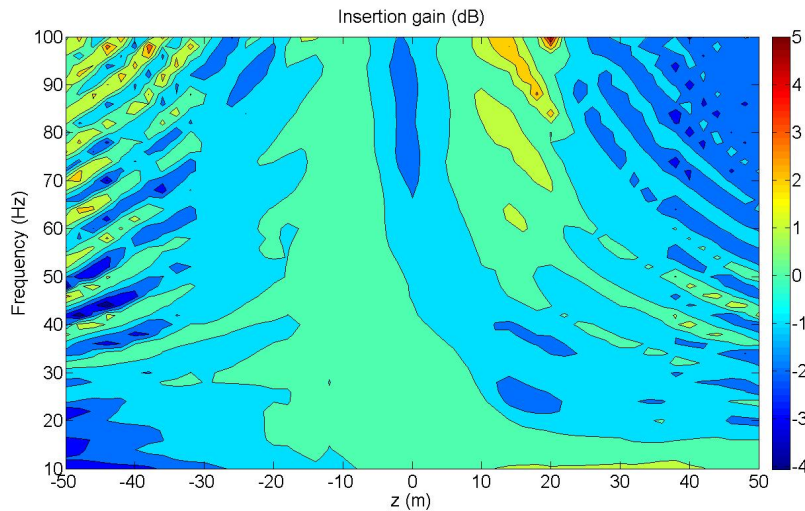


FIGURE 6.5: Insertion gain for a curvature in the vertical plane

as clear as for a curvature in the horizontal plane. This is because the longitudinal component U_x also contributes to the vertical displacement in the global coordinate system.

6.3 Conclusion

A curved tunnel is modelled using a purely geometrical approach. The derivation is done for a curvature in the horizontal and vertical plane. The tunnel and track are modelled with the PiP model discussed in Chapter 2. A similar approach is used by Beckers [1] to model a curved tunnel in the horizontal plane.

The model for a curved tunnel can be coupled to the building model in the same way as discussed in Chapter 4. The computation time however will augment drastically. To compute the displacements at one point in the soil, the original PiP model will have to be runned $(N + 1)/2$ times, where N is the number of axles used. For every axle the calculation has to be repeated because the distance r changes for every axle. Due to symmetry, it is sufficient to repeat the calculations $(N + 1)/2$ times instead of N times. Furthermore, since the tunnel is curved, the calculations have to be repeated as well for every pile of the building which leads to large computation times.

The results obtained here confirm the conclusion Beckers [1] made. At the concave side of the curved tunnel the vibration level is higher then for a straight tunnel and at the convex side the vibration level is reduced as can be expected. However, the influence of the curvature on the vibration level in the soil remains limited. A general conclusion can't be made because only the geometrical aspect of the curvature is investigated and not the different dynamic behaviour of the tunnel itself. This behaviour can be accounted for by using a finite element method.

Chapter 7

Conclusion

The overall conclusions are presented in this chapter. Furthermore, suggestions are given for future work.

7.1 Conclusion

Vibrations from underground railways generate discomfort and noise in buildings. In this dissertation a model is presented to calculate vibration levels in buildings due to an underground railway. The model is computationally efficient and makes it possible to assess design options for both underground railways and buildings.

The PiP model is used to model the underground railway. The soil is modelled as a full space with a cylindrical cavity using the elastic continuum equations and the tunnel wall is modelled as a thin cylindrical shell. The track is modelled as a floating slab track. The PiP model is known to be representative for an underground railway and computationally efficient.

The model for the building is based on the work of Cryer. The building is represented as a two-dimensional portal frame. The dynamic stiffness matrix method is used in combination with periodic structure theory to model an infinite building. Novak's model is used to model the pile foundation of the building. A comparison between finite and infinite models showed that infinite models are a good representation of multistory buildings. Multiple resonances are observed in the finite model without a pile foundation due to waves reflecting at the sides of the building. These resonances, however, are not present in a real building due to damping at the structural joints and radiation damping into the soil and are also not present in the infinite model. After adding a pile foundation, the finite and infinite models agreed much better. The infinite models need less computing power than the finite models and therefore an infinite model is chosen to model the building.

The vibrations generated by the PiP model are used as an input for the building model. An uncoupled source-receiver method is used to join the two models. The building model is integrated in the GUI of the PiP model. Together, they result in an efficient model that can be used to simulate several design options.

A building parallel to the tunnel is the most simple case. Due to the infinite extent of the tunnel, the input at the different piles is the same and therefore the computation time is limited. For a building at an angle to the tunnel, it will take longer to calculate the response of the building since the inputs differ from pile to pile.

The vibration level in the soil will change when a building is added. In general a reduction of the vibration level can be observed due to the extra mass and damping that the building provides. Peaks due to wave interference observed in the soil are smoothed out when a building is added. The vibrations only propagate through the building at particular frequencies. These coincide with certain eigenmodes of the building.

7.2 Recommendations for future work

Instead of using version 3 of the PiP model, version 4 could be used. This version also includes a free surface. Other features, like the two tunnel model developed by Kuo or the curved tunnel presented in this dissertation, could be integrated in the graphical user interface. It has to be noted that adding these extra features will increase the computation time. Therefore, it has to be checked if these features have a significant impact on the vibration level and are of importance when assessing design options.

Only the vertical vibration component is used here as an input for the building model. Instead of using Novak's model, other methods could be used to model the pile foundation so that the lateral behaviour of the pile is correctly modelled. This can be done for example by using the pile model presented by Kuo. It can also be interesting to use a three-dimensional model and compare it to the two-dimensional model presented here.

It is assumed here that the presence of a building has no influence on the vibrations generated by the underground railway. The uncoupled source-receiver model used to join the PiP model to the building model can be replaced by a coupled method. In this way the influence of the building on the vibration level can be investigated and the assumptions made using an uncoupled model evaluated.

Finally, the model presented here should be compared to finite element and boundary element methods to validate its accuracy.

Appendix A

Overview of the PiP model

An overview of the different features and applications of the PiP model is given in Table [A.1](#). The features are ordered chronological in the left column and the people who worked on it in the right column.

Feature	Source
PiP model	Forrest [6]
Track slab with bending and torsion	Forrest [6]
Single pile BE model and building model	Talbot [21]
Pile-soil-pile interaction	Talbot [21]
Continuous versus discontinuous slabs	Hussein [11]
Track with two/three lines of support and uniform support	Hussein [11]
Symmetric and asymmetric load on the tunnel invert	Hussein [11]
Out of phase roughness	Hussein [11]
Graphical user interface PiP	Hussein [11]
Fictitious force method and ElastoDynamic Toolbox	Rikse [19]
Free surface, bedrock and horizontal soil layers	Rikse [19]
Single pile BE model (Timoshenko beam theory)	Coulier [3]
Shadow effect with piles	Coulier [3]
Inter/Intra rail unevenness	Beckers [1]
Horizontal loading on tracks	Beckers [1]
Directly fixed concrete layer on tunnel invert	Beckers [1]
Double track railway	Beckers [1]
Curved tunnels	Beckers [1]
Voids at tunnel-soil interface	Jones [12]
Inclined soil layers	Jones [12]
Inhomogeneous soils	Jones [12]
PiP model for piles and multiple pile models	Kuo [13]
Two tunnel model	Kuo [13]

TABLE A.1: Overview of the different features and applications of the PiP model.

Appendix B

Coefficient matrices for cylindrical shell and elastic continuum

B.1 Coefficients for the cylindrical shell

The elements of the matrix A to calculate the displacements of the cylindrical shell are given below. These coefficients are the full ones derived from the Volmir [22] or Flügge [5] shell equations.

$$\begin{aligned} a_{11} &= \frac{\rho a(1-\nu^2)}{E} \omega^2 - a\xi^2 - \frac{(1-\nu)}{2a} n^2 - \frac{(1-\nu)}{2a} \frac{h^2}{12a^2} n^2 \\ a_{12} &= \frac{(1+\nu)}{2} i\xi n \\ a_{13} &= \nu i\xi + \frac{h^2}{12} (i\xi)^3 + \frac{h^2}{12a^2} \frac{(1-\nu)}{2} i\xi n^2 \\ a_{21} &= -\frac{(1+\nu)}{2} i\xi n \\ a_{22} &= \frac{\rho a(1-\nu^2)}{E} \omega^2 - \frac{a(1-\nu)}{2} \xi^2 - \frac{1}{a} n^2 - \frac{a(1-\nu)}{2} \frac{h^2}{4a^2} \xi^2 \\ a_{23} &= \frac{1}{a} n + \frac{h^2}{12} \frac{(3-\nu)}{2a} \xi^2 n \\ a_{31} &= \nu i\xi - \frac{h^2}{12} (i\xi)^3 - \frac{h^2}{12a^2} \frac{(1-\nu)}{2} i\xi n^2 \\ a_{32} &= \frac{1}{a} n + \frac{h^2}{12} \frac{(3-\nu)}{2a} \xi^2 n \\ a_{33} &= \frac{\rho a(1-\nu^2)}{E} \omega^2 - \frac{h^2}{12} \left(a\xi^4 + \frac{2}{a} \xi^2 n^2 + \frac{1}{a^3} n^4 \right) - \frac{1}{a} + \frac{h^2}{6a^3} n^2 - \frac{h^2}{12a^3} \end{aligned} \tag{B.1}$$

B.2 Coefficients for the elastic continuum

The elements of the matrix \mathbf{U} used to determine the displacement components of the continuum are [6]:

$$\begin{aligned}
 u_{11} &= \frac{n}{r} I_n(\alpha r) + \alpha I_{n+1}(\alpha r) \\
 u_{12} &= \frac{n}{r} K_n(\alpha r) - \alpha K_{n+1}(\alpha r) \\
 u_{13} &= i\xi I_{n+1}(\beta r) \\
 u_{14} &= i\xi K_{n+1}(\beta r) \\
 u_{15} &= \frac{n}{r} I_n(\beta r) \\
 u_{16} &= \frac{n}{r} K_n(\beta r) \\
 u_{21} &= -\frac{n}{r} I_n(\alpha r) \\
 u_{22} &= -\frac{n}{r} K_n(\alpha r) \\
 u_{23} &= i\xi I_{n+1}(\beta r) \\
 u_{24} &= i\xi K_{n+1}(\beta r) \\
 u_{25} &= -\frac{n}{r} I_n(\beta r) - \beta I_{n+1}(\beta r) \\
 u_{26} &= -\frac{n}{r} K_n(\beta r) + \beta K_{n+1}(\beta r) \\
 u_{31} &= i\xi I_n(\alpha r) \\
 u_{32} &= i\xi K_n(\alpha r) \\
 u_{33} &= -\beta I_n(\beta r) \\
 u_{34} &= \beta K_n(\beta r) \\
 u_{35} &= 0 \\
 u_{36} &= 0
 \end{aligned} \tag{B.2}$$

The elements of the matrix \mathbf{T} used to determine the stress components of the

continuum are [6]:

$$\begin{aligned}
 t_{11} &= \left(2\mu\frac{(n^2-n)}{r^2} - \lambda\xi^2 + (\lambda + 2\mu)\alpha^2\right) I_n(\alpha r) - 2\mu\frac{\alpha}{r} I_{n+1}(\alpha r) \\
 t_{12} &= \left(2\mu\frac{(n^2-n)}{r^2} - \lambda\xi^2 + (\lambda + 2\mu)\alpha^2\right) K_n(\alpha r) - 2\mu\frac{\alpha}{r} K_{n+1}(\alpha r) \\
 t_{13} &= 2\mu i \xi \beta I_n(\beta r) - 2\mu i \xi \frac{(n+1)}{r} I_{n+1}(\beta r) \\
 t_{14} &= -2\mu i \xi \beta K_n(\beta r) - 2\mu i \xi \frac{(n+1)}{r} K_{n+1}(\beta r) \\
 t_{15} &= 2\mu\frac{(n^2-n)}{r^2} I_n(\beta r) + 2\mu\frac{n}{r} \beta I_{n+1}(\beta r) \\
 t_{16} &= 2\mu\frac{(n^2-n)}{r^2} K_n(\beta r) - 2\mu\frac{n}{r} \beta K_{n+1}(\beta r) \\
 t_{21} &= -2\mu\frac{(n^2-n)}{r^2} I_n(\alpha r) - 2\mu\frac{n}{r} \alpha I_{n+1}(\alpha r) \\
 t_{22} &= -2\mu\frac{(n^2-n)}{r^2} K_n(\alpha r) + 2\mu\frac{n}{r} \alpha K_{n+1}(\alpha r) \\
 t_{23} &= \mu i \xi \beta I_n(\beta r) - 2\mu i \xi \frac{(n+1)}{r} I_{n+1}(\beta r) \\
 t_{24} &= -\mu i \xi \beta K_n(\beta r) - 2\mu i \xi \frac{(n+1)}{r} K_{n+1}(\beta r) \\
 t_{25} &= \left(-2\mu\frac{(n^2-n)}{r^2} - \mu\beta^2\right) I_n(\beta r) + 2\mu\frac{\beta}{r} I_{n+1}(\beta r) \\
 t_{26} &= \left(-2\mu\frac{(n^2-n)}{r^2} - \mu\beta^2\right) K_n(\beta r) - 2\mu\frac{\beta}{r} K_{n+1}(\beta r) \\
 t_{31} &= 2\mu i \xi \frac{n}{r} I_n(\alpha r) + 2\mu i \xi \alpha I_{n+1}(\alpha r) \\
 t_{32} &= 2\mu i \xi \frac{n}{r} K_n(\alpha r) - 2\mu i \xi \alpha K_{n+1}(\alpha r) \\
 t_{33} &= -\mu\frac{n}{r} \beta I_n(\beta r) - \mu(\xi^2 + \beta^2) I_{n+1}(\beta r) \\
 t_{34} &= \mu\frac{n}{r} \beta K_n(\beta r) - \mu(\xi^2 + \beta^2) K_{n+1}(\beta r) \\
 t_{35} &= \mu i \xi \frac{n}{r} I_n(\beta r) \\
 t_{36} &= \mu i \xi \frac{n}{r} K_n(\beta r) \\
 t_{41} &= \left(-2\mu\frac{(n^2-n)}{r^2} + \lambda(\alpha^2 - \xi^2)\right) I_n(\alpha r) + 2\mu\frac{\alpha}{r} I_{n+1}(\alpha r) \\
 t_{42} &= \left(-2\mu\frac{(n^2-n)}{r^2} + \lambda(\alpha^2 - \xi^2)\right) K_n(\alpha r) - 2\mu\frac{\alpha}{r} K_{n+1}(\alpha r) \\
 t_{43} &= 2\mu i \xi \frac{(n+1)}{r} I_{n+1}(\beta r) \\
 t_{44} &= 2\mu i \xi \frac{(n+1)}{r} K_{n+1}(\beta r) \\
 t_{45} &= -2\mu\frac{(n^2-n)}{r^2} I_n(\beta r) - 2\mu\frac{n}{r} \beta I_{n+1}(\beta r) \\
 t_{46} &= -2\mu\frac{(n^2-n)}{r^2} K_n(\beta r) + 2\mu\frac{n}{r} \beta K_{n+1}(\beta r) \\
 t_{51} &= -2\mu i \xi \frac{n}{r} I_n(\alpha r) \\
 t_{52} &= -2\mu i \xi \frac{n}{r} K_n(\alpha r) \\
 t_{53} &= \mu\frac{n}{r} \beta I_n(\beta r) - \mu\xi^2 I_{n+1}(\beta r) \\
 t_{54} &= -\mu\frac{n}{r} \beta K_n(\beta r) - \mu\xi^2 K_{n+1}(\beta r) \\
 t_{55} &= -\mu i \xi \frac{n}{r} I_n(\beta r) - \mu i \xi \beta I_{n+1}(\beta r) \\
 t_{56} &= -\mu i \xi \frac{n}{r} K_n(\beta r) + \mu i \xi \beta K_{n+1}(\beta r) \\
 t_{61} &= (\lambda\alpha^2 - (\lambda + 2\mu)\xi^2) I_n(\alpha r) \\
 t_{62} &= (\lambda\alpha^2 - (\lambda + 2\mu)\xi^2) K_n(\alpha r) \\
 t_{63} &= -2\mu i \xi \beta I_n(\beta r) \\
 t_{64} &= 2\mu i \xi \beta K_n(\beta r) \\
 t_{65} &= 0 \\
 t_{66} &= 0
 \end{aligned} \tag{B.3}$$

Appendix C

Displacements of the floating slab track due to unit load on the track

In Figure C.1 a schematic overview is given of the floating slab track in the tunnel as described in 2.2.1. The FRFs are found by applying a unit point load on the rail and calculating the displacement responses of the rail, slab and tunnel invert respectively. The calculations are done in the wavenumber-frequency domain.

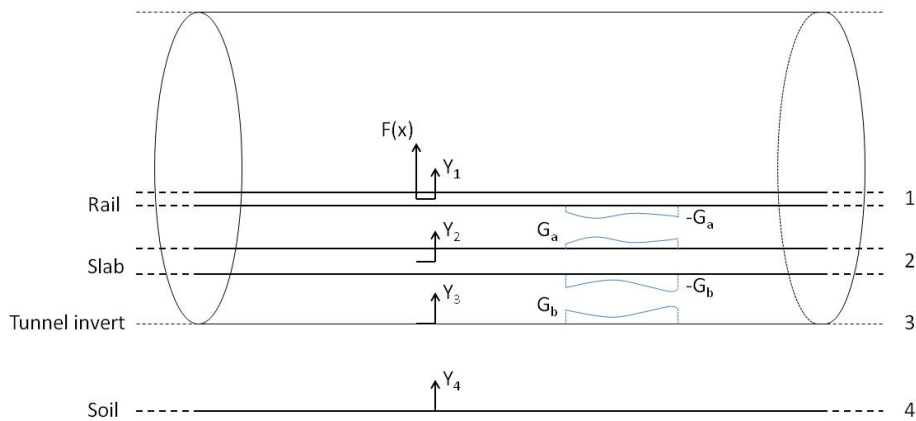


FIGURE C.1: Schematic overview of floating slab track. The displacements and interaction forces acting on the rails, slab and tunnel are indicated.

When a unit point load acts on the slab at $x = 0$ this yields

$$\begin{aligned}\tilde{Y}_1 &= \tilde{H}_{11}(-\tilde{G}_a + 1) \\ \tilde{Y}_2 &= \tilde{H}_{22}(\tilde{G}_a - \tilde{G}_b) \\ \tilde{Y}_3 &= \tilde{H}_{33}\tilde{G}_b\end{aligned}\quad (\text{C.1})$$

for the displacements \tilde{Y}_1 along the rails, \tilde{Y}_2 along the slab and \tilde{Y}_3 along the tunnel invert. The applied point load is equivalent to a force per unit length of $F = \delta(x)$, which gives $\tilde{F} = 1$ when transformed. The functions \tilde{H}_{11} and \tilde{H}_{22} are the FRFs H_{11} and H_{22} in the wavenumber domain for the response of a free beam to a point load at $x = 0$ for the two rails and the slab respectively. The function \tilde{H}_{33} is the FRF H_{33} for the response of the uncoupled tunnel invert to a point load at $x = 0$ in the wavenumber domain.

The joining condition between the rails and the slab and the slab and the tunnel are

$$\tilde{G}_a = k_a(\tilde{Y}_1 - \tilde{Y}_2)\tilde{G}_b = k_b(\tilde{Y}_2 - \tilde{Y}_3) \quad (\text{C.2})$$

Combining equations (C.1) and (C.2) results in a system with five equations and five unknowns, namely \tilde{Y}_1 , \tilde{Y}_2 , \tilde{Y}_3 , \tilde{G}_a and \tilde{G}_b . Substituting equations (C.2) into equations (C.1) gives

$$\begin{cases} \tilde{Y}_1 = \tilde{H}_{11}(-k_a(\tilde{Y}_1 - \tilde{Y}_2) + 1) \\ \tilde{Y}_2 = \tilde{H}_{22}(k_a(\tilde{Y}_1 - \tilde{Y}_2) - k_b(\tilde{Y}_2 - \tilde{Y}_3)) \\ \tilde{Y}_3 = \tilde{H}_{33}(k_b(\tilde{Y}_2 - \tilde{Y}_3)) \end{cases} \quad (\text{C.3})$$

Writing \tilde{Y}_1 and \tilde{Y}_3 in function of \tilde{Y}_2 results in

$$\begin{cases} \tilde{Y}_1 = \frac{k_a\tilde{H}_{11}}{1+k_a\tilde{H}_{11}}\tilde{Y}_2 + \frac{\tilde{H}_{11}}{1+k_a\tilde{H}_{11}} \\ \tilde{Y}_2 = \tilde{H}_{22}\left(k_a\left(\frac{k_a\tilde{H}_{11}}{1+k_a\tilde{H}_{11}}\tilde{Y}_2 + \frac{\tilde{H}_{11}}{1+k_a\tilde{H}_{11}}\right) - k_b\left(\tilde{Y}_2 - \frac{k_b\tilde{H}_{33}}{1+k_b\tilde{H}_{33}}\tilde{Y}_2\right)\right) \\ \tilde{Y}_3 = \frac{k_b\tilde{H}_{33}}{1+k_b\tilde{H}_{33}}\tilde{Y}_2 \end{cases} \quad (\text{C.4})$$

The second expression in (C.4) can be solved for \tilde{Y}_2

$$\tilde{Y}_2 = \frac{k_a\tilde{H}_{11}\tilde{H}_{22}(1 + k_b\tilde{H}_{33})}{1 + k_b\tilde{H}_{33} + k_a\tilde{H}_{11} + k_a\tilde{H}_{22} + k_b\tilde{H}_{22} + k_ak_b\tilde{H}_{11}\tilde{H}_{33} + k_ak_b\tilde{H}_{11}\tilde{H}_{22} + k_ak_b\tilde{H}_{22}\tilde{H}_{33}} \quad (\text{C.5})$$

Substituting this result into the first and third expression of (C.4) results in following equations for \tilde{Y}_1 and \tilde{Y}_3

$$\tilde{Y}_1 = \frac{\tilde{H}_{11}\left(1 + k_a\tilde{H}_{22} + k_b\tilde{H}_{22} + k_b\tilde{H}_{33} + k_ak_b\tilde{H}_{22}\tilde{H}_{33}\right)}{1 + k_b\tilde{H}_{33} + k_a\tilde{H}_{11} + k_a\tilde{H}_{22} + k_b\tilde{H}_{22} + k_ak_b\tilde{H}_{11}\tilde{H}_{33} + k_ak_b\tilde{H}_{11}\tilde{H}_{22} + k_ak_b\tilde{H}_{22}\tilde{H}_{33}} \quad (\text{C.6})$$

$$\tilde{Y}_3 = \frac{k_ak_b\tilde{H}_{11}\tilde{H}_{22}\tilde{H}_{33}}{1 + k_b\tilde{H}_{33} + k_a\tilde{H}_{11} + k_a\tilde{H}_{22} + k_b\tilde{H}_{22} + k_ak_b\tilde{H}_{11}\tilde{H}_{33} + k_ak_b\tilde{H}_{11}\tilde{H}_{22} + k_ak_b\tilde{H}_{22}\tilde{H}_{33}} \quad (\text{C.7})$$

Bibliography

- [1] M. Beckers. Incorporating geometric features into the pip model for subway induced vibrations. Master's thesis, KU Leuven, 2010.
- [2] D. R. Bland. *Theory of Linear Viscoelasticity*. Pergamon Press, 1960.
- [3] P. Coulier. The vibration response of piled foundations to inertial and underground railway induced loadings. Master's thesis, KU Leuven, 2010.
- [4] D. Cryer. *Modelling of Vibration in Buildings with Application to Base Isolation*. PhD thesis, University of Cambridge, July 1994.
- [5] W. Flügge. *Stresses in Shells*. Springer-Verlag, 1973.
- [6] J. Forrest. *Modelling of Ground Vibration from Underground Railways*. PhD thesis, University of Cambridge, June 1999.
- [7] K. Graff. *Wave Motion in Elastic Solids*. Oxford University Press, 1975.
- [8] S. Gupta, M. Hussein, G. Degrande, H. Hunt, and D. Clouteau. A comparison of two numerical models for the prediction of vibrations from underground railway traffic. *Soil Dynamics and Earthquake Engineering*, 27:608–624, 2007.
- [9] H. Hunt. Prediction of vibration transmission from railways into buildings using models of infinite length. *Vehicle System Dynamics*, 24:234–247, 1995.
- [10] H. Hunt and D. Newland. Isolation of buildings from ground vibration: a review of recent progress. *Proceedings of the Institution of Mechanical Engineers, Part C: Mechanical Engineering Science*, 205:39–52, 1991.
- [11] M. Hussein. *Vibration from underground railways*. PhD thesis, University of Cambridge, December 2004.
- [12] S. Jones. *Ground vibration from underground railways: how simplifying assumptions limit prediction accuracy*. PhD thesis, University of Cambridge, September 2010.
- [13] K. Kuo. *Vibration from Underground Railways: Considering Piled Foundations and Twin Tunnels*. PhD thesis, University of Cambridge, September 2011.
- [14] R. Livesley. *Matrix Methods of Structural Analysis*. Pergamon Press, 1975.

- [15] D. Mead. A general theory of harmonic wave propagation in linear periodic systems with multiple coupling. *Journal of Sound and Vibration*, 27:235–260, 1973.
- [16] A. D. Nashif, D. I. Jones, and J. P. Henderson. *Vibration damping*. Wiley, 1985.
- [17] D. Newland. *Mechanical vibration analysis and computation*. Longman, 1989.
- [18] M. Novak. Dynamic stiffness and damping of piles. *Canadian Geotechnical Journal*, 11:574–598, 1974.
- [19] L. Rikse. Modelling of subway induced vibrations using the pipe in pipe model. Master’s thesis, KU Leuven, 2007.
- [20] M. Schevenels. EDT: Elastodynamics Toolbox for MATLAB, March 2012.
- [21] J. Talbot. *On the Performance of Base-Isolated Buildings: A Generic Model*. PhD thesis, University of Cambridge, November 2001.
- [22] A. Volmir. *Nonlinear Dynamics of Plates and Shells*. Nauka, 1972.